Multi-Physics Analysis of Laser Solid Freeform Fabrication

by

Masoud Alimardani

A thesis
presented to the University of Waterloo
in fulfillment of the
thesis requirement for the degree of
Doctor of Philosophy
in
Mechanical Engineering

Waterloo, Ontario, Canada, 2009

AUTHOR'S DECLARATION

I hereby declare that I am the sole author of this thesis. This is a true copy of the thesis, including any required final revisions, as accepted by my examiners.

I understand that my thesis may be made electronically available to the public.

Abstract

The quality of parts fabricated using Laser Solid Freeform Fabrication (LSFF) is highly dependent on the physical phenomena and operating parameters which govern the process. For instance, the thermal stress patterns and intensity, induced throughout the process domain due to the layer-by-layer material deposition and the temperature distribution characteristics, contribute significantly to potential delamination and crack formation across the fabricated part. In this research, some of the main features as well as drawbacks of this technique are studied through a multi-physics analysis of the process. For this purpose, a coupled time-dependent 3D model is developed with which the geometry of the deposited material as well as temperature and thermal stress fields across the process domain can be predicted. In the proposed approach, coupled thermal and stress domains are numerically obtained assuming a decoupled interaction between the laser beam and powder stream. To predict the geometry of the deposited material, once the melt pool boundary is obtained, the process domain is discretized in a cross-sectional fashion based on the powder feed rate, elapsed time, and intersection of the melt pool and powder stream projected on the substrate. Layers of additive material are then added onto the non-planar domain. The main process parameters affected by a multilayer deposition due to the formation of non-planar surfaces, such as powder catchment, are incorporated into the modelling approach to enhance the accuracy of the results. To demonstrate the proposed algorithm and to study the main features of the process, a four-layer thin wall of AISI 304L steel on a substrate of the same material is numerically and experimentally fabricated. The numerical analyses along with the experimental results are then used to investigate the correlation between the temperature-thermal stress fields and crack formation across the fabricated parts. The trend of the results reveals that by preheating the substrate prior to the fabrication process, it is possible to substantially reduce the formed micro-cracks. To demonstrate the feasibility of preheating on the reduction of micro-cracks, several simulations and experiments are performed in which a crack-free result is obtained, with a 22 per cent reduction in thermal stresses when the substrate is preheated to 800 K. The numerical and experimental results are also used to study the circumstances of the microstructural formation during the fabrication process. To conclude this research, the developed modelling approach is further extended to briefly discuss the effects of the path patterns and the main operating

parameters on the outcomes of the process. The effects of the material properties and their variations on the temperature distributions and thermal stress fields are studied by fabrication of a thin wall of two Stellite 6 layers and two Ti layers on a stainless steel substrate.

Acknowledgements

This thesis, a result of four years of research, would not have been possible without the support and encouragement of many people.

I would like to express my gratitude to Professor Ehsan Toysekani for his immeasurably illuminative suggestions and to Professor Jan P. Huissoon for his highly influential guidance throughout my Ph.D. program. I would like to take this opportunity and extend my deepest gratitude to the members of my Ph.D. advisory committee, Professor Amir Khajepour, Professor Steve F. Corbin, Professor Walter W. Duley, and the external member of the committee Professor Milan Brandt who kindly accepted to travel a long distance from Swinburne University of Technology in Melbourne Australia to attend my thesis defense. I feel blessed and fortunate to have benefited from the assistance and wisdom of such highly distinguished scholars in the field of my research.

I would also like to convey my most sincere thanks to all my colleagues in the Automated Laser Fabrication (ALFa) Laboratory at the University of Waterloo for their invaluable participations and kind supports. Finally, my deepest appreciation goes to my family and friends for their sincere encouragements throughout all my life.

I also wish to acknowledge the financial supports of the Natural Sciences and Engineering Research Council of Canada (NSERC), the Ontario Centres of Excellence (OCE), and Ontario Ministry of Training, Colleges and Universities.

Contents

List of Figures

List of Tables

Chapter 1

Introduction

The field of laser material processing has recently faced new directions owing to reduced cost of new laser systems as well as development in high speed computers and consequently computer aided design (CAD), laser technologies, and layered/additive manufacturing techniques. As a result, many sectors including automotive, defense and aerospace have started employing this emerging technology in different fields of welding, cutting and surface treatment. Amongst diverse applications of laser material processing techniques, Laser Solid Freeform Fabrication (LSFF) utilizes the advantageous features of additive manufacturing methods and laser technology which itself has had tremendous impacts on many different fields of science and engineering within the last few decades. This chapter intends to provide an overview on additive manufacturing techniques. The common advantages and disadvantages of these techniques over the conventional methods are briefly pointed out in order to provide a basic picture of the fundamental challenges in their further developments. The last sections of this chapter present the main objectives and contributions as well as an overview of the thesis.

1.1 LSFF and Layered Manufacturing

LSFF, as one of the material additive manufacturing techniques, has shown tremendous potential for different fields of applications such as coating [1], rapid prototyping [2], and

parts repair [3]. Using LSFF, a fully functional near-net-shape three dimensional (3D) object can be fabricated directly from its CAD model by successive layer-by-layer metallurgically bonded deposition of metallic materials. In this process, a laser beam is utilized to melt a thin layer of a moving substrate and powder particles, deposited on the process domain, to form a small track. Each track (clad) is created by rapid solidification of the additive materials together with a thin layer of the moving substrate, or previously deposited tracks. The LSFF process is schematically shown in Figure 1.1.

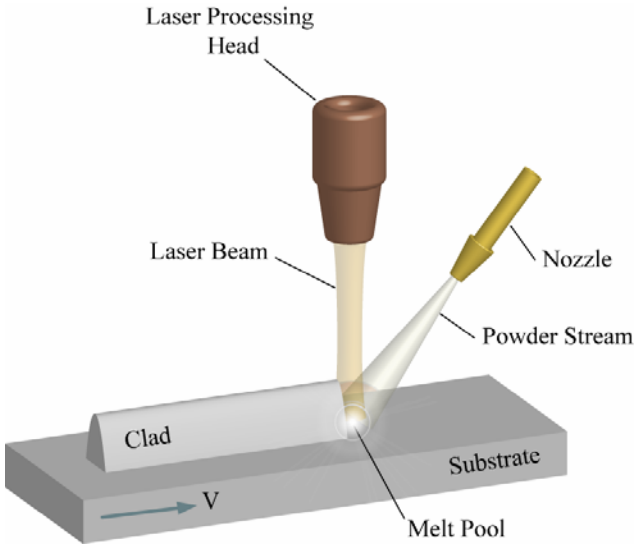

Figure 1.1 Schematic of the LSFF process

Since the LSFF process has been developed and applied to different applications at various academic and industrial facilities around the world, the term LSFF is not unique to describe this technique. The term "laser cladding" is mainly employed for laser surfacing and coating [1], while LSFF, which is also referred to Laser Additive Manufacturing ^{TM} (LAM), Direct Metal Deposition ^{TM} (DMD), and Laser Engineering Net Shaping ^{TM} (LENS), is basically adopted for rapid prototyping or layered manufacturing applications. However, because the physics of the process for different applications is essentially the same regardless of the trade names, the outcomes of this research can be extended to all applications. The main focus remains on rapid manufacturing as one of the most comprehensive and complex applications of this process. Although LSFF offers many inherent advantages over other

additive or layered manufacturing techniques, in a lager scope, additive manufacturing also presents many significant features over subtractive rapid prototyping methods in which a 3D component is created by removing the material from the process domain.

To provide a better understanding of the LSFF process, its advantages and disadvantages, a selective group of additive rapid prototyping techniques will briefly be described in this section. As the main concern of this thesis, the LSFF process and its characteristics will be discussed further in detail in the following chapters. A complete list of additive manufacturing methods and their special features and characteristics including their accuracies and performances are comprehensively provided in the literature [4, 5, 6, 7].

- *Stereolithography (SLA):* This technique is a method in which a photosensitive monomer resin is used as the fabrication material. The resin is converted to a polymer by exposing it to ultraviolet (UV) light (i.e., UV laser beam). A track, with dimensions proportional to the light absorption, is solidified by tracing the laser beam on a thin surface of the resin on a substrate placed in a tank. The substrate is then lowered in the resin tank to fabricate the next layer on the top of the first one. By repeating the process for consecutive layers and tracing a predefined path for each layer, a 3D component can be created. Once the component is fabricated, it is removed from the substrate and placed in an UV oven for post treatment. The SLA process is schematically shown in Figure 1.2.

  The SLA technique is quite popular and produces moderate results in terms of dimensional accuracy than those fabricated using other rapid prototyping techniques. The disadvantages of the SLA process are mainly restrictions on the materials and overhanging parts of the main structure. The choice of materials is limited and cannot be recycled. They are expensive, toxic, brittle, and may shrink or warp after the process. They should also not be kept exposed to ambient light due to premature polymerization. Overhanging parts must be supported using support structures. The supports can be designed as parts of the whole structure during the design stage and removed after the build-up process. This has an adverse effect on the surface finish of the final product.

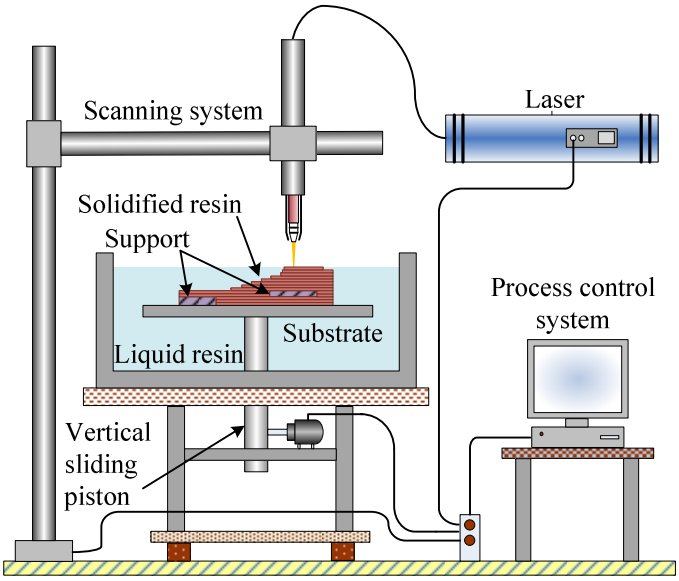

Figure 1.2 Schematic of the SLA process

- *Fused Deposition Modelling (FDM):* In FDM, tracks of additive molten material are deposited on a substrate by feeding thermoplastic polymer through a heated nozzle as shown in Figure 1.3. The molten polymer is then solidified after extrusion and bonded to the previous deposited layer. The material extrusion rate and the nozzle scanning speed have important roles in the quality of the final build-up. For overhanging parts, this method also needs support structures that can be removed after the fabrication process. In this method, it is possible to use another nozzle for deposition of the support structures with cheaper additive materials. There is a wide choice of materials, both color and type, and these are also not toxic. However, the surface finish of the components is poorer than those manufactured using the SLA technique.

- *Selective Laser Sintering (SLS):* SLS is a layered manufacturing technique in which a part can be created by sintering powder particles spread evenly on a substrate using a laser beam as schematically shown in Figure 1.4. In this process, a low power laser beam is used to overcome the surface tension of the powder particles and fuse them together. After sintering each layer, the substrate is lowered and a new layer of powder is spread over the substrate for the next layer fabrication.

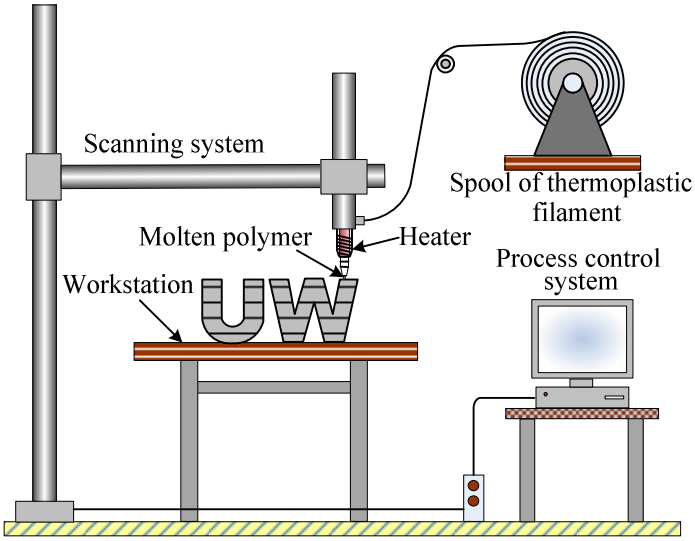

Figure 1.3 Schematic of the FDM process

This method dose not usually requires supporting structures since the unused powder in the chamber participates in the process as support for the sintered sections. A wide range of materials can be used including polycarbonate, PVC, nylon as well as metallic powders and ceramics. The materials used in this technique are not toxic. They are cheaper and can be processed with restively lower laser power compared to the SLA method.

Some of the drawbacks of this method stem from the heating process. After the build-up process, fabricated parts need a long cooling cycle. The cooling cycle depends on the material and for instance might exceed 12 hours for wax parts. The qualities of the parts are extremely sensitive to the process parameters which vary widely for each material. Shrinkage and distortion are other important disadvantages that result from temperature gradients generated throughout the process. They can somewhat be controlled by preheating the powder particles prior to the sintering process.

- *3D Printing*: 3D printing is another example of layered rapid prototyping techniques. In 3D printing, a layer of powder is evenly spread on a substrate and an inkjet printing head sprays a binder on the surface of the powder in a 2D path pattern. Like SLS, the substrate is lowered in a chamber and a thin layer of the powder particles is spread over the previous layer for the next layer printing process. In this process,

aluminum-oxide, and alumina-silica ceramic powders can be used for the fabrication materials and amorphous or colloidal silicon carbide for the binders. In this method, unused powder in the chamber acts as the support for the fabricated part. A post processing treatment is required to enhance the bonding between successive layers and also remove the excess powder particles. Parts manufactured by this technique are prone to several drawbacks including fragility and porosity. The surface finish of the parts is marred by stir-step effects. Removing the excess powder particles from cavities is sometimes difficult as well.

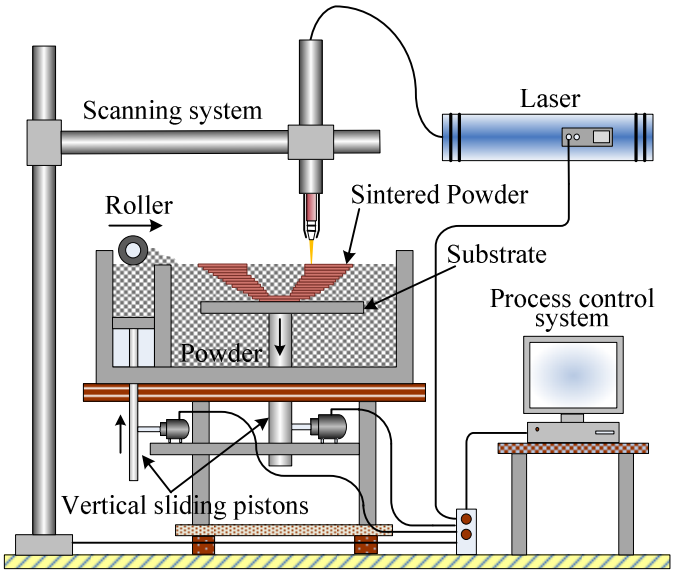

Figure 1.4 Schematic of the SLS process

- *Laminated Object Manufacturing (LOM):* in LOM, a 3D object can be created by successive placing and bonding of plastic, metal or composite sheets on top of each others. After placing a new sheet on the top of the stack, a laser beam, set to penetrate only through one sheet, is employed to cut the sheet into a predefined shape. The cutouts can be removed or kept for the support of the next layer. A hot roll is also used, after each sheet placement, to stimulate the bonding glue spread between successive layers.

  This technique is fairly fast and can use relatively cheap materials such as wood and paper. Compared to other techniques, it can be used for fabrication of relatively

large components. Delamination between the bonded layers, a large amount of cutouts, and difficulty in fabrication of complex geometries (due to limitations on removing the cutouts and placing new sheet) are some of the drawbacks of LOM. In addition, the presence of the laser beam in contact with flammable materials is another disadvantage of this method that should be taken into account compared to other methods.

As noted, the main common feature in layered manufacturing is that the build-up process initiates by decomposition of the CAD model of an object into thin layers (2D surfaces). Therefore, compared to other conventional subtractive methods, the geometrical complexity of an object does not have a significant effect on the manufacturing process development, owing to decomposition of the 3D body into 2D layers [6]. This is more dominant in techniques like LSFF in which 2D layers are fabricated through deposition of sequential tracks overlapped each other with more flexible relative motion between the substrate and deposition system. In addition, layered manufacturing can eliminate many production steps such as drawing preparation, specific size raw material procurement, man-machine interaction process planning, intermittent quality checks, and consequently related human errors [8].

1.2 Problem Statement

Rapid prototyping techniques give a physical identity to a virtual concept. Physical models, although normally not capable of functioning in their real operating conditions, can assist in refining a physical design during the development process prior to mass production. However, in today's highly competitive and fast-changing world, emerging advanced technologies, such as LSFF, demonstrate capacities that exceed existing boundaries and barriers. Rapid manufacturing has defined a new meaning besides rapid prototyping which was fostered and mastered over the last few decades. Rapid manufacturing has shown a wider range of applications whereby fabrication of production quality parts is also possible under rapid manufacturing protocols. This has had an influential effect on the transition from mass production to flexible low-volume-production manufacturing strategies, in which complex structures capable of functioning in a multidisciplinary environment are prevalent.

LSFF as a layered/additive manufacturing technique has shown tremendous potential for these types of applications.

The flexibility of LSFF and its other promising features offer solutions to limitations of comparable methods. However, despite all inherent and demonstrated advantages, like other new techniques, LSFF also has several drawbacks and consequently faces challenges in utilizing its full manufacturing potential.

The main drawbacks of LSFF stem from the same sources as its advantages, the additive nature and the laser beam characteristics [9, 10]. In LSFF, besides the layer-by-layer material deposition, the process domain undergoes cyclic heating and cooling. In addition, the heat source (i.e., laser beam), which is highly concentrated and moves across the fabrication domain, develops an uneven temperature distribution throughout the structure. This process characteristic makes LSFF vulnerable to thermal stresses which are the primary source of potential delamination and crack formation. The heat source characteristics can also play a crucial role in poor bonding and porosity.

On the other hand, one of the most important criteria for rapid manufacturing is fabrication of the parts with accurate geometries and desired mechanical and metallurgical properties. LSFF as a multidisciplinary technology is governed by a large number of process parameters, interrelated and highly sensitive to disturbances. These sensitive and interrelated parameters determine the circumstances of the involved physical phenomena such as heat conduction, melting, phase transformation, and solidification. Accordingly, final mechanical/metallurgical qualities of the fabricated parts using LSFF are highly dependent on the process parameters. Therefore, any disturbances or sudden changes of these parameters may compromise the geometrical accuracy as well as the final structural qualities [11, 12]. Thus, controlling these parameters is critical during the fabrication of an object to maintain desired physical accuracies. In order to bring all variations effectively under the control, it is necessary to understand the relationships between these parameters and their effects on the final build-up. Based on this knowledge, it is possible to design a control plan as well as a path planning paradigm to reduce internal and external disturbances efficiently. Developing the full potential of this emerging manufacturing technique is being investigated by various research groups around the world.

1.3 Contributions of the Dissertation

The main objective of this dissertation is:

> *To investigate the multi-physics of multilayer material deposition in LSFF with the purpose of gaining insight into the process and consequently improving final outcomes*

The central focus of this research is on the multi-physics modelling and characterization of the LSFF process. This is an important step for studying the underlying physics of complex and multidisciplinary processes such as the LSFF process, since it can reduce the number of experimental tests required, and provide data that sometimes are not possible to obtain through experiments. In the course of study, several challenges and drawbacks involved in further development of this technique such as delamination and crack formation are addressed and comprehensively investigated. The research was conducted with an inclination towards utilizing the LSFF process for fabrication of heterogeneous structures, which have many applications in multidisciplinary environments such as biomedical engineering.

1.4 Outline of the Dissertation

This thesis comprises seven chapters. After an introduction to the rapid manufacturing and research objectives in the first chapter, Chapter 2 gives an overview of the LSFF process, including a basic definition of the process, required equipment, its main applications, different process parameters as well as their effects on the physical properties of the final fabricated parts. The LSFF physical domain and its main governing equations besides their associated boundary conditions are also addressed in Chapter 2.

Chapter 3 describes the development of a coupled time-dependent 3D numerical modelling approach for predicting transient geometry of additive materials, thermal characteristics, and thermal stresses induced in the LSFF process as a function of process parameters and material properties. This is performed through mathematical modelling of the process followed by introducing a solution strategy for the multilayer material deposition. The developed approach is then used to simulate the fabrication of a four-layer

thin wall. The effects of the process parameters for a non-planar deposition are also explained in the course of the process modelling. Some of the main numerical results obtained from the process simulation are presented to show the capability of the proposed model. Last section in this chapter is devoted to the experimental analyses performed for verification of the numerical results in terms of the geometry of the wall, temperature, and stress fields across the modelling domain.

In Chapter 4, the temperature distribution characteristics in LSFF, as the main factor that determines the final physical and metallurgical qualities of the parts fabricated using LSFF, is explained. A comprehensive discussion over the numerical results obtained from the simulation of the four-layer thin wall is also presented through a detailed discussion over the melt pool characteristics, thermal stresses, and geometrical features of the wall. Another section of this chapter is allocated to a brief review of the microstructures formed in the LSFF process followed by a discussion on the effects of path patterns on thermal stresses and geometry of the fabricated parts. The last subject discussed in this chapter is allocated to the delamination and crack formation in the LSFF process as one of the main drawbacks in layered manufacturing and particularly in LSFF. In this section, an investigation of the temperature distribution and stress field and their correlation with delamination and crack formation is presented. Preheating the substrate prior to the fabrication process in order to reduce the micro-cracks formed across the fabricated parts is also discussed in this section.

The first section in Chapter 5 describes the effects of the process parameters on the LSFF process in more detail. However, the main subject of this chapter is the fabrication of multi-material objects. An introductory investigation on the effects of the material properties and their variations on the temperature distribution and thermal stress field are presented in this chapter. This is achieved by simulation of a thin wall composed of two different additive materials.

Finally in the last chapter, Chapter 6, a summary of the results is presented followed by an outline of future work and recommendations which stem from the results of the investigations presented throughout this research.

Chapter 2

Background and Physics of the Laser Solid Freeform Fabrication Process

Understanding the physics of a process is a crucial step for developing an efficient approach to optimize and improve the process. This chapter primarily outlines different aspects and characteristics of LSFF including the operating parameters which define the quality of the fabricated parts using the LSFF process. The LSFF main governing equations and their associated boundary conditions are other sections presented in this chapter. Multi material deposition in LSFF and its advantageous features for fabrication of heterogeneous structures are also briefly addressed.

2.1 LSFF process

Laser material processing can be classified into two main groups: applications in which relatively lower laser energies are required (and therefore, there are no changes in the phases and states of the processed materials such as bending or surface hardening) and applications in which relatively higher laser energy is required (and consequently, the processed materials go through phase or state transformations). The LSFF process is one of the laser material

processing techniques in which phase transformations from solid to liquid and liquid to solid occur. Owing to unique laser beam characteristics and the additive nature of the process, LSFF has many advantageous features. A small heat affected zone (HAZ), minimal dilution, direct deposition, and integration of CAD tools with the production process are some of the main features of the LSFF technique. These characteristics can eliminate many manufacturing steps compared to conventional methods, and also overcome the limitations of existing metal manufacturing technologies in terms of reduction of production time, enhancement of thermal controllability, and production of functionally graded parts (heterogeneous structures) which has shown a wide range of applications [1, 2, 3, 13, 14, 15, 16]. For instance, the small HAZ causes minimal warpage and distortion, and consequently a reduction in the susceptibility to cracking [17, 18].

A laser, a positioning device, and a material deposition system are the main equipment needed for the LSFF process. Additive material can be deposited into the process domain by different methods such as pre-placed powder on the substrate, automatic powder injection, and wire feeding. Since utilizing LSFF in industry mainly requires deposition in complex path patterns, regardless of the technical advantages and disadvantages of different deposition methods, LSFF by powder injection has demonstrated to be more practical and efficient. Figure 2.1 shows a schematic arrangement of the LSFF process and its setup using powder injection for the material deposition.

2.2 Applications of LSFF

As pointed out in the first chapter, LSFF under different names has effectively been used for different applications: namely, coating, part repair, and rapid manufacturing. Since there are many published articles and research reports [1, 2, 3, 12, 13]documenting developments, challenges, advantages, and disadvantages of the LSFF process in its various applications, here the discussion will be limited to the potential of the LSFF process for fabrication of functionally graded parts or heterogeneous structures.

Heterogeneous components are usually made of different materials (in this thesis, heterogeneous structures and functionally graded parts are considered the same and they represent structures made of different materials). Due to new fabrication technologies, the

use of heterogeneous objects has shown a rapid increase in the past decade [19]. In many different engineering applications such as biomedical and geophysical applications, conflicting material properties are required in order to enhance mechanical properties and functionality of an object. For instance, it is possible to fabricate a heterogeneous component with low thermal expansion and a relatively high heat transfer rate. Conventional methods cannot create objects in which materials change gradually from one to another. Sharp interfaces between different materials cause stress concentrations that ultimately create delamination and cracks between layers. Another major problem in fabrication of heterogeneous objects is controlling the variation of the different desired materials. Most of the time, a large number of unknown variables are involved in the process which have to be considered together [14].

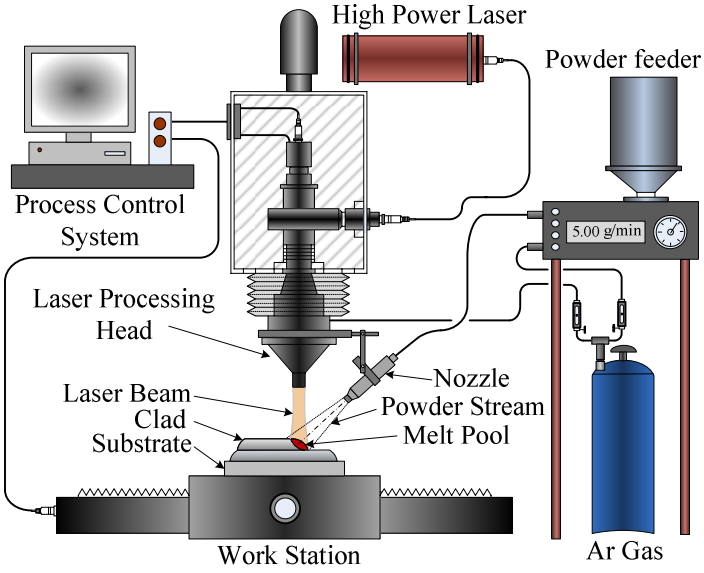

Figure 2.1 Schematic of the LSFF setup

LSFF technology allows the creation of parts with the deposition of different materials (multi-material deposition) in one specific layer or different layers (i.e., material composition varies from layer to layer or from one point to another point). The gradual change from one material to another reduces stress concentrations between the interfaces of subsequent deposited layers, and as a result, dramatically enhance the performance of the fabricated part. However, this variation should be carefully linked with the overall thermal expansion

of the mixed materials to prevent cracks or delamination due to a large difference in the thermal expansion coefficients of the constituent materials.

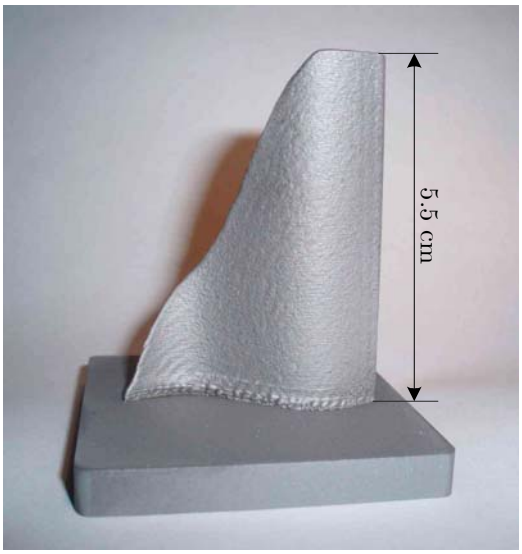

Figure 2.2 Fabrication of a 3D component by the LSFF technique (Source: Courtesy of the Automated Laser Fabrication (ALFa) Laboratory, University of Waterloo)

To study the underlying phenomena from which the LSFF critical drawbacks originate, as briefly discussed in the preceding chapter; it is first necessary to understand the process parameters, their relationships and their effects on the final build-up. Based on these relationships, it is then possible to control the process parameters and consequently counter external disturbances more efficiently during the fabrication process. This is the main focus of the remainder of this chapter.

2.3 LSFF Process Parameters

In LSFF, a large number of operating parameters govern the process. Understanding the relationships between these parameters and their effects on the process are crucial to the geometrical and physical qualities of the fabricated parts. In general, the parameters are classified into two groups. The first group refers to those related to the properties of the powder and the substrate such as the thermal properties of the materials used. The second

group contains parameters specific to the equipment used in the process [11, 20]. These parameters are summarized in Table 2.1 [20].

Some of the process parameters affect each other or are affected by the environment of the process (they are sensitive to the external disturbances). Furthermore, they are highly sensitive to variations of the working parameters as well. Since the quality and geometrical accuracy of a clad depends on the process parameters, they should be kept within certain tolerance ranges throughout the fabrication process to guarantee the results. For example, the desired temperature of the melt pool and consequent temperature distribution over the substrate is a function of process parameters including material properties, laser power density at the process zone, and scanning or traverse speed. These also determine the cooling rate at the liquid-solid transient boundary that has a curial effect on the solidification process and microstructure of the fabricated parts. The temperature distributions (temperature gradients) also determine the thermal strains and therefore thermal stresses across the process domain [21, 22].

Table 2.1 Main Process Parameters

Laser	Motion device	Powder feeder	Material
-Average power -Spot size -Wavelength -Pulsed/CW -Beam profile -Laser pulse shaping	-Relative velocity -Relative acceleration -System accuracy	-Powder feed rate -Inert gas flow rate -Nozzle specification -Powder stream profile	-Substrate Geometry -Composition -Powder size -Surface tension -Metallurgical, thermo-physical and optical properties

On the other hand, any disturbances or sudden changes of these parameters may cause a totally different outcome. For instance, various interaction times, as a function of traverse

speed, result in completely different product in terms of the mechanical and metallurgical characteristics.

In laser material processing, different interaction times and laser power intensities result in three different physical phenomena: vaporization, melting, and heating. Each of these three categories, depends on the interaction time and laser power intensity, also produces different outcomes. LSFF, which is in the melting class, requires approximately an interaction time of 10^{-2} to 10^{-4} s, and a laser power intensity of 10^{3} to 10^{4} W/mm^{2}. In the same zone (melting class), by increasing the laser power intensity, from 10^{3} to 10^{8} W/mm^{2}, and decreasing the interaction time, from 10^{-3} to 10^{-8} s, the process condition will be appropriate for welding, alloying, and glazing, respectively [16, 23]. Therefore, the sensitivity of LSFF to the process parameters and complexity of its involved physical phenomena makes it difficult to produce consistent results witch meet all desired mechanical and geometrical requirements even under the same operating parameters. However, the associated limitations and drawbacks can be overcome efficiently by understanding the process and consequently developing a comprehensive control plan to monitor and control the main process parameters [11, 24].

2.4 Parts Quality

Despite all demonstrated advantages of LSFF compared to conventional manufacturing techniques, LSFF has not been widely employed in industry due to several limitations associated with this manufacturing technique. In the LSFF process, delaminating, crack formation between deposited layers, and variations in the mechanical and metallurgical properties across the structure of the produced parts are some of these limitations and drawbacks.

There are several reported research programs that address the related physical phenomena, specific process parameters, and material properties of a specific product. Some of these research programs have been conducted to characterize the melt pool properties and understand the effects of the process parameters on the LSFF process [21, 25]. The interaction between the laser beam and the powder stream [17, 26], the effect of laser characteristics on the process [27, 28], and the metallurgical and mechanical properties of the

clad [29, 30] have also been investigated. Most of the theoretical investigations in this area involved a large number of assumptions to simplify the modelling procedures [31, 32]. All these research programs have the same goal, which is to gain insight into the process in order to increase the quality of the clad. In practice, it is difficult or impossible to produce a clad which meets all desired mechanical and geometrical requirements, and an optimized set of requirements should be used.

The properties of the deposited layers using the LSFF process can be classified in the following four groups: geometrical, mechanical, metallurgical and qualitative properties. Table 2.2 shows the parameters which contribute to these four groups. Some of these may be inter-related; for instance, the wear resistance can be affected by the hardness, the microstructure, the number of cracks and their depth and direction, and the bonding between base material and substrate [20].

Table 2.2 Clad properties [20]

Geometrical	Mechanical	Metallurgical	Qualitative
-Clad dimensions -Dilution -Roughness	-Hardness -Distribution -Residual stress -Wear resistance -Tensile strength	-Microstructure -Dilution -Grain size -Homogeneity -Corrosion -Resistance	-Porosity -Cracking

2.5 Physical Domain and Mathematical Modelling of the LSFF Process

The physical domain of the LSFF process consists of a substrate, deposited material (i.e., clad), a powder stream, and a laser beam. The LSFF process is schematically shown in Figure 2.3 in which h_c is the clad height, h_d is the depth of the melted substrate, and θ_{jet} is the angle of the powder jet with respect to the substrate. To model the process, the laser beam specifications, material deposition, laser beam-powder interactions, and heat transfer

throughout the process domain should be integrated in a dynamic fashion. All physical phenomena involved in the process can be assembled together based on their relationships through the process governing equations. The following section addresses the governing equations of the process and their associated boundary conditions as well as the significance of the process parameters in the modelling process.

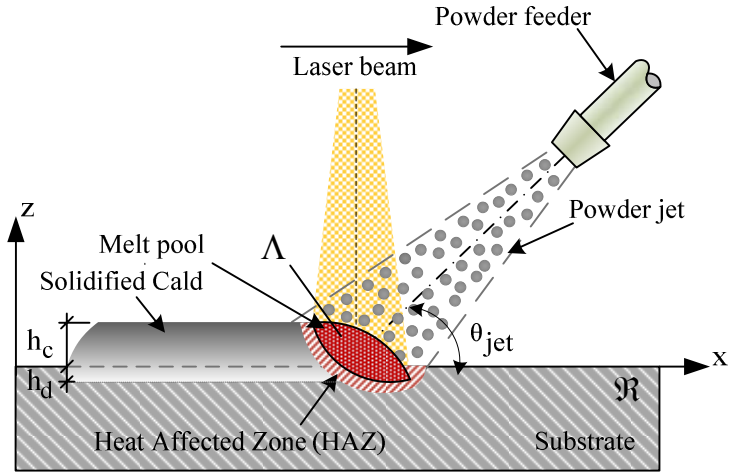

Figure 2.3 Schematic of the deposition domain in the LSFF process with powder injection

2.5.1 Governing Equations

In LSFF, the main portion of the laser energy is directly absorbed by the substrate and forms a melt pool. The powder particles, which are simultaneously added to the process domain, absorb and carry some of the laser energy into the melt pool as well. Some part of the absorbed energy distributed throughout the process domain is then lost through convective and radiative losses. These physical phenomena in the process domain can mathematically be presented by continuity, momentum, and heat conduction equations as follows:

Continuity equation:

$$\frac{\partial \rho}{\partial t} + \nabla.(\rho \mathbf{U}) = 0 \tag{2.1}$$

Momentum equation:

$$\frac{\partial(\rho u_x)}{\partial t} + \nabla.(\rho \mathbf{U} u_x) = \nabla.(\mu \nabla u_x) - \frac{\partial p}{\partial x} \tag{2.2}$$

$$\frac{\partial(\rho u_y)}{\partial t} + \nabla.(\rho \mathbf{U} u_y) = \nabla.(\mu \nabla u_y) - \frac{\partial p}{\partial y} \tag{2.3}$$

$$\frac{\partial(\rho u_z)}{\partial t} + \nabla.(\rho \mathbf{U} u_z) = \nabla.(\mu \nabla u_z) - \frac{\partial p}{\partial z} + \rho \mathbf{g} \tag{2.4}$$

Heat conduction equation:

$$\nabla \cdot (k \nabla T) + Q = \frac{\partial(\rho c_p T)}{\partial t} + \mathbf{U} \cdot \nabla(\rho c_p T) \tag{2.5}$$

where ρ (kg/m^3) is density, t (s) is time, $\mathbf{U}$ (m/s) is the velocity vector, p (Pa) is the pressure, μ (kg/s.m) is viscosity, g (m/s^2) is the gravity field, k (kg/m.K) is thermal conductivity, c_p (J/kg.K) is specific heat capacity, Q (W/m^3) is power generated per volume within the substrate, and u_x, u_y ,u_z (m/s) are the liquid velocities in the x, y and z directions respectively. In addition to Equations (2.1) to (2.5), which are the main equations governing the LSFF process, the concentration equation, and equations related to the evolution of free surface can also be considered along with the main governing equations [16, 25, 33, 34, 35]. The concentration equation, and the level set equation used for tracking the evolution of the free surface are respectively represented as follows:

$$\frac{\partial(\rho c)}{\partial t} + \nabla.(\rho \mathbf{U} \boldsymbol{c}) = \nabla.(\rho D \nabla \boldsymbol{c}) + \nabla.(\rho D \nabla(c_l - c)) - \nabla.(\rho f_s (c_l - c_s)\mathbf{U}) \tag{2.6}$$

$$\frac{\partial \varphi}{\partial t} + F\left|\nabla \varphi\right| = 0 \tag{2.7}$$

where c is the solute concentration, f_s is the solid fraction, D is the mass diffusivity, $\varphi(x,y,t)$ is a distance function, and F is a speed function (or force function) which depends on interfacial forces ($F = F_{fs} + \mathbf{n}.\mathbf{u}$ where F_{fs} is the free surface growth velocity, $\mathbf{n}$ is the normal vector and $\mathbf{u}$ is the fluid velocity).

Another important physical phenomenon that occurs in the LSFF process is the consequence of the nature of the temperature distribution, caused by the moving concentrated heat source across the process domain. The temperature gradients throughout the process domain cause thermal strains, which result in deformation, and consequently thermal stresses. The thermal strain depends on the present temperature and the initial temperature, and is independent of stress.

The total strain ε in a body can be represented as:

$$\varepsilon_{mn} = \varepsilon^{M}_{mn} + \varepsilon^{T}_{mn} \qquad (m,n = 1,2,3) \tag{2.8}$$

where ε^{M} (m/m) and ε^{T} (m/m) are the strains contributed from the mechanical forces and temperature changes, respectively. As the stress is a linear function of strain, the constitutive equation for linear elastic materials is [36]:

$$\sigma_{ij} = D_{ijmn}\varepsilon_{mn} \qquad (i,j,m,n = 1,2,3) \tag{2.9}$$

where σ_{ij} (Pa) is the elastic stress, and D_{ijmn} (Pa) is the tensor of elastic coefficients with 81 components. Due to symmetry of the strain and stress tensors, in general only 36 components are independent.

As a small section of the process domain goes under the high temperature regime, therefore for the HAZ and melt pool zone, the effects of the plastic strain and phase transformation (i.e., volume change and transformation plasticity) should also be taken into account. Considering these effects, Equation (2.8) can be written in its comprehensive form as:

$$\dot{\varepsilon}_{mn} = \dot{\varepsilon}^{M}_{mn} + \dot{\varepsilon}^{T}_{mn} + \dot{\varepsilon}^{P}_{mn} + \dot{\varepsilon}^{Tp}_{mn} + \dot{\varepsilon}^{V}_{mn} \qquad (m,n = 1,2,3) \tag{2.10}$$

where ε^{P} (m/m) is the plastic strain, ε^{Tp} (m/m) is the contribution of the transformation plasticity effect, and ε^{V} (m/m) is the strain resulted from the volumetric dilatation.

Based on problem specifications, appropriate expressions for these strains are suggested in the literature [37, 38].

2.5.2 Boundary Conditions and Assumptions

To solve the equations governing the LSFF process, appropriate boundary and initial conditions are required for all points of an enclosed boundary during the process time, and particular conditions at one point in time (i.e., initial condition). For thermal strain and stress fields, it is also necessary to consider boundary conditions which prescribe the external forces and any displacement at the boundary surface. Furthermore, some of the process specifications such as the heat source (i.e., laser beam) and its moving effect need to be considered in the associated boundary conditions.

The second order heat conduction Equation (2.5) must be solved under appropriate initial-essential and boundary conditions. The initial and essential conditions are:

$$T(x,y,z,0) = T_0 \tag{2.11}$$

$$T(x,y,z,\infty) = T_0 \tag{2.12}$$

where T_0 (K) is the ambient temperature. The convection and radiation boundary condition can be considered together as:

$$k(\nabla T \cdot \mathbf{n})\,|_{\Re} = [-h(T-T_0) - \varepsilon_R\,\sigma_R(T^4 - T_0^4)]\,|_{\Re} \quad \text{if } \Re \notin \Lambda \tag{2.13}$$

where $\mathbf{n}$ is the normal vector of the surface, ε_R is emissivity, h is the heat convection coefficient (W/m^2.K), σ_R is the Stefan-Boltzman constant (5.67×10^{-8} W/m^2.K^4) ,$\Re$ (m^2) is the substrate surface, Λ (m^2) is the area of the laser beam on the substrate. $\Re$ and Λ are shown in Figure 2.3. The effect of the moving laser beam can also be considered as a surface heat source in the boundary conditions as follows:

$$k(\nabla T \cdot \mathbf{n})\,|_{\Re} = [\beta I(x,y,z,U,t) - h(T-T_0) - \varepsilon_R\,\sigma_R(T^4 - T_0^4)]\,|_{\Re} \quad \text{if } \Re \in \Lambda \tag{2.14}$$

where β is the absorption factor, I (W/m^2) is the laser power distribution on the substrate, U (m/s) is the velocity in the x, y and z directions, respectively. Initial conditions for stress and strain fields which prescribe the external forces and any displacement at the boundary surface at the beginning of the LSFF process are:

$$\varepsilon(x,y,z,0)|_{T=T_o}=0 \quad \& \quad \sigma(x,y,z,0)|_{T=T_o}=0 \tag{2.15}$$

Since the solute atoms throughout the solidification process disperse into the liquid phase as a result of rejection from the solidification front, the boundary condition can be defined as the gradient of the solute concentration on the liquid side [34]:

$$-D_l \frac{\partial c_l}{\partial n} = (1-k_p) v_n c_l \tag{2.16}$$

where v_n (m/s) is the normal interface velocity. The boundary condition at the liquid-gas interface is [34]:

$$c|_{\varphi=0} = c_{pp} \tag{2.17}$$

where c_{pp} is the powder particle solute concentration. More details regarding the boundary conditions of free surfaces and forces applied at liquid-gas interfaces can be found in the literature [25, 34].

To model the LSFF process, the next step is to mathematically model the process using the governing equations along with their associated boundary conditions. After this, the last step is to develop a strategy to solve the mathematical model which is obtained from the governing equations and their boundary conditions along with appropriate adjustments such as considering the effect of the moving laser beam.

Since considering all phenomena realistically occurring during the LSFF process makes the problem highly complicated, some adjustments as well as assumptions for reducing the complexity of the problem have to be taken into account. To name a few, many models were developed only for the two-dimensional domain. In some modelling approaches, the effect of the additive materials was ignored or considered in a decoupled fashion, while in some other approaches the additive materials were considered in the model with a predefined geometry. To simplify the mathematical formulation, the effects of heat losses through convection and radiation were partially/fully overlooked or considered together with a proper approximation. Because many physical phenomena are involved in this multifaceted process, a large number of diverse assumptions and adjustments can be listed. However, these

assumptions are made in a way to keep any possible compromises to a minimum regarding the aspect of the process which is under investigation.

In the next chapter, various LSFF modelling approaches developed by different research groups along with their main features, including their associated assumptions and adjustments will first be addressed. Then, a coupled time-dependent 3D numerical modelling approach of the LSFF process developed based on the process governing equations and their boundary condition presented in this section will be explained in detail.

2.6 Summary

The LSFF process, as a material processing technique, can be used to fabricate fully functional near-net 3D components directly from their CAD models. The LSFF setup includes a positioning device, a laser, and a material deposition system. In this method, a laser beam is utilized as a heat source to form a small melt pool on a substrate placed on a work station which moves along a predefined trajectory. By adding the metallic material into the melt pool, a tiny track is formed as the heat source moves away and the molten added material solidified. LSFF has shown many advantages which have made this technique a potential candidate in many different fields such as coating, part repair, and rapid manufacturing.

Additive nature and unique laser beam characteristics as well as advances in rapid prototyping techniques, have made LSFF a unique fabrication technique with many superior features. LSFF can have an influential effect on the transition from mass production strategies to flexible low-volume-production manufacturing by which fabrication of components capable of functioning in multidisciplinary environments are possible. Despite all LSFF advantages, LSFF has several drawbacks which impose a number of restrictions on its full utilization in industry. LSFF, as an interdisciplinary technology, is governed by a large number of interrelated process parameters pertaining to the equipment and materials used. These interrelated parameters, which are highly sensitive to changes in the operating conditions, determine the physical quality and geometrical accuracy of the final product. Therefore, controlling these parameters is critical during the fabrication of an object using LSFF. In order to bring all variations effectively under control, it is necessary to understand

the relationships between these parameters and their effects on the final build-up. However, for the LSFF process in which a large number of sensitive and interrelated process parameters determine the quality of the final product, having a comprehensive model of the process can give a better understanding of the system behaviour and the correlation of the process parameters. For this purpose, first it is required to represent various physical phenomena involved in the LSFF process mathematically and then assembled them together based on their relationships through associated governing equations. As described in this chapter, the main governing equation of the LSFF process are continuity equation, momentum equation, heat conduction equation, concentration equation, strain and the constitutive equation for linear elastic materials.

Chapter 3

Multi-physics Modelling of Laser Solid Freeform Fabrication

Once a model of a system is available, it is possible to carry out various procedures to gain a better understanding of the system. Furthermore, such derived models give insight into the nature of the system behavior, and consequently, reduce time and complexity involved in experimental methods. The main theme of this chapter is to describe the development of a coupled time-dependent 3D numerical model of the LSFF process. The proposed modelling approach can be employed to dynamically predict geometrical characteristics of the deposited additive material, temperature distributions and thermal stress fields induced throughout the LSFF process as a function of process parameters and material properties. The last section of this chapter is devoted to the experimental verification of the developed model. The next section inclusively reviews studies which concern modelling of the LSFF process.

3.1 LSFF Numerical and analytical Modelling Approaches - a Literature Review

In analytical models, most of the solution strategies are based on the mathematical formulation only employing differential equations. Since solving these differential equations

for any complex or real-life problems are difficult or even in most cases impossible, significant simplifications involved in these types of modelling approaches are prevalent such as considering one-dimensional or steady-state models [31, 32]. In some less severe cases, the differential equations can analytically be solved by using numerical methods at the very end of the solution process. Although with the advent of high speed computers, numerical methods are now established solution strategies for complex real-life problems, still, using analytical methods for showing a specific point of view are preferred. For LSFF, Steen [16] described different basic analytical modelling approaches.

For an instantaneous stationary point source of energy Qpc_p assuming no heat exchange through convection or radiation, the solution of the heat conduction equation, Equation (2.5), is:

$$T = \frac{Q}{8(\pi\alpha t)^{2/3}} \exp\{-[(x-x')^2 + (y-y')^2 + (z-z')^2]/4\alpha t\} \tag{3.1}$$

where α (m^2/s) is thermal diffusivity, and (x', y', z') is the location of the heat source. The effect of different heat sources can be added using the superposition principle. Therefore, with the constant heat flow q supplied to the medium per unit time, the temperature at point (x, y, z) at any time is found by integrating Equation (3.1) over time. The final result is:

$$T(x,y,z,t) = \frac{q}{4(\pi\alpha d_r)} \operatorname{erfc}[\frac{d_r}{(4\alpha t)^{1/2}}] \tag{3.2}$$

where:

$$d_r = [(x-x')^2 + (y-y')^2 + (z-z')^2]^{1/2} \tag{3.3}$$

Using the solution for the continuous point source and integrating this over an area, it is possible to determine the temperature of a domain at any point during the heating process with a heat source of any geometry. In addition, using the same method for the point source expressed by Equation (3.2), a well-known Rosenthal solution for the moving heat source with a constant velocity along the x direction of a semi-infinite domain without radiation heat loss and melting is as follows:

$$T(x,y,z,t)-T_0=\frac{Q}{2\pi k}e^{-vx/2\alpha}\frac{e^{-v[(x^2+y^2+z^2)^{1/2}]/2\alpha}}{(x^2+y^2+z^2)^{1/2}} \tag{3.4}$$

where v (m/s) is the velocity of the moving heat source. There have been many contributions in the process modellings of different laser material applications within the last few decades. However, in this section the focus is mostly on the recent contributions to the field which are more related to the subject of this research. More information related to the various modelling approaches in laser material processing and brief review of stationary and dynamic models developed by different research groups are provided by Machwood et al. [39].

There are many numerical/analytical models developed more realistically within the framework of the LSFF governing equations. Several stationary and transient analytical and numerical thermal models have been developed in which various physical parameters related to the heat transfer phenomenon such as melt pool characteristics and geometry, interaction between melt pool and powder stream, thermal distribution throughout the process domain, and the effect of variations in the process parameters on the whole process were studied.

One of the first and most comprehensive LSFF modelling approaches for a single clad was proposed by Picasso et al. [40]. In this simple but realistic modelling strategy, the interactions between the powder particles, the laser beam, and the melt pool were considered. Their developed 3D analytical model could compute the melt pool shape, and also predicted the laser beam velocity and powder feed rate based on the other process parameters, including the laser power, powder stream geometry and clad height. To solve this stationary analytical model, certain assumptions were made. For instance, they considered the clad and the substrate thermo-physical properties to be the same and the latent heat effects were neglected. Likewise, in the models developed by Pinkerton et al. [31] and Han et al. [25], convective and radiation heat losses were ignored, and temperature independent thermo-physical properties, as well as a fully covered melt pool by the powder stream were assumed. Pinkerton et al. [31] developed an analytical model to calculate the geometry of the melt pool based on the Rosenthal equation, Equation (3.4). The geometry of the melt pool boundaries considered orthogonal to the direction of motion assumed arcs of a

circle. The model was solved for two sets of process parameters; one for the melt pool with boundaries forming a continuous circle, and the other for the melt pool with two different arcs of circles above and below the substrate in the plane orthogonal to the melt pool motion. Han et al. [25] developed a comprehensive model for the laser cladding process with coaxial powder injection. The proposed model in which the effects of the melting, evaporation, evolution of the free surface and powder injection were considered was ultimately used to study the effects of the process parameters on the melt pool geometrical characteristics. There are also several more analytical models solved numerically using the Finite Element Method (FEM) for single layer deposition [21, 27].

As many of the process parameters such as those related to the melt pool characteristics and microstructure of the fabricating part are difficult or impossible to be monitored experimentally; many research groups have also taken the approach of using an experimentally calibrated numerical model to investigate the effects of these parameters. Cho et al. [41] investigated the effect of the latent heat on the process. They numerically examined the temperature fields with and without considering the latent heat for a semi-infinite domain. Toyserkani et al. [27, 28] developed a 3D finite element (FE) model to study the effects of laser pulse shaping, traverse speed, and powder feed rate on the laser cladding process with powder injection for a single layer deposition. He et al. [34] also developed a 3D numerical model to study the temperature and velocity fields formed during the LSFF process. They used this model to study the interaction of the laser and powder particles as well as the effects of the laser powder, traverse speed, and powder feed rate on the clad geometry. In addition, the free surface movement of the melt pool was studied using the level-set method. Qi et al. [42] developed a 3D model of the process for a coaxial laser powder deposition system. The heat transfer mechanism, phase changes and fluid flow in melt pool were studied while temperature and fluid velocity were solved in a coupled fashion. The level-set method was implemented to detect the free surface of the melt pool. In this modelling approach the physical phenomena at the liquid-gas and solid-liquid interface were considered with the appropriate boundary conditions. Some assumptions were considered in this study to model the process, including that the liquid is considered an incompressible Newtonian fluid with a laminar fluid flow. The solid and liquid phases are

considered as a continuum domain with a zero velocity for the solid domain. The powder particles are immediately melted on the surface of the melt pool. Peryre at el. [43] also simulated the thermal specifications of the LSFF process using a two-step approach. The first step was to predict the morphology of the formed geometry of the additive material. The second step was allocated to the thermal analysis of the process. In their study, for the 2D description of powder heating using the coaxial nozzle, the model proposed by Qi et al. [42] was employed as the basis of the investigation by which they predicted the width and height of the deposited material based on the temperature distributions. The temperature distribution was determined using steady state calculations by the FE method. A simplified description of temperature in the melt pool was developed based on the geometrical specifications of the melt pool and the maximum temperature T_{max}. Maximum temperatures are obtained from the FE solutions. They used the following proposed expression for the temperature of the melt pool to find the melt pool depth, d (the melt pool area on the substrate is considered to have an elliptical shape):

$$T = T_m + \frac{1}{2}(T_{\max} - T_{melt})[1 + \cos(\pi(\frac{x^2}{(0.5w)^2} + \frac{y^2}{L_f^2} + \frac{z^2}{d^2}))] \quad \text{, for front semi ellipse} \qquad (3.5)$$

$$T = T_m + \frac{1}{2}(T_{\max} - T_{melt})[1 + \cos(\pi(\frac{x^2}{(0.5w)^2} + \frac{y^2}{L_r^2} + \frac{z^2}{d^2}))] \quad \text{, for rear semi ellipse} \qquad (3.6)$$

where w (m) is the melt pool width, T_{melt} (K) is the melting temperature, L_f (m) is the front part of the melt pool length, and L_r(m) is the rear part of the melt pool length. Then, the following equation was used to determine the height of the track for each element of the discretized domain:

$$\Delta h_{ij} = \frac{m_l \Delta l}{\rho V} \qquad (3.7)$$

where m_l (g/s.m^2) is the local powder feed rate, Δl (m) is the cell size, and V is the traverse speed of the laser beam and material deposition system. The experimental results were also used to check the corresponding numerical results and the related findings.

To the best knowledge of the author, while there are many papers concerned with experimental investigation of the LSFF process and its application to rapid prototyping of specific components [44, 45], there are only a few studies focused on the modelling of the multilayer LSFF process. Amongst these, Pinkerton et al. [46, 47, 48] experimentally studied the effects of the laser pulse width and pulse frequency on microstructure and surface finish of multiple-layer deposition of 316L steel. They also experimentally studied the interconnections between input parameters and final material dimensions, properties and surface finish in multilayer deposition using a 1.5 kW diode laser. The study of the effect of powder concentration distribution on the fabrication of a thin wall is another example of research related to the multilayer LSFF technology [49]. In this study, a model for the effect of powder concentration distribution on the fabrication of a thin wall was developed. Using this model along with the experimental analyses, the effects of the fluctuation of the powder feed rate, the concentration distribution, and the center lines of the powder jet with the laser beam on the geometry of a thin wall were investigated in a coaxial laser material deposition.

Among the few papers concerned with the modelling of the multilayer LSFF, Vasinonta et al. [50] developed a 2D numerical thermal model in which the effect of convective heat transfer from the wall surface and convective flows in the melt pool were not considered. Also, the laser beam was represented as a point source of heat, neglecting the laser energy distribution. On one hand, the length of the wall was assumed to be large enough in order to consider the melt pool size independent of the existence of the vertical free surface, while on the other hand the substrate was considered very large for acting as a thermal heat sink. Han et al. [51] established a transient mathematical model to study thermal and mass transportation phenomena during the repair process for a part with a rectangular hole. One of the prominent aspects of their study is the use of the level set method to consider the fluctuation of the melt pool surface during the evolution of the melt pool shape. Their 2D simulations in terms of maximum temperature and length of the melt pool for two consecutive layers were verified with experimental data. In their study, the effects of solidification, melting, surface tension, and Marangoni were considered. Costa et al. [52] developed a 3D FE model to study the influence of substrate size and idle time between the

deposition of consecutive layers on the microstructure and hardness of a ten-layer steel wall fabricated by LSFF. They used a step wise approach in which deposited material can be added to the model by activating a new group of elements at each time step. A rectangular cross section was assumed for the wall and the accuracy of the model was verified by the available data in the literature. The density, specific heat capacity and thermal conductivity were considered temperature dependent, and the effect of latent heat of fusion was also taken into account. A more comprehensive 3D transient FE model of a thin wall was developed by Hu et al. [21] to study the thermal behavior of the melt pool. They assumed that temperature dependent thermo-physical properties and the thermal load were in the form of the thermal flux density with a normal distribution. The latent heat of fusion was also taken into account, while because of rapid melting and solidification, the convective flow of heat in the melt pool was ignored. In these modelling approaches, the focus was on the thermal behavior of the melt pool and the models did not predict the geometry of deposition layers during a multilayer LSFF process.

However, in these reported modelling approaches, the geometry of the deposited materials are defined in advance (i.e., a thin wall with a rectangular cross section), or in a dynamic fashion, a new group of elements at each time step is activated to build up a thin wall with a rectangular cross section.

Since in the LSFF process the contraction caused by the thermal strains results in the deformation, and consequently residual stresses, several articles have discussed the effects of the thermal stresses on the mechanical-metallurgical properties of parts fabricated using layered manufacturing and particularly LSFF [9, 10, 53].

A number of research groups have conducted studies to integrate stress fields induced by thermal gradients into modelling approaches as a major phenomenon which determine several mechanical – metallurgical qualities of the final part. Mughal et al. [54] developed a 2D FE thermo-mechanical model with a distributed moving heat source to predict the residual stress in solid freeform fabrication employing direct metal deposition. Nickel et al. [55] studied the effect of deposition patterns on deformations and thermal stresses produced during the laser deposition process. Their approach was a combination of experiments and numerical modelling using FE method. To simplify their model, material deposition was not

considered, nor was latent heat or the effects of radiation and convection on the process. In addition, all boundaries except the bottom surface of the substrate were assumed to be insulated. Another major simplification in their study was related to the laser beam as the heat source. In the FE model, the entire deposition line was heated and then cooled at the same time prior to the next deposition. Jendrzejewski et al. [56, 57] studied the stress fields in laser cladding (for both single and double layer depositions) using a decoupled time-dependent FE model. In their proposed model, the additive material dynamically added to the process domain with a predefined rectangular cross section. In addition, the substrate and additive material were discretized with large element sizes. They studied the effects of time delay for the second layer deposition and preheating. The effect of preheating was studied in general without investigation of the intensities and dispersions throughout the deposition path. Ghosh et al. [37] developed an uncoupled 3D transient FE modelling approach to study macro-micro stresses induced by thermal distributions. Simulations and experiments were performed for single layer deposition of one and two adjacent tracks. Additive material was incorporated to the model by activating a new group of brick type elements at each time step. This resulted in a track with a rectangular cross section while a Gaussian distribution was considered for the laser beam intensity profile. The model was experimentally verified, although the laser power and properties of the additive materials used in the experiments and simulations were different.

In the next section, a 3D time-dependent multi-physics numerical modelling approach for the multilayer LSFF process by powder injection system is described. For this purpose, various assumptions and adjustments are considered in order to have a simple yet realistic mathematical approach while incorporating the effects of different process parameters into the model, such as Marangoni phenomena, power attenuation, the effect of angle of incidence (Drude reflectivity), and the effect of external forces or displacements. An algorithm is then described in detail to incorporate the deposition of additive materials into the process domain on planar as well as non-planar surfaces. This modelling approach is used to simulate a four-layer thin wall and to study the temperature distribution and thermal stress field. The numerical results including geometrical features of the deposited material and thermal behaviors of the model, as well as the deflection of the substrate caused by the

thermal stress are verified by experimental data which will also be addressed in the following sections.

3.2 A Time-Dependent Multi-Physics Model of the LSFF Process: Mathematical Model

In this section, different steps of a numerical approach for multi-physics modelling of the LSFF process by powder injection will be described. In this approach, the shape of each deposited layer is predicted in a decoupled fashion while the temperature distributions and the temporal thermal stress fields are dynamically determined using a coupled solution strategy.

The transient temperature distribution $T(x,y,z,t)$ throughout the domain of the LSFF process can be obtained from the 3D heat conduction equation along with its associated boundary conditions as explained in Chapter 2. In this approach, assuming linear elastic material, the thermal stress fields are obtained using Equations (2.8) and (2.9). It should be noted that the heat conduction equation cannot properly represent the heat transfer mechanism in the melt pool zone which is dominated by convection resulting from Marangoni flows driven by surface tension gradients. For an accurate formulation, the melt pool and solid zones can be considered as separate regions and coupled through moving boundary conditions [58]. However, it is possible to formulate the heat transfer system of the melt pool as a part of the whole process domain, and also indirectly to take into account other physical effects encompassed by other process governing equations considering appropriate assumptions [59, 60].

3.3 Adjustments and Assumptions on the Boundary Conditions

To fit the governing equations and their associated boundary conditions to the LSFF process while the main phenomena involved are considered, some adjustments as well as assumptions for reducing the complexity of the problem should be taken into account. To incorporate the effects of different operating parameters into the mathematical

representation of the LSFF process as well as to simplify the solution process, the following adjustments and assumptions are considered.

- *Power Distribution of a Moving Laser Beam*: For the laser beam power distribution, a circular Gaussion TEM_{00} is considered. The laser power distribution in a polar system, $I(r)$ (W/m^2) for this case is defined as:

$$I(r) = \delta_f \frac{2P_l}{\pi r_l^2} \exp\left[\frac{-2(r^2)}{r_l^2}\right] \tag{3.8}$$

where r_l (m) is the laser beam radius on the substrate, r (m) is the distance from the center of the laser beam, and P_l (W) is the laser average power. δ_f is zero when the laser beam is off and is one when the laser beam is on. For a pulsed laser, laser power is $P_l = E.f$, where E (J) is the energy per pulse and f (Hz) is the laser pulse frequency. The effect of the moving laser beam is taken into account by updating its position r on the surface of the substrate based on the relative velocity of the laser processing head and the substrate as follows:

$$r = [(x - \int_{t_0}^{t} u_x dt)^2 + (y - \int_{t_0}^{t} u_y dt)^2 + (z - \int_{t_0}^{t} u_z dt)^2]^{1/2} \tag{3.9}$$

where u_x (m/s), u_y (m/s) and u_z (m/s) are the continuous velocities of the center of the laser beam in the x, y and z directions, respectively.

If the laser beam strikes a non-planar surface, the circular beam is projected on the non-planar surface accordingly.

- *Latent Heat of Fusion and Marangoni Flow*: The effect of latent heat of fusion on the temperature distribution is considered by modifying the specific heat capacity c_p (J/Kg.K) [61].

$$c_p^* = \frac{L_f}{T_m - T_0} + c_p \tag{3.10}$$

where L_f (J/Kg) is latent heat of fusion, T_m (K) is melting temperature, and T_o (K) is ambient temperature.

Marangoni flow, which is the effect of fluid motion due to the thermo-capillary phenomenon, is also considered for calculating the melt pool boundary by modifying the thermal conductivity K based on the method recommended by Lampa et al. [59]. The recommended correction factor is 2.5 obtained from the experimental data.

- *Power Attenuation*: A portion of the laser energy is directly absorbed by the substrate. The powder particles also absorb and carry some of the laser energy into the melt pool. To consider this effect in the modelling, a method developed by Picasso et al. [40] is used. Based on this method, the total absorbed power by the substrate P_w can be defined as:

$$P_w = \beta_e P_l \tag{3.11}$$

where P_l (W) is the total power of the laser, and β_e is the effective absorption factor. Based on this method, an effective absorption factor, β_e can be calculated as:

$$\beta_e = \beta_w(1-\xi) + \eta_p \beta_p \xi + \eta_p \beta_p (1-\beta_w)(1-\xi)\xi \tag{3.12}$$

where ξ is the ratio of the attenuated power to the laser power, β_w is the substrate absorption factor, β_p is the powder absorption factor, and η_p is the powder efficiency which can be written as:

$$\eta_p = \frac{A_{jet}^{melt}}{A_{jet}} \tag{3.13}$$

where A_{jet} (m^2) is the powder stream surface, and A_{jet}^{melt} (m^2) is the intersection of the melt pool and the powder stream area on the substrate, as shown in Figure 3.1.

Furthermore, ξ can be given by:

$$\xi = \frac{P_a}{P_l} = \frac{\dot{m}}{2\rho_p r_l r_p v_p \cos(\theta_{jet})} \qquad \text{if } r_{jet} < r_l \tag{3.14a}$$

$$\xi = \frac{P_a}{P_l} = \frac{\dot{m}}{2\rho_p r_{jet} r_p v_p \cos(\theta_{jet})} \qquad \text{if } r_{jet} \geq r_l \tag{3.14b}$$

where P_a (W) is the attenuated power, $\dot{m}$ (kg/s) is the powder feed rate, ρ_p (kg/m) is the powder density, r_p (m) is the radius of the powder particles, r_l (m) is the radius of the laser beam on the substrate, r_{jet} (m) is the radius of the powder stream on the substrate, v_p (m/s) is the velocity of the particles, and θ_{jet} (deg.) is the angle between the powder stream and the surface of the substrate.

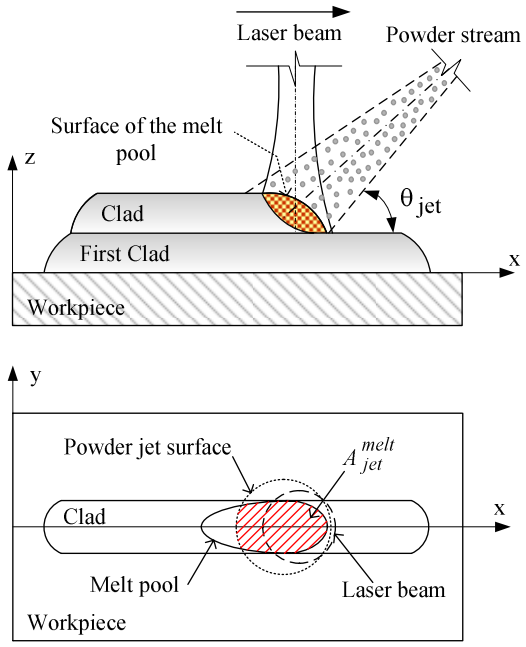

Figure 3.1 Schematic diagram of the laser beam and powder stream interaction during the multilayer LSFF process

- *Effect of Angle of Incidence*: In this study, the effect of the angle of incidence of the laser beam is considered for non-planar surfaces. Assuming an s-polarized beam, the reflectivity factor can be obtained by [16]:

$$R = \frac{(n - \cos\varphi_i)^2 + k^2}{(n + \cos\varphi_i)^2 + k^2} \tag{3.15}$$

where R is the reflectivity, φ_i is the incident angle, n is the refraction coefficient, and k is the material extinction coefficient. Assuming an opaque material (e.g., metal), the relation between the reflectivity and absorptivity is as follows:

$$\beta = 1 - R \tag{3.16}$$

For the sake of simplicity, an average angle of incidence can be calculated for each deposited layer based on the boundary of a non-planar surface within its intersection with the laser beam area on the top surface of each deposited layer. Figure 3.2 shows a laser beam irradiating a deposited track, including a typical laser ray direction and the angle of incidence during the multilayer LSFF process.

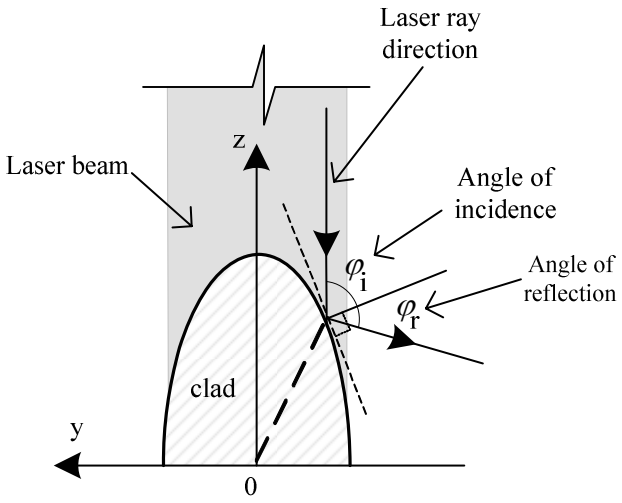

Figure 3.2 Angles of incidence and reflection

- *Combined Heat Transfer Coefficient*: A combined radiative and convective heat transfer coefficient (h_c) is used to reduce computation time, since the radiation term in the boundary condition makes the analysis highly non-linear [21]:

$$h_c = 2.41 \times 10^{-3} \varepsilon_R T^{1.61} \tag{3.17}$$

For other thermo-physical and optical properties, their averages throughout the process over the process temperatures were calculated to consider their temperature dependency.

- *Elastic Isotropic Materials*: For elastic isotropic materials, 36 independent components of D_{ijmn} reduce to just two independent components. Therefore, with this assumption the mechanical and thermal strains can be expressed as:

$$\varepsilon_{11}^{M} = \varepsilon_x \quad ; \quad \varepsilon_{22}^{M} = \varepsilon_y \quad ; \quad \varepsilon_{33}^{M} = \varepsilon_z$$

$$\varepsilon_{31}^{M} = \varepsilon_{13}^{M} = \frac{\gamma_{yz}}{2} \quad ; \quad \varepsilon_{12}^{M} = \varepsilon_{21}^{M} = \frac{\gamma_{zx}}{2} \quad ; \quad \varepsilon_{23}^{M} = \varepsilon_{32}^{M} = \frac{\gamma_{xy}}{2} \tag{3.18}$$

$$\varepsilon_{mn}^{T} = \alpha(T - T_{in})\,\delta_{mn} \qquad (m, n = 1,2,3) \tag{3.19}$$

where γ (m/m) is the shear strain, T_{in} (K) is the initial temperature, α (m/m.K) is the linear coefficient of thermal expansion, and δ_{mn} is the Kronecker delta defined as:

$$\delta_{mn} = \begin{cases} 1 & \text{for } m = n \\ 0 & \text{for } m \neq n \end{cases} \tag{3.20}$$

Therefore, the stresses in terms of the strains represented by the thermoelastic constitutive equations, Equation (2.9), can be given by [62]:

$$\varepsilon_{ij} = \frac{1+\nu}{E}\sigma_{ij} - \frac{\nu}{E}\delta_{ij}\sigma_{kk} + \alpha\,\Delta T\,\delta_{ij} \qquad (i, j, k = 1,2,3) \tag{3.21}$$

where ν is Poisson's ratio.

To express the stresses in terms of the strains in the thermoelastic constitutive equations, Equation (3.21) can be rewritten as:

$$\sigma_{ij} = \frac{E}{(1+\nu)(1-2\nu)}[\nu\delta_{ij}\varepsilon_{kk} + (1-2\nu)\varepsilon_{ij} - (1+\nu)\alpha\,\Delta T\,\delta_{ij}] \qquad (i, j, k = 1,2,3) \tag{3.22}$$

Displacement equations and compatibility equations are the other two governing equations of thermoelasticity. Displacement equations in index notation are defined as [62]:

$$G\nabla^2 d_i + (\frac{2\nu G}{1-2\nu} + G)\,d_{k,ki} - \alpha(\frac{6\nu G}{1-2\nu} + 2G)\Delta T_{,i} + F_i = 0 \qquad (i, j, k = 1,2,3) \tag{3.23}$$

where u (m) is the displacement, and F (N) is the external force. The index notation $\phi_{,i}$ means scalar gradient of ϕ, and $\phi_{k,ki}$ means gradient-divergence of ϕ. The compatibility equations in terms of the stress and in index notation are also defined as:

$$\nabla^2\sigma_{ij}+\frac{1}{1+\nu}\sigma_{kk,ij}+\alpha E\left(\frac{1}{1-\nu}\nabla^2(\Delta T)\delta_{ij}+\frac{1}{1+\nu}\Delta T_{,ij}\right)$$

$$=-\left(\frac{\nu}{1-\nu}F_{k,k}\delta_{ij}+F_{i,j}+F_{j,i}\right) \qquad (i,j,k=1,2,3) \qquad (3.24)$$

By solving Equations (3.22), (3.23) and (3.24) along with the appropriate boundary conditions and process governing equations, the thermal strains and stresses throughout the part fabricated by LSFF can be calculated.

Implementing the adjustments and the assumptions listed above, and considering a moving laser beam on the surface of the substrate with a constant velocity in the *xy* plane (i.e., $u_z=0$), by inserting Equations (3.8), (3.11) and (3.17) into Equations (2.13) and (2.14), the final boundary condition for governing thermal equation is derived as:

$$-K(\nabla T\cdot n)\big|_{\Re}=\frac{2}{\pi r_l^2}\delta_f\beta_e P_l\exp\left[\frac{-2[(x-u_x t)^2+(y-u_y t)^2]}{r_l^2}\right]-h_c(T-T_0) \text{ if } \Re\in\Lambda \quad (3.25)$$

$$-K(\nabla T\cdot n)\big|_{\Re}=-h_c(T-T_0) \text{ if } \Re\notin\Lambda \qquad (3.26)$$

3.4 Modelling Architecture

To solve the LSFF mathematical model while considering the effect of additive material, a strategy is contrived by which the 3D geometry of each layer deposited either on planar or non-planar surfaces can be predicted throughout the deposition process. This strategy comprises two main phases. The first phase calculates the temperature distribution and the strain-stress fields throughout the LSFF domain by solving the governing equations under the defined boundary conditions. The second phase then employs the results of the thermal analysis to predict the geometry of the deposited materials in a dynamic fashion for the multilayer LSFF deposition process. The two phases will be explained in the next two sections.

3.5 Solution Strategy of Mathematical Model

The analytical solution of the governing equations and their associated boundary conditions represented by Equations (2.5), (2.8), (2.9), and (3.8) to (3.26) is only possible for regular geometries under regular boundary conditions (i.e., specific and well-behaved). For most practical problems involving irregular geometries and/or complicated boundary conditions and material properties, it is not generally possible to obtain analytical mathematical solutions. Such problems can be solved using numerical techniques, in particular FEM. In this work, the governing equations and their boundary conditions are complicated due to the highly irregular 3D geometries of the deposited materials and substrate, interconnected operating parameters and temperature dependent mechanical-material properties, and a moving heat source with a Gaussian distribution; the FEM is therefore employed to solve these equations.

3.6 Three Dimensional Transient Geometry Prediction of Deposited Material

In this section a method is introduced by which it is possible to predict the geometry of the deposited materials and also incorporate the effect of the additive materials into the multilayer LSFF modelling. This method consists of three main steps as follows:

- Detection of the transient melt pool boundary
- Incorporation of additive material into the modelling domain
- Revision of the FE model based upon the updated geometry

A major difference between the single clad geometry creation proposed by Toyserkani et al. [27] and a multilayer clad geometry creation proposed in this work arises from the fact that in the single layer deposition, the melt pool boundary is assumed to be placed on a planar surface normal to the z coordinate, whereas in the multilayer deposition the melt pool surface is not planar, as shown in Figure 3.1. This difference requires the development of a

new methodology for incorporating the additive material for the second and subsequent layer depositions.

3.6.1 Detection of Transient Melt Pool Boundary

To incorporate the additive materials into the modelling domain, the boundary of the moving melt pool on the substrate must be obtained based on the numerical solution of Equation (2.5) along with its related boundary conditions for all time steps during the LSFF process (Note that Equation (2.8) is solved, coupled with Equation (2.5), to obtain the strain/stress field simultaneously). In this approach, the substrate is 'sliced' into r cross sections in the x direction, as shown in Figure 3.3a for a substrate with a rectangular cross section. Each cross section is afterwards discretized into m by n elements in the yz plane. Therefore, for each node denoted by a_{ij} $(i = 1,2,...,m;\ j = 1,2,...,n)$, its corresponding temperature and coordinates are available from the solution of the FE model and the geometry of the substrate. It should be noted that some of these nodes (referred to as void elements shown in Figure 3.3b) do not belong to the substrate; therefore, their corresponding temperature is not considered in the melt pool boundary detection process. In general, each slice and its corresponding temperature can be represented by:

$$S_k(m \times n) = \left[a_{ij} \right]_{t=t_s} \qquad (i = 1,2,\ldots,m;\ j = 1,2,\ldots,n;\ k = 1,2,\ldots,r) \tag{3.27}$$

$$T_k(m \times n) = \left[T_{ij} \right]_{t=t_s} \qquad (i = 1,2,\ldots,m;\ j = 1,2,\ldots,n;\ k = 1,2,\ldots,r) \tag{3.28}$$

where t_s refers to a sampling time step. In order to find the melt pool boundary on the upper surface of the substrate, the temperatures of all elements of S_k, which are placed on the solid/void interface, are found (i.e., nodes which belong to the substrate and are located on its upper boundary). The coordinates of the selected nodes and their corresponding temperatures are used to form matrices H and T as follows:

$$H(r \times m) = \left[h_{ki} \right]_{t=t_s} \qquad (i = 1,2,\ldots,m;\ k = 1,2,\ldots,r) \tag{3.29}$$

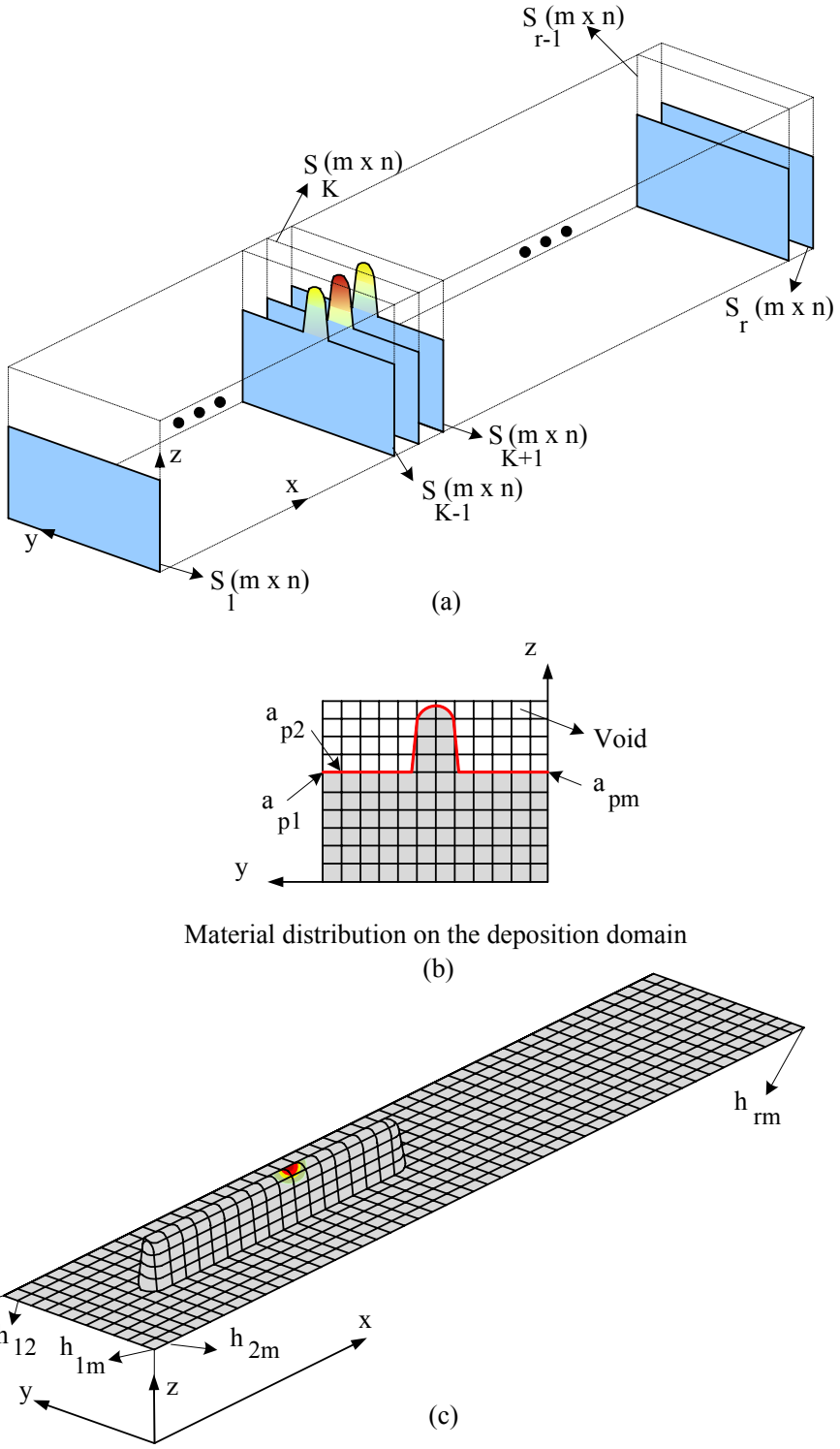

Figure 3.3 Detection of the melt pool boundary on non-planar surface: a) process domain, b) a cross section in the *yz* plane, c) upper surface of the substrate

$$T(r\times m)=\left[\ T_{ki}\ \right]_{t=t_s} \qquad (i=1,2,\ldots,m;\ k=1,2,\ldots,r) \tag{3.30}$$

where h_{ki} and T_{ki} are the heights and temperatures of the nodes located on the top surface of the substrate. By assembling these selected nodes of all slices in *xyz* coordinates along with their temperature T_{ki}, the upper surface of the substrate (including the melt pool boundary) can be developed at sample time t_s as shown in Figure 3.3c.

The position of each node in *xyz* coordinates is determined using h_{ki} along the z direction, and their x and y coordinates, which are the elements of the tensor Ω:

$$\Omega_{ki}=x_{k1}\,y_{1i} \tag{3.31}$$

where x_{i1} and y_{1j} are the elements of the following vectors:

$$\vec{X}=\begin{bmatrix}1 & 2 & \cdots & x_r\end{bmatrix}^T \tag{3.32}$$

$$\vec{Y}=\begin{bmatrix}1 & 2 & \cdots & y_m\end{bmatrix} \tag{3.33}$$

At this stage, the temperature distributions on the upper surface of the substrate are available at all time steps.

3.6.2 Incorporation of Additive Materials into Modelling Domain

Once the melt pool surface is obtained at each time step, a thin layer of material with thickness Δh is added to the nodes with temperatures higher than the melting temperature. These nodes must also be located on the intersection of the powder stream and the melt pool region. This concept can mathematically be represented by the following expressions:

$$h_{new}|_{\Omega}=h+\Delta h|_{\Omega} \quad at \quad (x_h,y_h,z_h)\in A_{jet}^{melt} \tag{3.34}$$

$$A_{jet}^{melt}=\left\{(x,y,z)|T_{(x,y,z)}\geq T_{melt}\cap(x,y,z)\in A_{jet}\right\} \tag{3.35}$$

where T_{melt} is the melting temperature of the substrate, and (x_h,y_h,z_h) are the coordinates of the nodes located on the intersection of the melt pool and powder stream. If this procedure continues for all consecutive time steps, a clad will be created. This method is schematically

illustrated in Figure 3.4. The height Δh of the thin layer of material deposited at each time step into the LSFF domain, as shown in Figure 3.4, can be calculated using the following mass conservation equation [27].

$$\Delta h = \frac{\dot{m}\,\Delta t}{A_{jet}^{melt}\,\rho_p} \tag{3.36}$$

where Δt (s) is the time step.

3.6.3 Revision of FE Model Based Upon the Updated Geometry

The FE model should be updated after each layer deposition based on the new geometry formed. The updated FE model will then be used for the next numerical analysis to determine the thermal and stress-strain fields, and consequently, to obtain the boundary of the melt pool for the subsequent clad creation. In order to facilitate the FE modelling, a standard geometry is fitted to the formed clad geometry created by the proposed material deposition method. There are different methods for doing this task. One of the methods is Fitzgibbon's approach [63], which is based on the least squares minimization technique. In this approach, an ellipse can be fitted into the border. An ellipse can be represented by an implicit second order polynomial as:

$$F(x,y) = p_1x^2 + p_2xy + p_3y^2 + p_4x + p_5y + p_6 = 0 \tag{3.37}$$

where p_1 to p_6 are coefficients of the ellipse and (x, y) are coordinates of points that form the ellipse. These coefficients can be written in vector notation as:

$$P = [p_1, p_2, p_3, p_4, p_5, p_6] \tag{3.38}$$

$$X = [x^2, xy, y^2, x, y, 1] \tag{3.39}$$

As a result, Equation (3.37) can be written as:

$$F_p(X) = P \cdot X \tag{3.40}$$

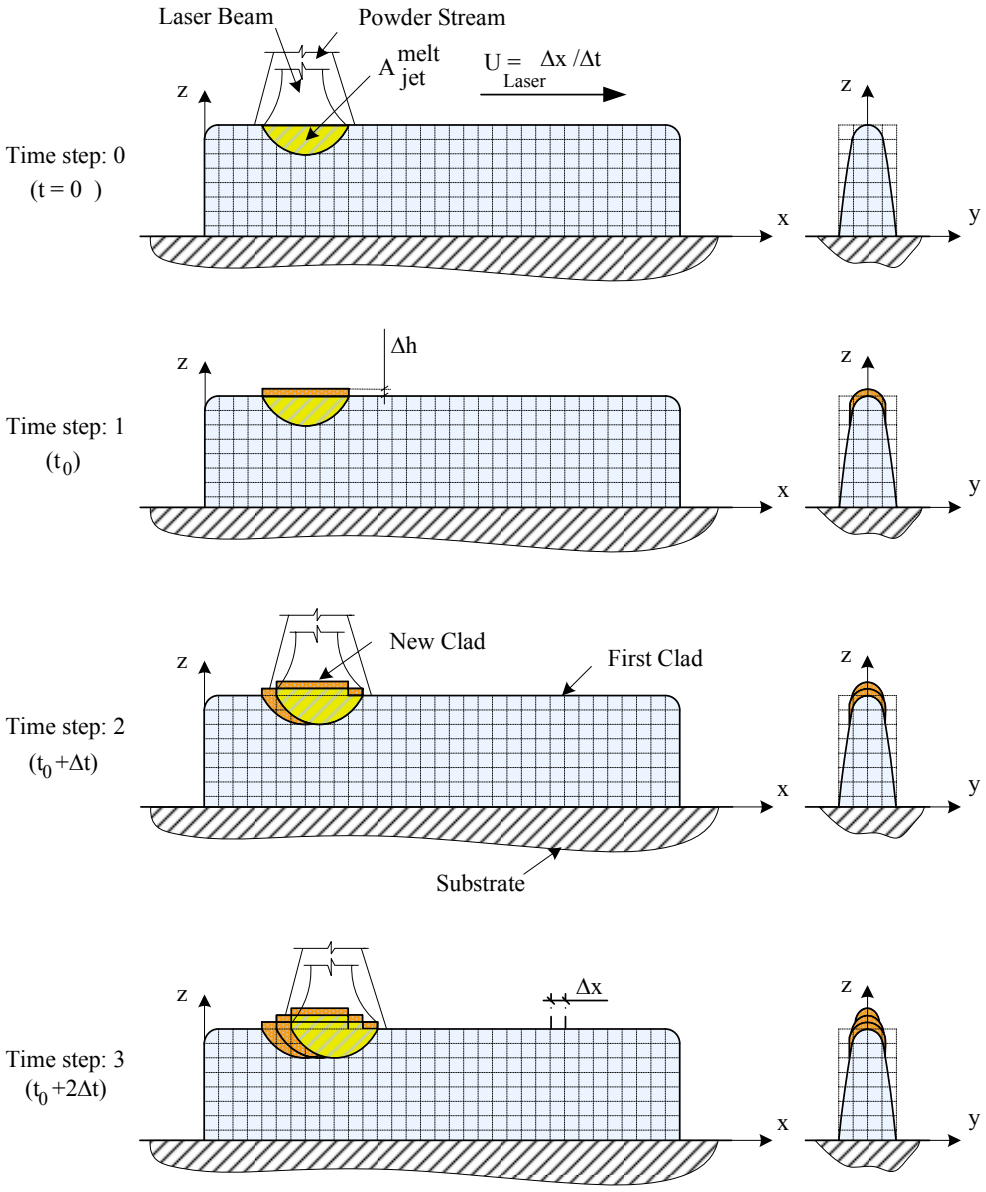

Figure 3.4 Material deposition method in the multilayer LSFF process modelling

In order to find the associated coefficients, a least squares minimization on N points (x_i, y_i), $i = 1, \ldots, N$ will be carried out. This minimization can be represented by the following equation:

$$\min \sum_{i=1}^{N} F(x_i, y_i)^2 = \min \sum_{i=1}^{N} (X_i \cdot P)^2 \tag{3.41}$$

Equation (3.41) can be solved directly by the standard least squares method, along with its associated constraint given by the following equation:

$$4p_1p_3 - p_2^2 = 1 \tag{3.42}$$

The output of this minimization will be the ellipse coefficients of Equation (3.37). Using this technique, a standard geometry can be fitted to the clad geometry created by the proposed additive material deposition method as shown in Figure 3.5.

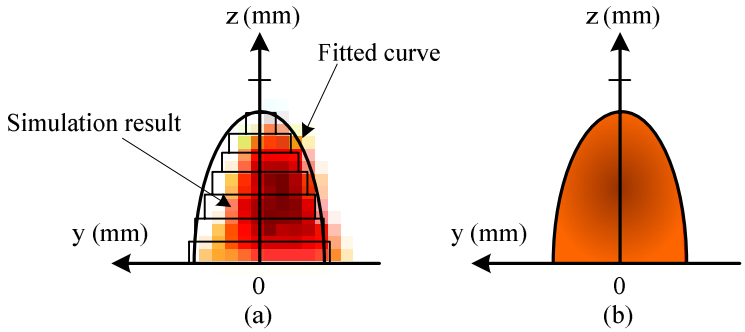

Figure 3.5 Fitting a standard geometry to the clad: a) simulation result, b) fitted object

The temperature of the deposited material formed on the surface of the substrate is considered the same as the corresponding nodes on the under surface at the final time step. Since the deposited material added to the process domain puts extra energy into the system, the total energy absorbed by the substrate (Equation (3.11)) should be updated by deducting this extra energy, which can be calculated using the following equation:

$$p_{extra} = mc_p\Delta T = \sum_{i=0}^{i=L/\Delta x} A\rho_p \Delta x c_p (T_n - T_0) \tag{3.43}$$

where A (m^2) is the clad cross section area, Δx (m), as shown in Figure 3.4, is the clad length created in each time step, T_n (k) is temperature of each node on the substrate underneath the clad created, and L (m) is the final length of the clad. The revised geometry

and its thermal distribution will be used for the next FE analysis, which is the first step of the modelling process for the next clad layer.

To conclude this section, the proposed method for solving the governing equations of the multilayer LSFF process and the algorithm for the material deposition throughout the process is summarized in the flowchart shown in Figure 3.6.

3.7 Coupled Thermal and Strain/Stress Modelling of Multilayer LSFF Process using Proposed Algorithm

To verify the method proposed in the previous section, a four-layer thin wall built up using LSFF on a 25×20×5 mm substrate was modeled. For this purpose, COMSOL Multiphysics 3.2a (www.comsol.com) was employed to solve the governing equations and their corresponding boundary conditions introduced in the previous section.

A time-dependent solver (Conjugate gradients), which is an implicit differential-algebraic equation (DAE) solver with automatic step size control, is used. The solver supports second order time derivatives as well as iterative solutions, and is suitable for multiphysics problems. The absolute tolerance parameters for time-dependent problems are problem dependent; the default value used is 0.001. Having the thermal distribution throughout the process domain from the FE solution, the melt pool surface can be detected and obtained at any time step for use in the next step, which is the geometrical prediction of the deposited material. To implement the proposed method for the incorporation of the additive material into the modelling scheme, a combined code was developed using MATLAB (www.mathworks.com), and the interface between MATLAB and COMSOL.

3.8 Numerical Parameters and Simulations

The material properties of AISI 304L steel were considered for both the substrate and powder particles. The absorption factor (β_w) of a flat surface, as a function of temperature [40] was used for calculation of the absorption factor at any angle of inclination. Table 3.1 lists the main process parameters and their values used for the simulation process.

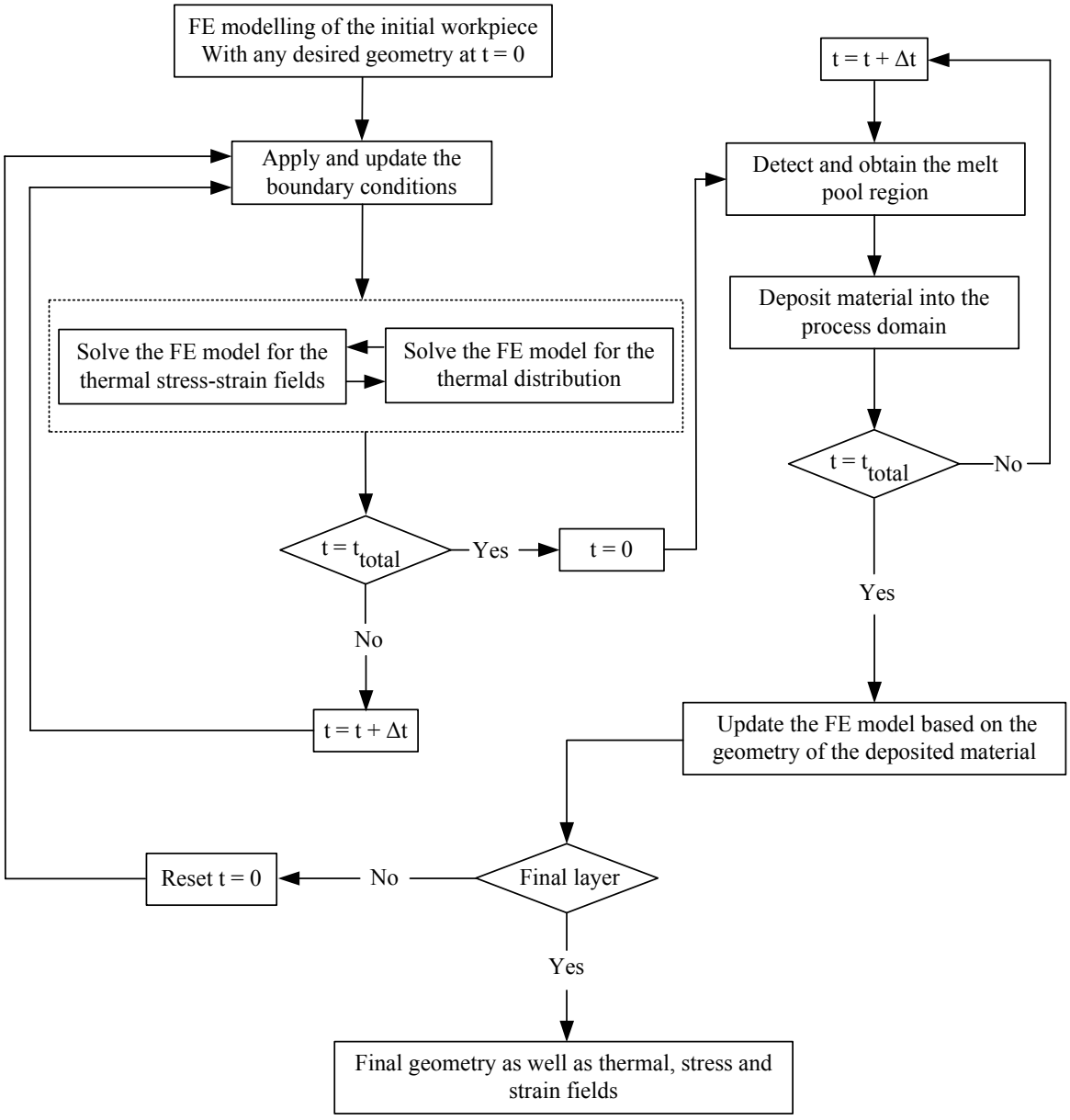

Figure 3.6 Flowchart of the proposed algorithm for a dynamic geometrical, thermal, and strain/stress fields prediction in multilayer LSFF process

Four-node tetrahedral elements were used to discretize the solid domain. To obtain the optimum number of elements in the model, a convergence test was conducted. This test was performed by increasing the number of elements in the FE model until the numerical solutions for the maximum temperatures and thermal stresses, throughout the process domain and time, converged. The results for the convergence tests are shown in Figure 3.7 and Figure 3.8 for the maximum temperatures and thermal stresses, respectively. In addition, all required element quality checks of the FE model were automatically performed to assure the accuracy of the model. Based on the results of the convergence test, the final discretized model for the first layer deposition has 82,025 elements and 484,076 degrees of freedom.

Table 3.1 Process parameters

Process parameter	**Value**	**Unit**
$\dot{m}$ - Powder feed rate	2	g/min
P - Laser Power	300	W
r_{jet} - Radius of the powder jet on the substrate	7.5e-4	m
r_l - Radius of the laser beam on the substrate	7.0e-4	m
T_0 - Ambient Temp.	298	K
T_m - Melting Temp.	1695	K
U - Process speed	1.5	mm/s
ρ_p - Powder density	7850	kg/m^3

Since the temperature distribution at the top surface of the model is of interest (owing to the melt pool and HAZ dimensions compared to the process domain), finer meshes were used on the top surface instead of through the whole body of the model as shown in Figure 3.9. This is useful to prevent increasing the number of elements unreasonably throughout the process domain as well as computational time.

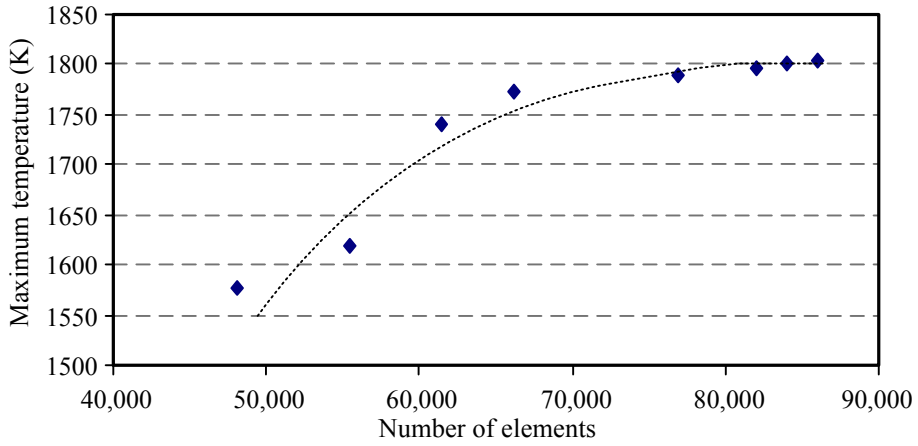

Figure 3.7 Convergence test for the time-dependent maximum temperature

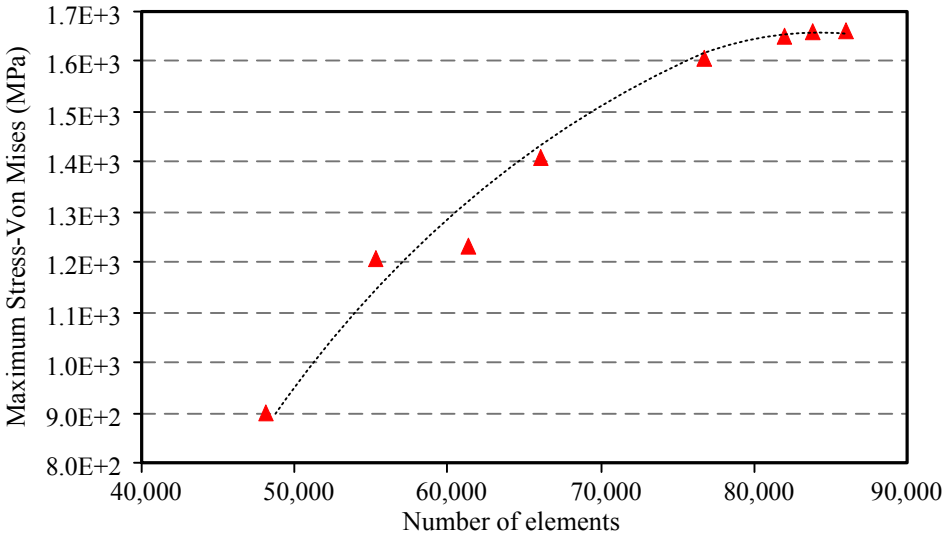

Figure 3.8 Convergence test for the time-dependent thermal stresses

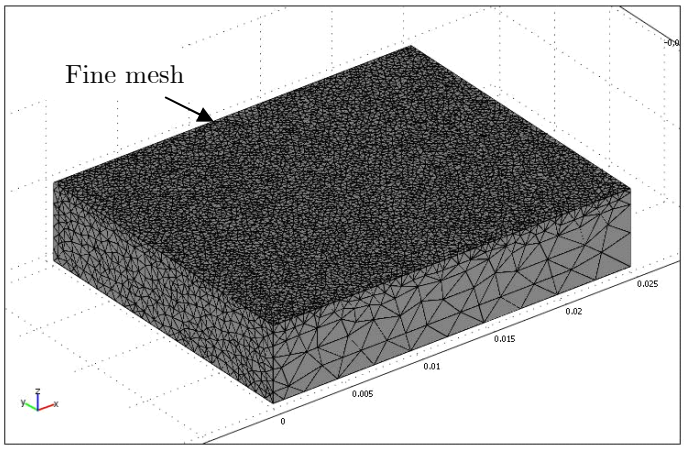

(a)

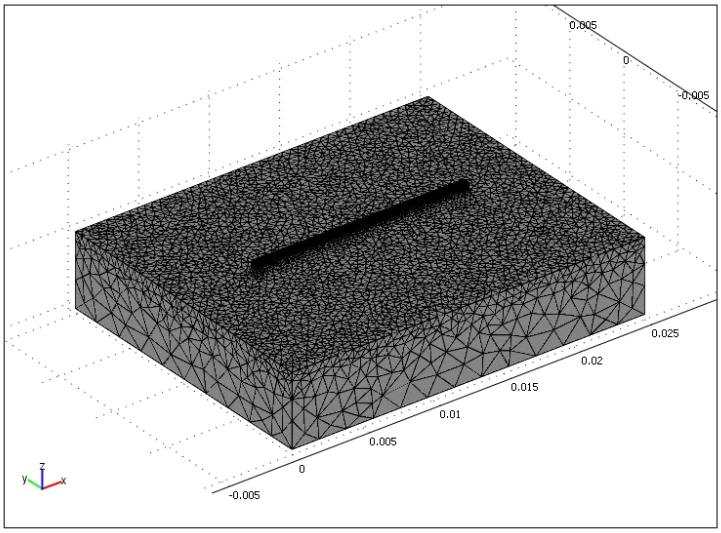

(b)

Figure 3.9 Discrete model for the FE analyses of the first and fourth layers

The laser beam was set to traverse a straight line on the substrate with starting and stopping points of (5, 0, 5) mm and (20, 0, 5) mm, respectively, relative to the coordinate system schematically shown in Figure 3.10. Since in the experimental process, a finite time is required to turn off the laser and return it to its home position for the next layer deposition, to make the numerical analysis identical to the experimental process, the simulation for the build-up of each layer was performed in a 20 s time span in which the laser is on and off for consecutive 10 s intervals. Figure 3.10 also shows the fabrication time plan for the thin wall with the status of the laser beam relative to the substrate. The temperature distribution and the stress-strain fields of the last time step of each simulation pass were considered as the initial condition for the next simulation pass.

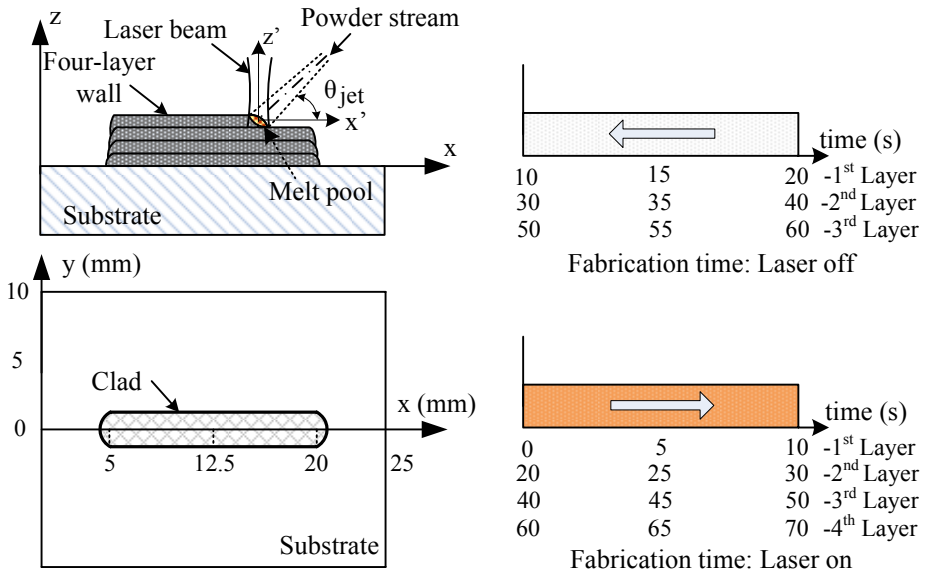

Figure 3.10 Schematic diagram of a four-layer wall fabrication using the LSFF process with its fabrication time plan

To consider the effect of angle of incidence on the process, the effective absorption factor β_e expressed by Equation (3.12) was calculated for each layer (a complete list of physical and thermo-physical properties of material used for calculation of β_e and other parameters in this study are provided in the literature [16, 33, 36]). Therefore, the powder catchment efficiency η_p was required to be updated for each layer based on the geometrical specifications presented in Equation (3.13) and shown in Figure 3.1. Figure 3.11 and Figure 3.12 show the

effective absorption factors and powder catchment efficiencies calculated for each layer from layer 1 to layer 4 (considering computational errors imposed by geometrical assumptions). As shown in these figures, the powder catchment efficiency increases for the upper layers, which can be explained by the increased melt pool surface due to temperature increase, while the effective absorption factor decreases because of the effect of angle of incidence in upper layers as explained in the preceding sections.

By solving the LSFF mathematical model using FEM, the temperature distributions and stress fields can be found throughout the deposition process for any time step. For instance, Figure 3.13 and Figure 3.14 show temperature distributions associated with the first and fourth layers at one specific time step. Figure 3.13 shows the temperature distribution prior to adding the layer to the geometrical domain and Figure 3.14 shows the temperature distribution on layer 3 prior to adding the fourth layer to the domain at $t = 5$ s. It should be noted that the boundary of the melt pool is obtained through the thermal analysis and then the associated layer is added to the process domain.

The geometrical results obtained from the algorithm, developed for the material deposition of a four-layer thin wall, are shown in Figure 3.15. As explained, using this numerical approach, it is possible to predict 3D geometries of the deposited material at any time step. Figure 3.15a shows the longitudinal views of the additive material depositions for the first and second layers at t=10 s and t= 28.5 s. Figure 3.15b also depicts the final profile of each layer in the xz plane as well as a cross section of the final build-up. Another numerical result presented in this section is the displacement of the substrate. Figure 3.16 also shows maximum displacements of the substrate at $x = 2.5$ mm throughout the process for each layer along with x, y and z coordinates.

3.9 Verifications of numerical results

Numerical methods, as a solution strategy, inherently include errors such as those resulting from approximation and rounding. Consequently, it is common practice to verify and check the accuracy of the numerical results using experimental or, if it is possible, analytical counterparts. Specifically, as described in the preceding section, LSFF is a complex process which needs several assumptions and simplifications throughout its modelling. Therefore, the

accuracy and reliability of the numerical results (i.e., the numerical model) were verified with the experimental results performed with the same operating parameters and conditions used in the simulations. The modelling results were verified in terms of the temperature and stress-strain fields. The accuracy of the algorithm proposed for the material deposition was also checked with the appropriate experimental data that all will be addressed in this section.

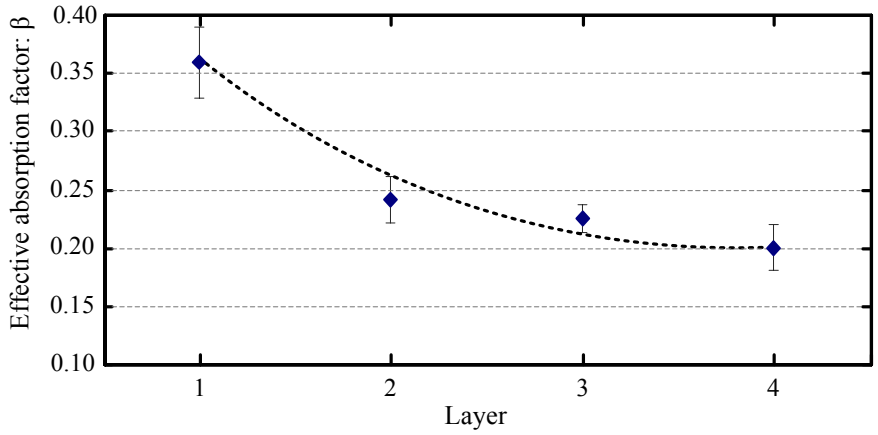

Figure 3.11 Effective absorption factor for each layer of a four-layer wall

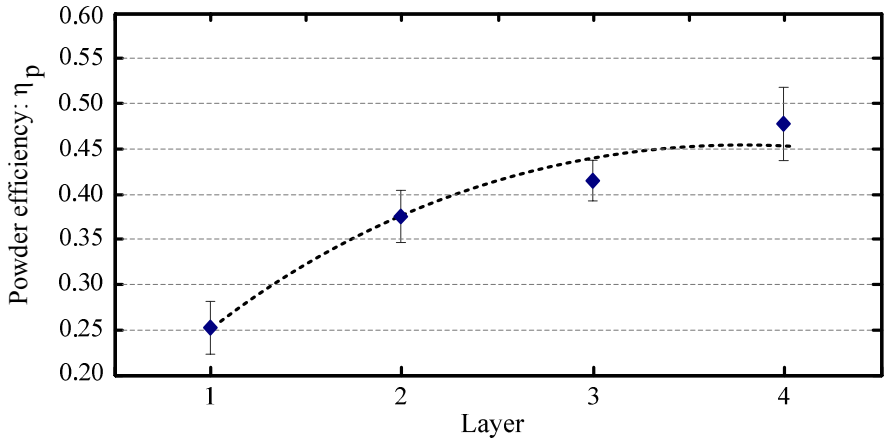

Figure 3.12 Powder catchment efficiency for each layer of a four-layer wall

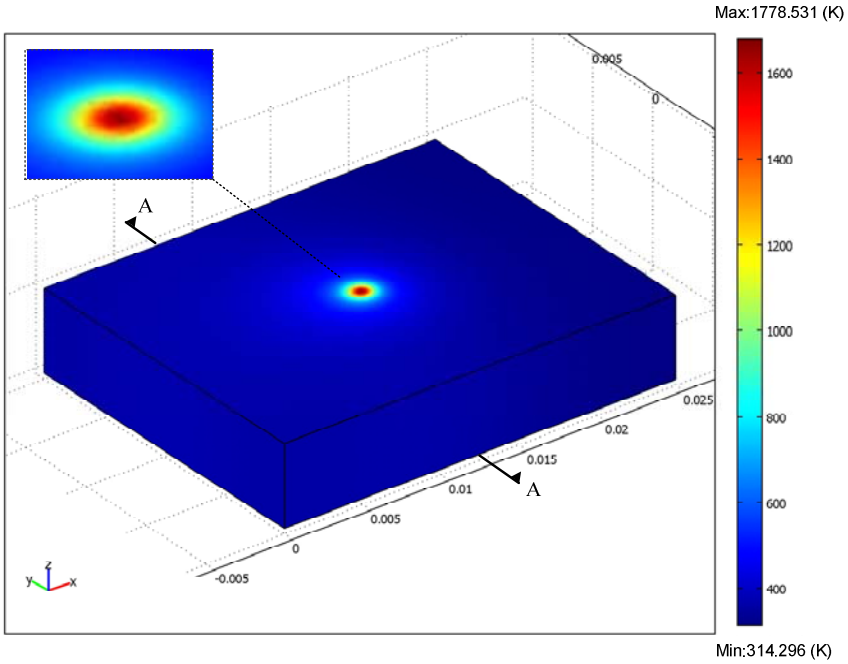

(a)

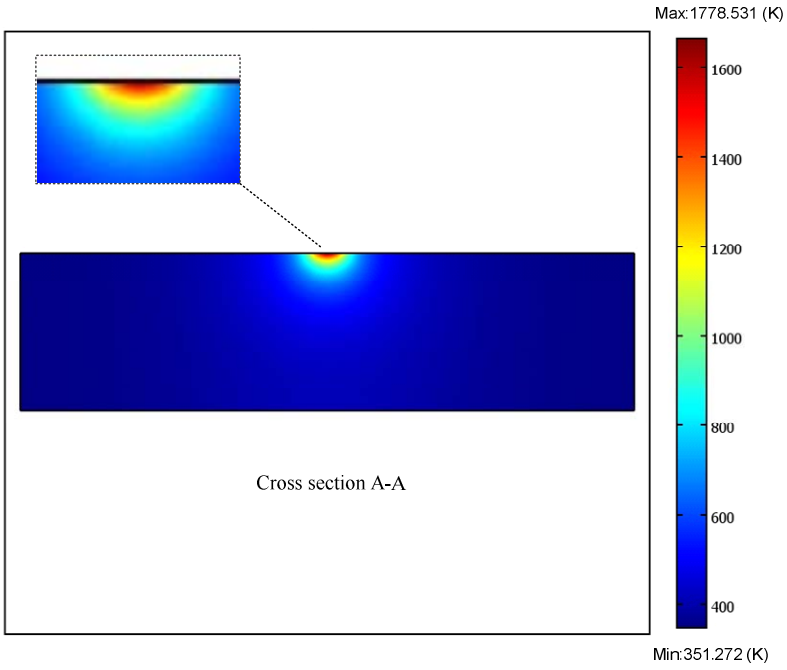

(b)

Figure 3.13 Temperature distribution at t =5 s for the first layer deposition throughout: a) the process domain, b) a cross section of the process domain perpendicular to the x axis

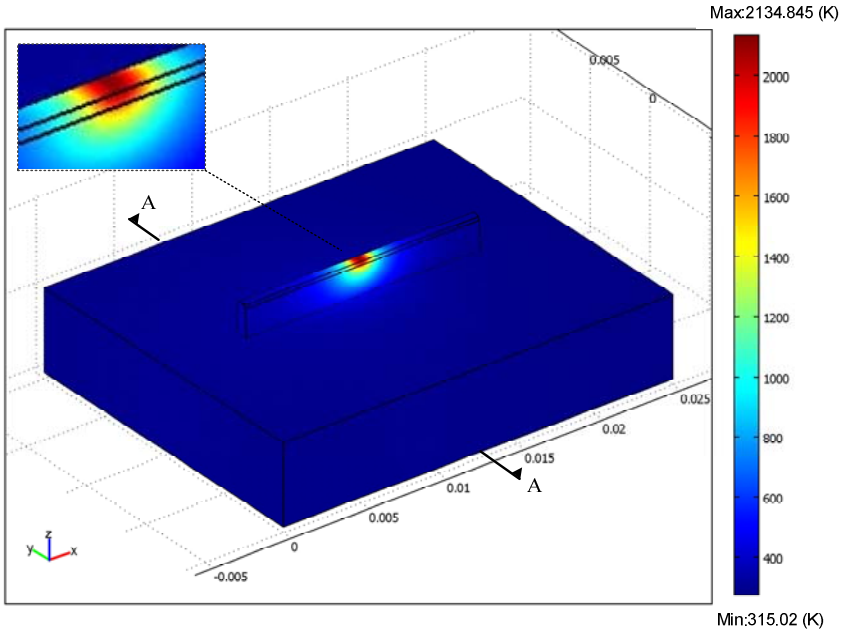

(a)

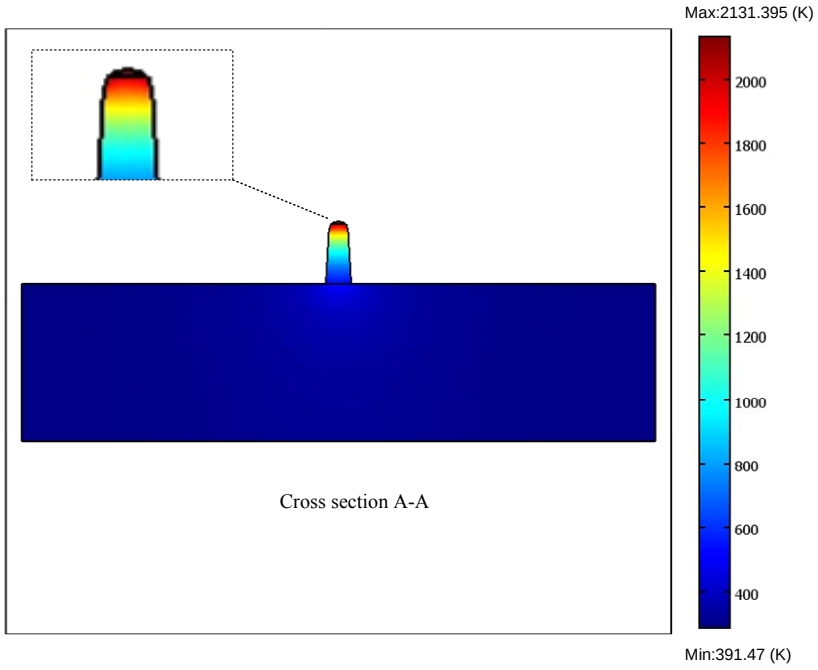

(b)

Figure 3.14 Temperature distribution at t =6.5 s for the fourth layer deposition throughout: a) the process domain, b) a cross section of the process domain perpendicular to the x axis

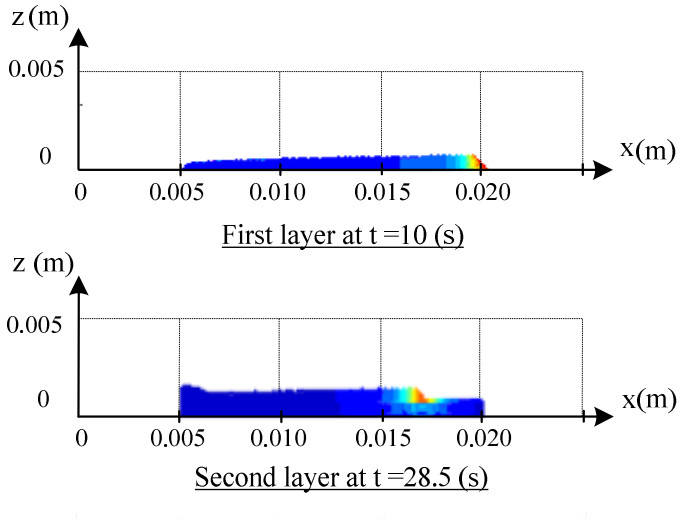

(a)

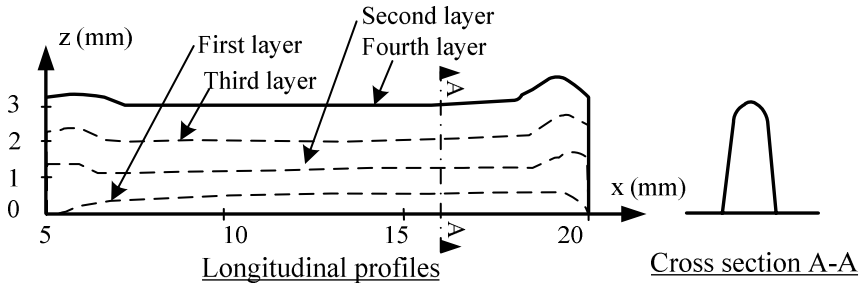

(b)

Figure 3.15 Simulation results of material deposition throughout the fabrication of a thin wall with four layers: a) Longitudinal views of geometrical predictions of the additive material deposited for the first and second layer, b) Longitudinal profiles and cross section of the deposited four layers

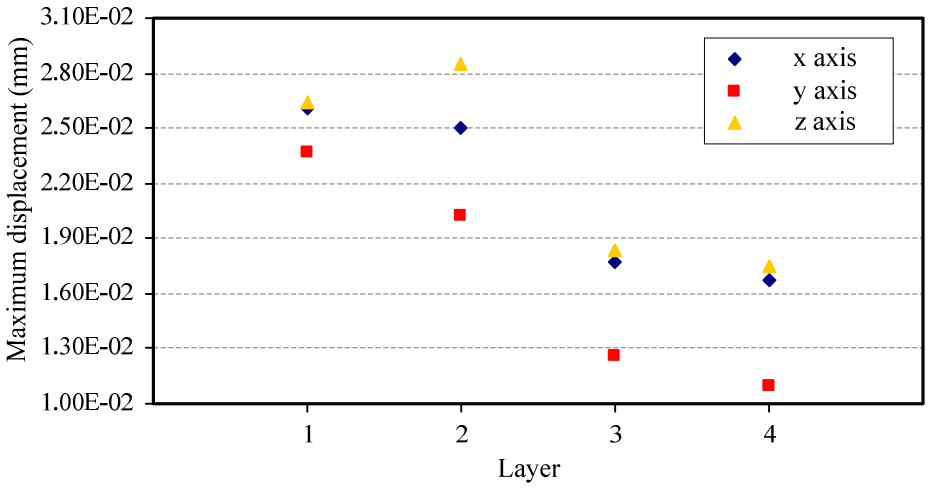

Figure 3.16 Maximum displacement of the substrate at the surface x=2.5 mm along with x, y and z coordinates

3.9.1 Experimental Setup and Procedure

To verify the numerical results, the same thin wall was experimentally fabricated with the same operating parameters and conditions described in the numerical simulations.

The experimental setup, as schematically shown in Figure 2.1, consisted of:

- A four-axis CNC table
- A LASAG FLS 1042N Nd:YAG pulsed laser with a maximum power of 1000 W
- A 9MP-CL Sulzer Metco powder feeder

For temperature measurements around the melt pool, two XCIB high temperature inconel overbraided ceramic fiber insulated type K thermocouples with maximum temperature of 1250 ˚C were used. These thermocouples were installed in the substrate adjacent to the laser pass and the data were recorded during the process using Lab VIEW (http://www.ni.com/labview/) as the data acquisition system interfaced with the motion system of the CNC table.

The laser beam intensity distribution was circular Gaussian TEM_{00}. The spot point of the laser beam was 5.08 mm under the focal point, and with a diameter of 1.4 mm on the

surface of the substrate. Argon gas with a flow rate of 2.3 e-5 m^3/s was used to shroud the laser beam, and as a shield to protect the optical lenses. The same argon gas was also used as a conveying gas to carry powder from the powder feeder system to the deposition zone. The powder feed rate was adjusted to 2 g/min and remained within ±5% of this value throughout the experiment. The angle of the lateral nozzle was set to 55 ° with respect to horizontal. The powder, SS304L, used in the experiment was 98 per cent pure on a metal basis. All other operating parameters are the same as those used in the numerical simulations. The process parameters are listed in Table 3.1. Figure 3.17 also shows the work station including the laser processing head, the lateral nozzle, and the thermocouple.

For this research, more experiments were performed to either verify or interpret the numerical results. The specifications of these experimental analyses and their related results will be presented and discussed along with their corresponding numerical investigations in the following chapters.

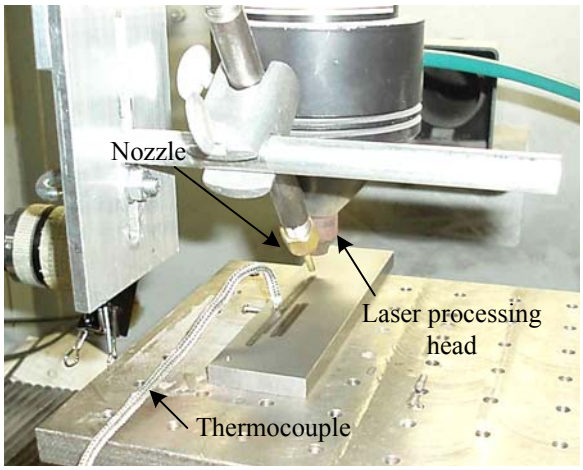

Figure 3.17 Work station

3.9.2 Comparison Between Experimental and Simulation Results

Using the setup described in the preceding section, a wall with four layers was deposited on the substrate. The fabricated wall is shown in Figure 3.18. A geometrical comparison between the simulation and experimental results after each layer deposition is also

illustrated in Figure 3.19 (in order to eliminate noisy data resulting from the mesh density and shape in the melt pool boundary, a moving average technique is used to smooth the data). A comparison between the average heights of each layer obtained from experimental and numerical results shows that the algorithm developed for material deposition can predict the geometry of the deposited material throughout the LSFF process with good agreement (maximum average relative error is 9.30 per cent). The error between numerical and experimental results throughout the build-up process is due to the assumptions made to formulate the LSFF process and the errors involved in the nature of numerical methods and their accumulation throughout the simulation process. Other potential sources of error can be related to the experimental setup, such as the variability of the powder feed rate throughout the experimental analysis.

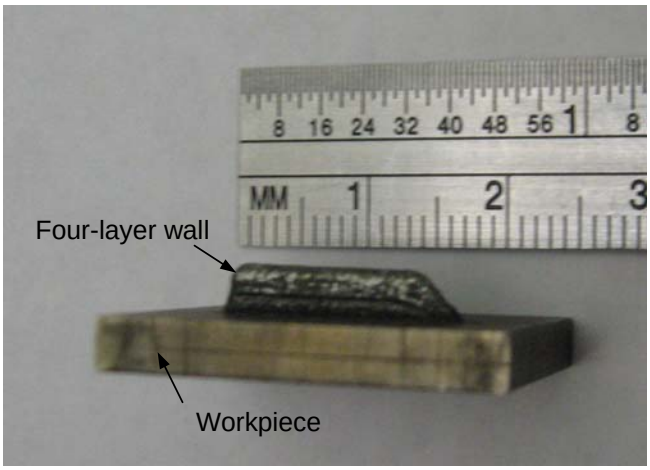

Figure 3.18 A thin wall with four layers fabricated by the LSFF process

In order to verify the accuracy of the FE analysis in terms of the thermal modelling of the LSFF process, the temperatures at two points in the substrate were measured continuously with the high temperature thermocouples described in Section 3.9.1 throughout the fabrication process. The positions of these two points in the substrate according to the coordinate system shown in Figure 3.10 are (17, 3, -1.5) and (12, 3, -1.5) mm for points A and B, respectively. The experimental results, the temperature histories at Points A and B, were compared with their corresponding results obtained from the simulation as shown in

Figure 3.20 and Figure 3.21 for these two points, respectively (Note that the laser was off for 10 seconds after each layer deposition in order to allow the positioning system to return the laser processing head to its home position, the fabrication time plan is shown in Figure 3.10 for the whole process). The data acquisition rate was set to 140 (Hz) in the algorithm developed in Lab VIEW.

The results demonstrate that the temperature profiles obtained from the developed numerical model correspond well to their counterparts measured experimentally. The average relative errors for the first to the fourth layer are 1.47, 3.8, 4.49 and 5.51 per cent for point A, and 1.55, 3.52, 4.42 and 5.29 per cent for point B, respectively. In Figure 3.20 and Figure 3.21, the position of the laser beam can be found considering the position of the laser beam along the x axis and its corresponding simulation time. For instance as shown in Figure 3.20, for Point A in the first layer deposition at the simulation time $t = 5$ s, the laser beam is at point P which is located at x =12.5 mm on the substrate, or $x = 7.5$ mm on the deposition track.

The model was also experimentally verified in terms of the distortion of the substrate caused by temperature distributions over the time (temperature gradient). For this purpose, two images were taken of the substrate before and after deposition of four layers using an optical microscope. In order to measure the deflection properly, several grooves were made on the substrate in the x, y, and z directions to measure the deflection of point d in the z direction as shown schematically in Figure 3.22. Displacement of point d' with respect to point d in the z direction was then determined based on these two images. The maximum absolute error is 3.80 per cent between experimental and numerical results. Maximum displacement of the substrate along with x, y and z coordinates are also shown in Figure 3.16. As seen, the maximum displacement takes place in the z direction which is a measure of the part deflection.

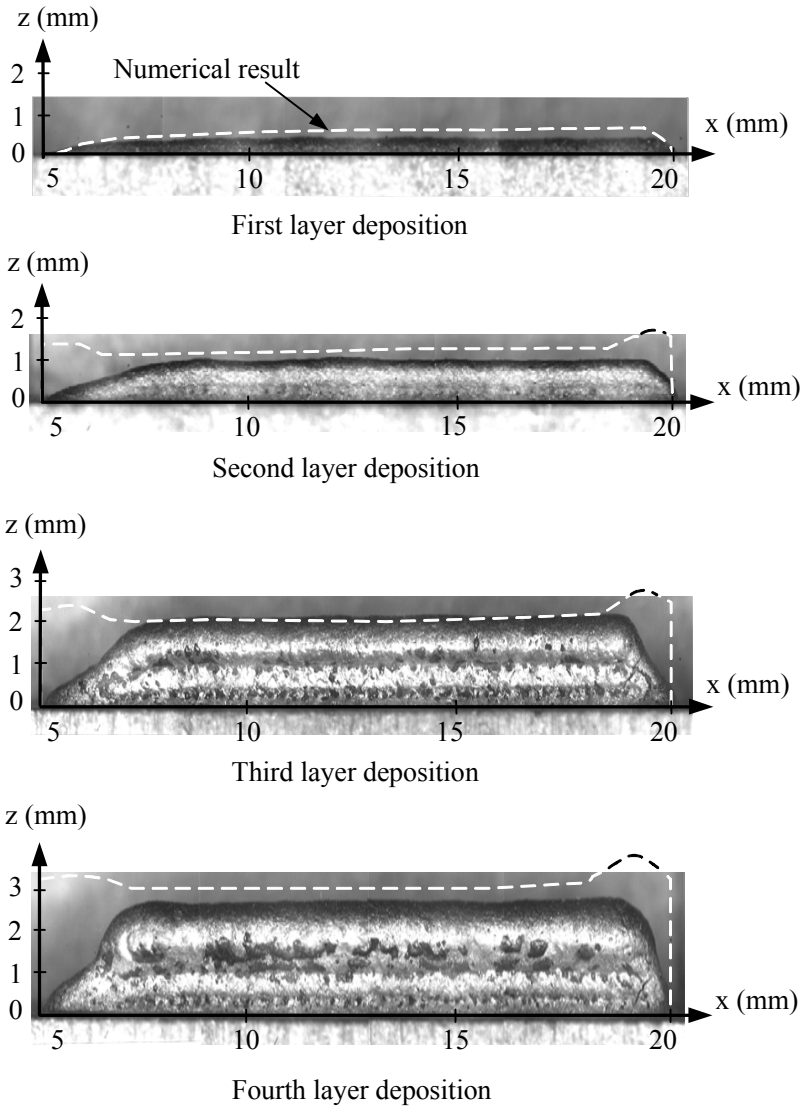

Figure 3.19 Geometrical comparison between experimental and simulation results

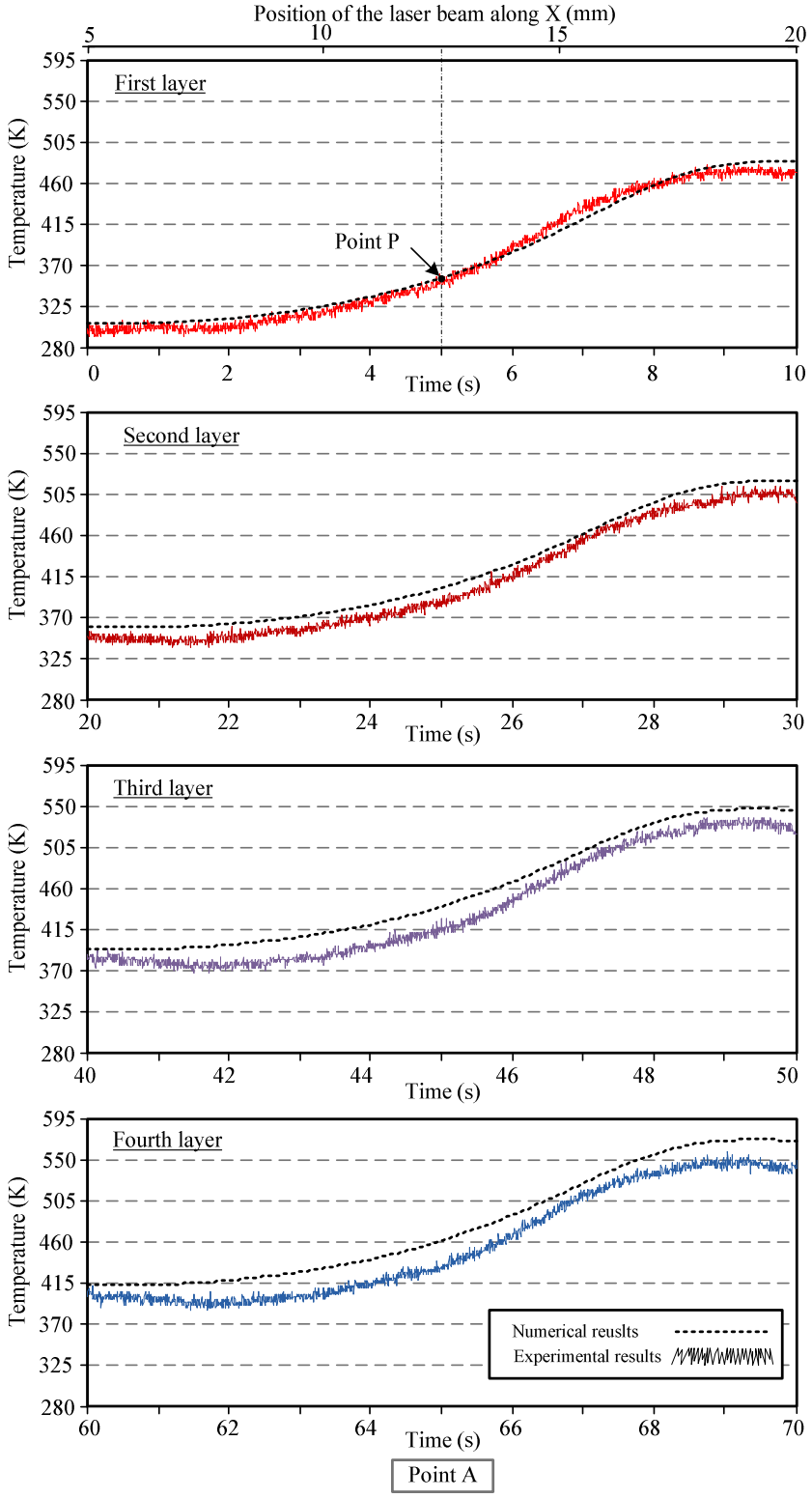

Figure 3.20 Experimental temperature measurement and their corresponding numerical values at point A

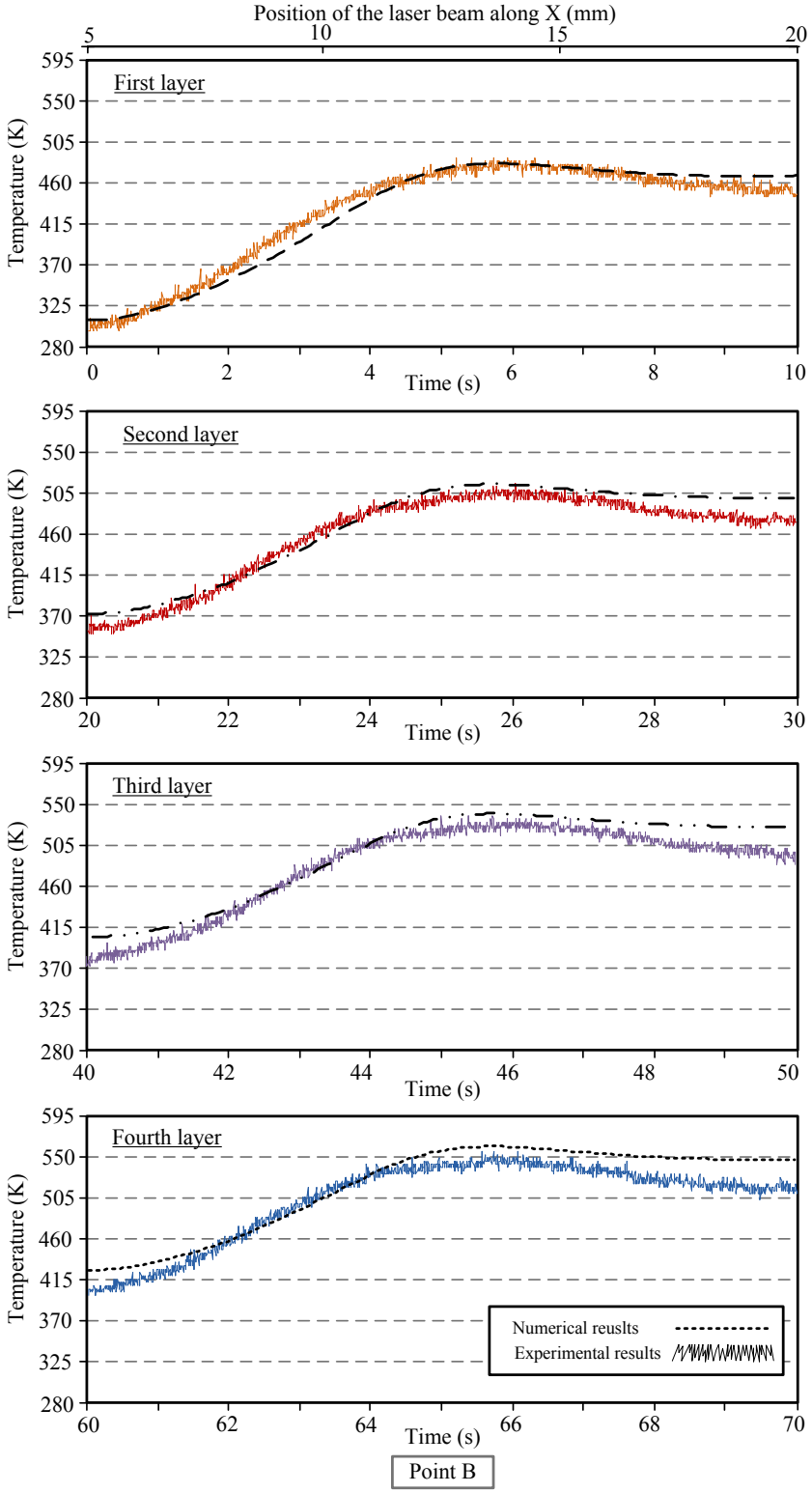

Figure 3.21 Experimental temperature measurement and their corresponding numerical values at point B

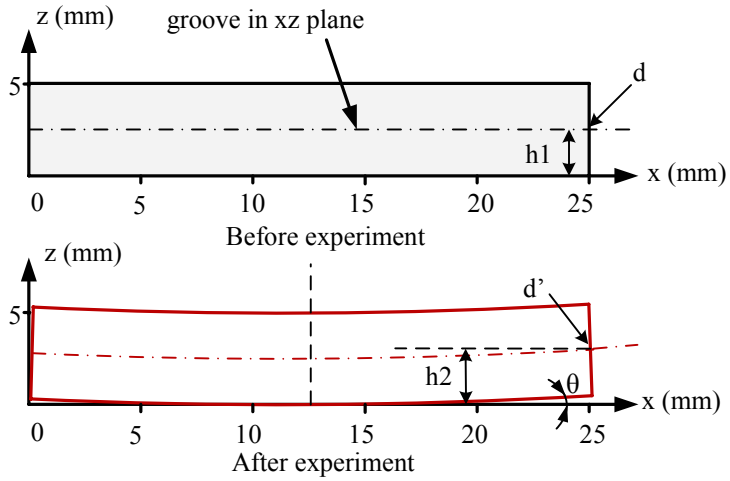

Figure 3.22 Substrate before and after experiment

3.10 Summary

Many research groups have developed different analytical and numerical models to study different aspects of the LSFF process. Several stationary and transient analytical and numerical thermal models have been developed in which various physical parameters related to the heat transfer phenomenon such as melt pool characteristics and geometry, interaction between melt pool and powder stream, thermal distribution throughout the process domain, and the effect of variations in the process parameters on the whole process were studied. Among these studies, only a few have reported on 2D and 3D modelling of the multilayer LSFF process. A number of research groups have also conducted studies to integrate stress fields induced by thermal gradients into modelling approaches as a major phenomenon which determine several mechanical – metallurgical qualities of the final part. However, in these reported modelling approaches, in addition to some simplifications and assumptions, the geometry of the deposited materials are defined in advance (i.e., a thin wall with a rectangular cross section), or in a dynamic fashion, a new group of elements at each time step is activated to build up a thin wall with a rectangular cross section.

In this chapter, a 3D numerical modelling approach was introduced by which the geometry of the layer-by-layer deposited material as well as coupled temperature and thermal stress fields across the process domain can be predicted in a dynamic fashion. In the

proposed modelling approach, the main process parameters as well as the effect of material deposition on non-planar surfaces were taken into account. FE method was used to solve the mathematical model developed based on the governing equations and their associated boundary conditions presented in Chapter 2 along with appropriate assumption and adjustment. To incorporate the additive material into the process domain, a decoupled method was proposed by which the additive material can dynamically be deposited into the process domain. Once the melt pool boundary is obtained from the FE solution, the physical domain is discretized in a cross-sectional direction. Based on the powder feed rate, elapsed time, and intersection of the melt pool and powder stream area on the substrate. Layers of additive material are then added onto the non-planar domain.

The developed model was used to simulate a four-layer thin wall of steel deposited on a substrate with dimension of 25×20×5 mm. The results show that the temperature and the thickness of the deposited layers increase at the end-point of layers 2, 3, and 4. Also, the powder catchment efficiency for the first layer is significantly lower than those of successive layers. The numerical results in terms of the geometry of wall, temperature distribution and stress field were experimentally verified with the same process parameters used in the numerical simulations.

Chapter 4

Temperature Distribution and Thermal Stress Fields Induced in the LSFF Process

Understanding the temperature distribution history is an important factor for process and path planning in LSFF. The presence of large temperature gradients throughout the fabrication process is the main cause of part deformation and consequent development of thermal stresses throughout the process domain. In layered manufacturing techniques including LSFF, the fabrication process consists of the deposition of sequential layers. Therefore, parts manufactured using LSFF are susceptible to delamination and crack formation. This chapter addresses the computation of the temperature distribution in LSFF and the effects on the geometry of the fabricated components, and stress fields induced throughout the fabrication process. A detailed discussion regarding melt pool characteristics, thermal stresses, and geometrical features of the four-layer thin wall is presented in this chapter after an introduction of the heat management in LSFF. The correlation between temperature distribution and microstructure of the fabricated parts fabricated is briefly reviewed. The effects of the path patterns on the thermal stress field and geometry of a fabricated part are also briefly addressed. In the last section, the effect of preheating the

substrate prior to the LSFF process in order to manage the thermal stresses, will also be discussed in detail.

4.1 Heat Management in the LSFF Process

The thermal behavior of the melt pool determines the output of the LSFF process. All geometrical aspects, metallurgical and mechanical properties of a part manufactured by LSFF, as have been discussed in the preceding chapters, are either directly derived or influenced by the melt pool characteristics. The nature of the temperature distribution (temperature gradient) over time is the main cause of distortion and thermal stresses in the part. The cooling rate at the liquid-solid interface of the melt pool affects the solidification process, and ultimately the material properties of the fabricated parts [21, 55].

To achieve a uniform clad bead, a melt pool with consistent features (i.e., with the same thermal and geometrical characteristics), relative to the process specifications, is essential. In order to have such a melt pool, all associated process parameters should be controlled throughout the fabrication process. In this regard, most process parameters related to the equipment can be monitored and ultimately controlled, if necessary. For instance, by changing the traverse speed or laser power, it is possible to change the size of the melt pool. However, the complexity arises from the fact that the geometry of the part changes within the LSFF process as a function of time. Namely, the melt pool features change as the build-up process proceeds. Therefore, to develop a robust control plan in order to obtain a uniform clad, the geometrical specification (i.e., topology and topography of an object over the time) of the location of the melt pool and its effect on the process should be integrated into the process governing equations. This can prevent unpredicted disturbances resulting from geometrical changes of the build-up into the LSFF process.

To have a melt pool with consistent features, the most important factor is to keep the heat conduction, convection, and radiation in balance with respect to the geometry of the location that the melt pool is formed. To further discuss this, it is possible to nondimensionalize the governing equations and associated boundary condition (Equations (2.5) and (2.11) to (2.14)). In order to show the concept, and without loss of generality, the terms of the heat loss by radiation will not be considered (Equations (2.13) and (2.14), the

heat loss through radiation can be considered in a combined radiative and convective heat transfer coefficient as presented in Equation (3.17)). The laser beam power is also considered constant for a specific time step.

The following definitions for dimensionless variables are selected [33]:

$$x^* = \frac{x}{L}; \quad y^* = \frac{y}{L}; \quad z^* = \frac{z}{L}; \quad n^* = \frac{n}{L} \tag{4.1a}$$

$$t^* = \frac{\alpha t}{L^2} \tag{4.1b}$$

$$\theta = \frac{T - T_\infty}{T_0 - T_\infty} \tag{4.1c}$$

$$\alpha = \frac{k}{\rho c_p} \tag{4.1d}$$

where T_∞ (K) is the ambient temperature, T_0 (K) is a uniform initial temperature and L (m) is a characteristic dimension of the body. By substituting the above variables with their corresponding variables, the following dimensionless Equations based on Equations (2.5) and (2.11) to (2.14) are derived, respectively:

$$\frac{\partial^2 \theta}{\partial x^{*2}} + \frac{\partial^2 \theta}{\partial y^{*2}} + \frac{\partial^2 \theta}{\partial z^{*2}} = \frac{\partial \theta}{\partial t} \tag{4.2}$$

$$\frac{\partial^2 \theta}{\partial n^*}|_\Omega = \frac{L}{k(T_0 - T_\infty)} \beta I(x^* - \frac{L^2}{\alpha}(\int_0^{t^*} u_x dt^*, y - \int_0^{t^*} u_y dt^*, z - \int_0^{t^*} u_z dt^*), \frac{L^2}{\alpha} t^*) - Bi\,\theta_b \tag{4.3}$$

$$\theta_0 = 1 \quad \text{when} \quad t = 0 \quad \text{and} \quad t = \infty \tag{4.4}$$

where Bi is the Biot number defined as:

$$Bi = \frac{h L}{k} \tag{4.5}$$

The governing equation and the second boundary condition in the new format do not contain any parameters, and only the Biot number as a single parameters appears in the convection boundary condition, Equation (4.3). The above dimensionless equations show that the solutions of systems with the same geometry only depend on dimensionless time and the *Biot* number [33]. One of the inherent characteristics of the Biot number can be derived through its alternative definition. For this purpose, the Biot number definition is rearranged as [33]:

$$Bi = \frac{hL}{K} = \frac{T_b - T_c}{T_b - T_\infty} = \frac{(L/KA)}{(1/hA)} = \frac{R_{cond}}{R_{conv}} \tag{4.6}$$

where T_b, T_c and T_∞ are shown in Figure 4.1.

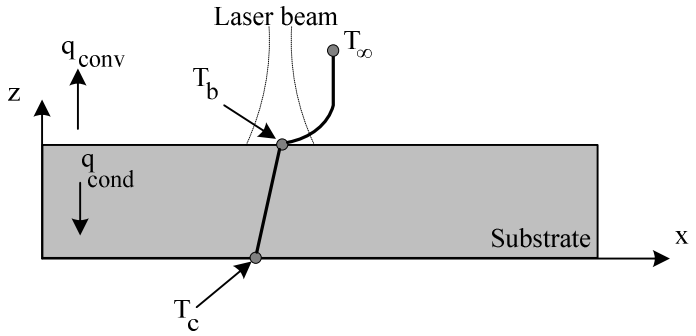

Figure 4.1 Temperature indications on the substrate

Equation (4.6) implies that the Biot number shows the rate of heat conduction to the rate of heat convection in a thermal system. For example, a small Biot number indicates that the heat transfer by conduction dominates the heat transfer by convection, and in this case a system with a sudden change in its temperature can return to its steady state more quickly than a system with a larger Biot number. Therefore, in the LSFF process, the small Biot number provides a better cooling rate regime, and consequently reduces the maximum temperatures formed in the melt pool (the temperature gradients through the part). Figure 4.2 shows the transient temperature distributions across a thin substrate for different cases of Biot numbers while the substrate is being cooled by free convection [33].

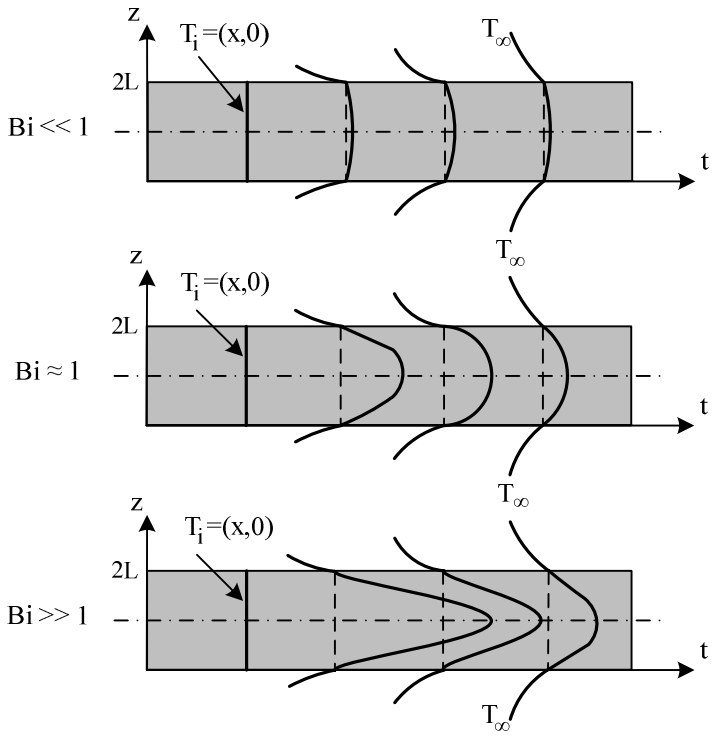

Figure 4.2 Transient thermal distribution in a thin substrate for different Biot numbers while being cooled by free convection

Several research programs have studied the temperature distribution in different fields of laser material processing, either the effects of the temperature distribution on the outcome of the process or the effects of the process parameters on the temperature distribution. Among these investigations, Kalyon et al. [64] studied the effects of the pulse parameters and specifically the effect of the Biot number on temporal variation in surface temperature of the substrate. They studied the physical phenomena involved in the laser heating process through a closed-from solution for the temperature rise in the substrate. The governing equations were solved using a Laplace transformation method. Pinkerton et al. [65] studied the effects of changes in the distance between the laser deposition head on the melt pool size, temperature distribution, and powder flux using a coaxial powder feeding system. For this study a 3D analytical model was developed. The model was combined with another model for powder flow to investigate material assimilation rates. Based on the experimental results, it was shown that with decreasing distance between the melt pool and deposition

head, higher walls were built, compared to cases where the deposition head was kept unchanged relative to the melt pool positions. Jandric et al. [66] have also proposed a dimensionless geometrical factor as a connection between process parameters and the substrate geometry in order to perform heat management for solid freeform fabrication based on gas-tungsten arc welding deposition in a real time fashion. The geometrical factor had its maximum value of 1 when an observed point is far from the boundaries of the part, and has its minimum 0 on the boundaries. Therefore, in their work the dimensionless geometrical factor represents the actual amount of material around the observed point (i.e., HAZ and its close surrounding). They reported that their real-time adaptive controller which was developed based on their proposed heat management method showed robust performance in terms of uniform material deposition through the fabrication process.

To describe the effects of the temperature distributions throughout the process on the geometry of the deposited material and thermal stress fields induced in the LSFF process, a detailed discussion of the numerical and experimental results of the four-layer thin wall (for which the numerical and experimental fabrications were described in the last chapter) is presented in the next section.

4.2 Melt Pool Condition and its Effects on Geometrical Characteristics and Thermal Stresses in LSFF

As seen in Figure 3.15b and Figure 3.19, the clad height increases at two end-points of layers 2, 3 and 4. This is because of higher melt pool temperatures at these two regions which result in a bigger melt pool, and consequently, higher powder catchment. Maximum temperatures along with the deposition tracks throughout the fabrication process are showed in Figure 4.3.

Considering the heat source dimension, the substrate acts as a heat sink in terms of absorbing the energy conveyed from the laser beam throughout the build-up process by conduction, and transfers a portion of this energy to the surroundings by convection and radiation, as considered in Equations (3.25) and (3.26). Therefore, considering the geometrical changes from the first layer to the fourth layer, the nature of heat transfer for

the first layer is different from subsequent layers. For the upper layers, the nature of the heat transfer is similar to a thin vertical fin, whereas for the first layer, the physical domain is compatible with a semi-infinite heat conduction domain. Considering the geometry of a thin wall, the heat losses through convection and radiation increase as more layers are deposited. This effect can also be observed between the middle and the end segments of the wall. Figure 4.4 shows the difference between the nature of the heat transfer of the thin wall and the substrate. Since the energy losses through convection and radiation are relatively lower than that by conduction, with the proposed combined convection factor (approximately in the range 8 to 186 (W/ m^2.K) calculated using Equation (3.17)), the temperature rises at the ends of each layer and also at upper layers (This can also be justified based on the Biot number described in the last section and presented schematically through Figure 4.2). This effect in the experimental results is not as evident as in the numerical results. The reason is that the flow of molten material and adherent/coherent effects are not fully considered as a function of the height for the multilayer deposition in the modelling strategy.

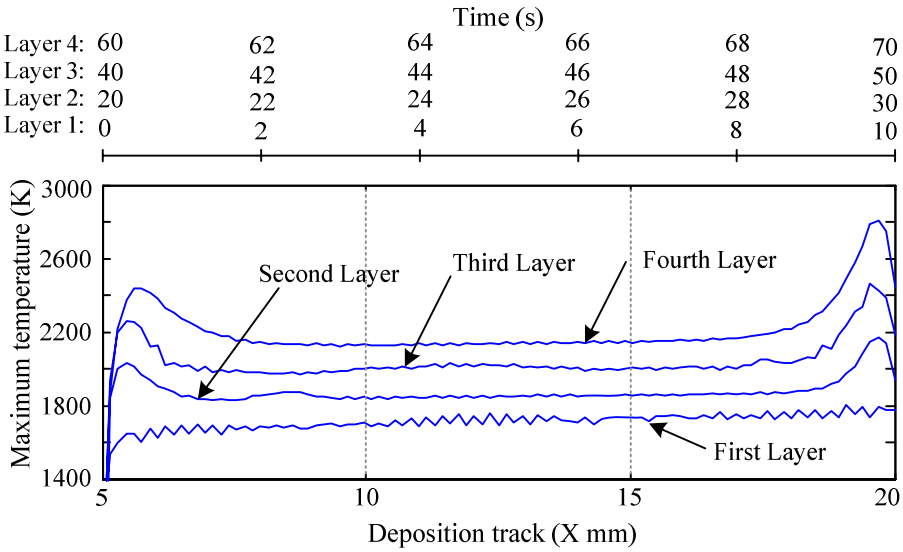

Figure 4.3 Maximum temperatures along with the deposition tracks

However, a comparison between the wall cross sections obtained numerically and experimentally shows that in the wall fabricated experimentally, more material is deposited in the upper layers. This fact is evident from the increase of wall thickness throughout the buildup process, as shown in Figure 4.5. In this figure, the cross section A is at $x = 8$ mm (relative to the coordinate system shown in Figure 3.10) with a maximum thickness of 1.495 mm, and the cross section B is at $x = 12.5$ mm with a maximum thickness of 1.365 mm. Moreover, as seen in Figure 3.19, the startup transients in the laser beam and the power stream at the starting points make the wall built experimentally with a stair step shape at this point (the stair step shape will be addressed in detail in the next sections). However, the shapes of the end-points of the wall are closer to their numerical counterparts as the result of the more stable operating parameters.

The geometry of the first layer shows the same trends observed from the experimental and numerical results. As explained, the substrate acts like a heat sink throughout the fabrication process, the lower melt pool temperature results in a smaller melt pool boundary and consequently a lower powder catchment. This produces a smaller track compared to the subsequent layers as illustrated in Figure 3.19. Therefore, the wall at the base is thinner as shown in Figure 4.5. The same trend was reported through the experimental analyses of thin walls with ten layers where a geometrical variation coefficient is defined to check the geometrical differences caused by changing the laser power [11].

The temperature distribution under a predefined set of process parameters varies with the geometrical formation of a part throughout the fabrication process. With the same process environment, the results in terms of thermal stresses show that the changes in the thermal stresses are a function of the time-dependent geometry of the process domain and the temperature. This is also implied by the related governing equations, Equation (3.22). Corresponding to the temperature distribution and transformation throughout the LSFF process presented in Figure 3.13 and Figure 4.3, their counterparts for the thermal stress can also be extracted from the numerical results. For instance, Figure 4.6 shows the maximum thermal stresses (Von Mises) of the first layer imposed by the deposition of the second to fourth layers.

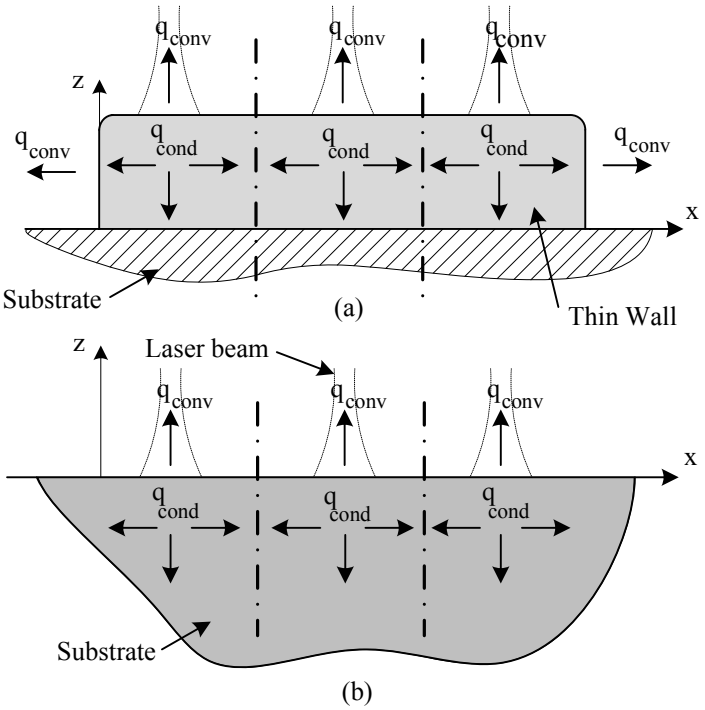

Figure 4.4 Heat transfer nature on: a) the four-layer thin wall, and b) the substrate during the LSFF process

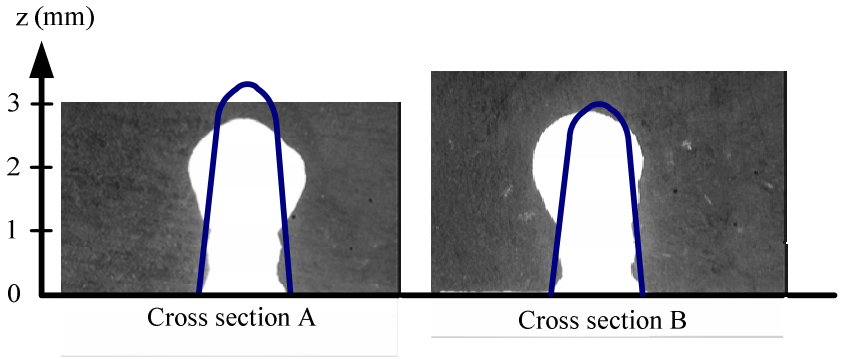

Figure 4.5 Cross sections A and B of the thin wall at x = 8 mm and x = 12.5 mm

Figure 4.6 shows that the maximum stresses increase at the two ends of each layer after the first layer deposition, while for the middle segments, these stresses decrease as the number of deposited layers increases. In contrast to the maximum temperatures that evolved within the deposition process (as illustrated in Figure 4.3), the average maximum thermal stresses formed through the first to the fourth layer deposition (based on the Equation (3.22)) exhibits a different behavior and decreases. This is due to the geometrical changes and the decrease in thermal gradients throughout the process (the substrate temperature within the build-up process increases). The average maximum thermal stresses of the second, third and fourth layers compared to the first layer were 20, 22.5 and 24 per cent reductions, respectively. On the other hand, because of the sudden geometrical changes, although the average thermal stresses decrease during the LSFF process, the maximum stresses still occur at the end segments of layers 2 to 4.

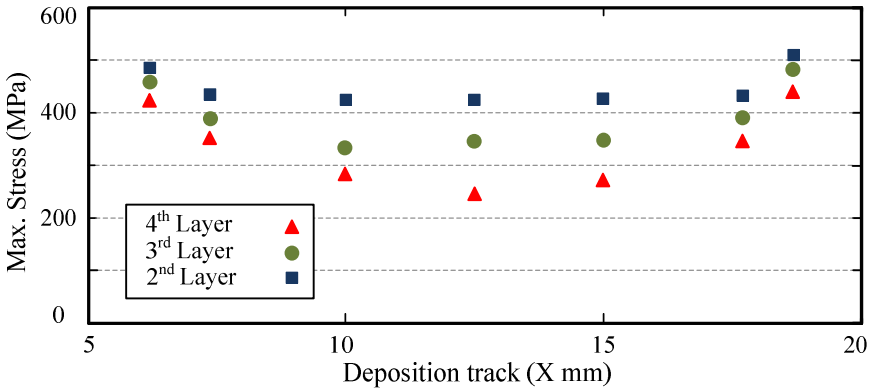

Figure 4.6 Maximum thermal stresses (Von Mises) of the first layer imposed by the deposition of the second to fourth layers

Figure 4.7 also shows the maximum stresses over the maximum temperatures for each layer along the deposition track (noisy data resulting from the mesh density in the melt pool boundary are eliminated using a moving average technique to smooth the data). This parameter (i.e., ψ = maximum stress/maximum temperature) is a function of process parameters, material properties, and geometries of the deposition points. ψ (Pa/K), which

should be lower than a specific value, can be represented by the following mathematical expression:

$$\psi = \frac{\sigma_{\max}}{T_{\max}} = f(U, P, r_l, ...; \rho, T_m, ...; D_{clad}) \leq \mu_m \; or \; \mu \tag{4.7}$$

$$\mu_m \text{ if } \psi \in \text{melt pool} \quad \& \quad \mu \quad if \quad \psi \notin \text{melt pool}$$

where D_{clad} is geometrical specification of the clad formed dynamically during the LSFF process. μ_m (Pa/K) can be determined base on the vaporization temperatures of the substrate and additive materials, and mechanical specifications of the melt pool. μ (Pa/K) can be calculated based on the maximum temperature and yield stress. As seen in Figure 4.7, ψ increases at both end segments of the wall indicating the possibilities of crack formation and delamination in these regions, similarly to what Figure 4.3 and Figure 4.6 imply. Finding critical values for ψ for different materials and process parameters requires more numerical and experimental analysis.

The results obtained from the model show that by controlling the thermal distribution and sudden geometrical changes, it is possible to manage the thermal strains and consequently thermal stresses, which is the main source of cracks and delamination of the layers deposited within a buildup process. To show this, the substrate of the sample model was clamped to the positioning table at its four corners (0,0,0), (25,0,0), (25,20,0), and (0,20,0) mm . In this case, while the temperature distribution throughout the process does not change for clamped and non-clamped models, as shown in Figure 4.8, the locations of the maximum stresses are different for these two models. The maximum stress concentration fields for the non-clamped and clamped substrates are shown in Figure 4.9a and b, respectively. For instance, the maximum thermal stresses for the clamped model at $t = 9$ s has 3.9 per cent reduction at the same region (region B1 shown in Figure 4.9b) compared to the non-clamped substrate (region A1 shown in Figure 4.9a). For the clamped substrate, more stress concentrations occur at the clamped regions.

In the next sections of this chapter, controlling the thermal distribution in other to reduce the thermal stresses will be discussed in more detail.

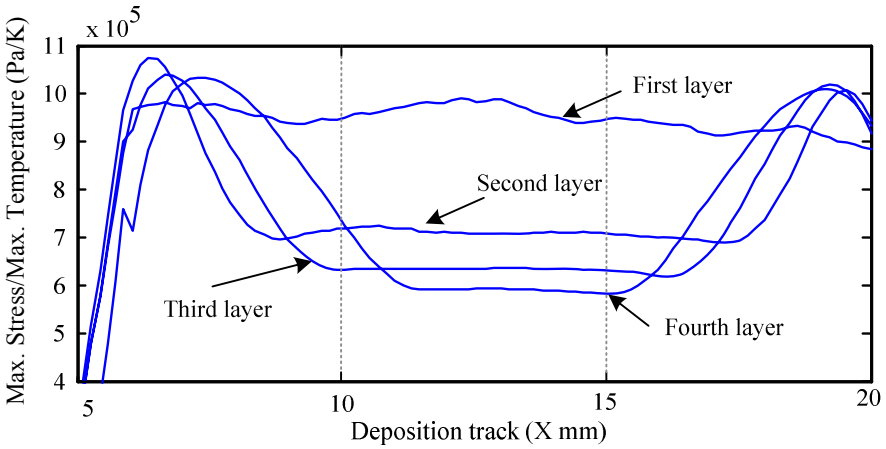

Figure 4.7 Maximum stress over Maximum Temperature for each deposited layer

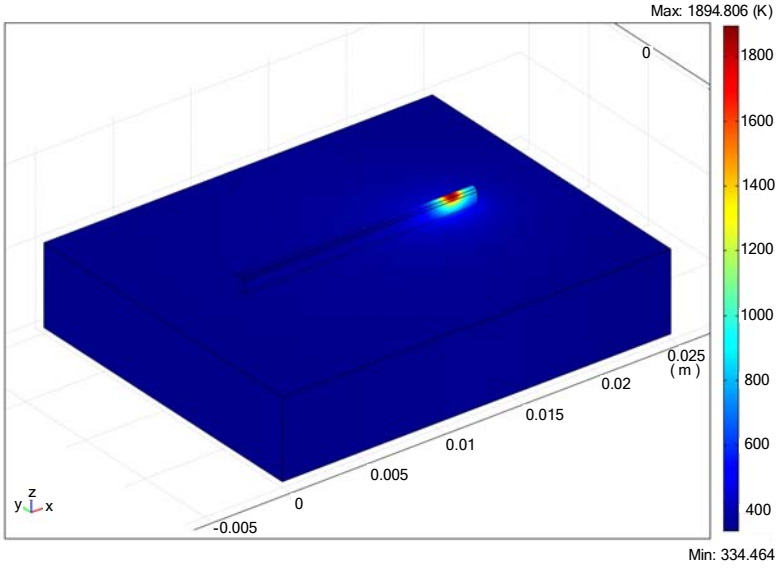

Figure 4.8 Temperature distribution for non-clamped and clamped substrates at t = 9 s

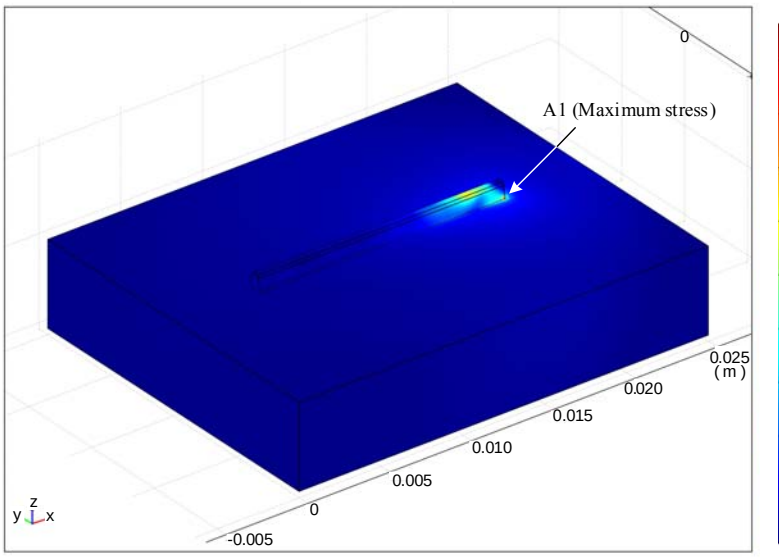

(a)

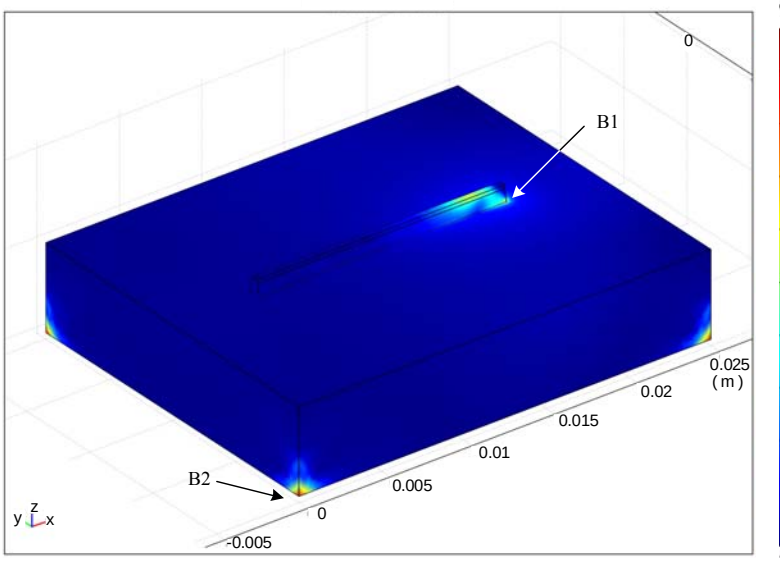

(b)

Figure 4.9 Thermal stress concentration: a) the non-clamped Substrate, b) the clamped substrate for the second layer deposition at t = 9 s

4.3 Temperature Distribution and Microstructure

Microstructure determines the final quality of a fabricated part. Rapid solidification can produce materials with superior mechanical and metallurgical properties. In LSFF, the small heat zone (laser beam area on the surface of the substrate) compared to the substrate size results in a very high heat loss as discussed in the preceding sections of this chapter. Therefore, due to the very high heating and cooling rates, fine microstructure/meta-stable phases are expected [70]. This characteristic of the LSFF process has widely been studied through laser surface treatment where a wear resistant surface is required. This application, because of the flexibility of this technique, has further been expanded for repairing wear on high value components [67, 68]. In this respect, many research programs have focused on the investigation of the final microstructure of a component built up using the LSFF technique. They studied the microstructures of different materials used for manufacturing a part using LSFF as well as the effects of the process parameters on the microstructure of fabricated components.

For instance, to fabricate high performance saw blades, WC-Co was deposited on a steel substrate using the LSFF technique. It was reported that after various mechanical and metallurgical analyses, the results demonstrated crack free WC-Co deposition with a superb bonding. The minimum average of the micro-hardness from 700 HV at the blade has improved to 1450 at the final surface [69]. Adak at el. [29] experimentally studied laser cladding by wire feeding Cu-30Ni, which is known for its corrosion resistant properties, to define the microstructure of the clad material and the HAZ in the substrate as a function of the process parameters. Their results showed that a high quality clad with excellent mechanical integrity can be obtained within a wide range of process parameters. Their findings are only for a single layer deposition and subject to variations of the laser power, traverse speed, wire feeding speed and beam angle in a specific range. Investigation of the effect of laser pulse width on the microstructure and surface finish in multilayer LSFF is another research in this field that conducted through the fabrication of a straight vertical wall of 316L steel [46]. Li et al. [70] studied the effect of carbon content of the microstructure and cracking susceptibility of Fe-based layers using a continuous wave CO_2 laser. Their results showed that with the increase of carbon content, the hardness of the

layers does not always increase, while with a small change of carbon content in the alloy powders, the microstructure of the deposited layers can be changed. D'Oliveira et al. [53] studied microstructural characteristics in multilayer deposition of Stellite 6 on a 304 stainless steel substrate (coating of one to five layers). The results of their investigation indicated that a non-uniform hardness is formed through the coating resulting from soft interface regions adjacent to harder regions. The hardness decreases at the overlapped regions due to the melting and reheating of these parts. This is more evident in the upper layers. It was reported that microstructures with dendritic and lamellar interdendritic were observed. Near to the external surfaces, the results showed an increased interdendritic refinement. The results obtained from this work were used to discuss the feasibility of the process for maintenance of worn surfaces. In another research program, Pinkerton et al. [46, 47] experimentally investigated the effects of laser pulse width and frequency on the microstructure of a thin wall of stainless steel. The results showed that the microstructures are fully austenitic using either pulsed or continuous lasers. The microstructure is mainly cellular. In the regions between the deposited layers directional growth was also observed. This is more apparent in the results obtained from pulsed layers. It was shown that the surface roughness changes slightly with pulse frequency, however, it is better with pulsed laser than with continuous. The surface roughness and track height increased in the vertical direction with an increase in pulse length, but this also resulted in a decrease in the macro-hardness of the part.

Another priority of research in this field is the exploration of different materials and alloys with novel properties that can be adopted for the LSFF fabrication process. This research is substantially focused on the cladability of alloys and materials intended to be used for fabrication processes, through investigation of their microstructures and physical properties. Cladability is considered "to include primarily the formation of a continuous, high density clad deposit with a uniform or homogeneous microstructure, possessing a strong metallurgical bond to the substrate but with low dilution. However, in particular cases, cladability could also include the requirement of a certain level of dilution by the substrate, a certain clad height or deposition efficiency or even specific material properties that are required from the clad" [71].

As pointed out, in LSFF, the microstructure and physical properties of the fabricated parts are determined by the solidification circumstances, defined through the local parameters, and transformations that take place during cooling in the solid-state stage. Therefore, the microstructures and properties of a component might vary throughout the fabricated structure. This variation depends on the process parameters and the thermal history of each point and possible phase transformations that occur during the fabrication process [52, 72]. Since the aforementioned information is difficult or sometimes impossible to obtain by means of experimental analyses, few articles have particularly extended the numerical results further to study the variations of the microstructure, or any of its related parameters, and its correlation with temperature distributions (temperature gradient at the solid/liquid interface and cooling rate). Jendrzejewski et al. [73] modeled the temperature field in the multi-layer LSFF process using a coaxial nozzle. In this approach, the geometry of the deposited materials was considered in advance. It was assumed that the traverse speed is low enough for the powder particles to remain in the melt pool long enough to be melted. The 2D numerical results were obtained using a nonlinear heat transfer variable step analysis method. They used the numerical results to measure the dilution based on the isothermal contour maps obtained from the numerical solutions. The cooling rates and their variations through multi-layer depositions of bronze and stellite were also studied. Costa el at. [52] investigated the effects of the substrate size and idle time between the deposition of subsequent layers on the microstructure and hardness of a thin wall with ten layers of AISI 420 steel. The specifications of their proposed model were briefly explained in 3.1. In this study, the thermal history of each point was also used to study any phase transformation that occurred in any solid-state phase throughout the fabrication process. The microstructure of a track in multi-layer deposition goes under first rapid solidification of the deposited material, then preheating or remelting at the interface through deposition of the subsequent layer, and finally cooling as the melt pool travels away by increasing the height of the build-up. After solidification, the formed microstructure is mainly made up of austenite dendrites. It also consists of a small portion of inter-dendritic carbide particles. The diffusive transformations of austenite are prevented completely because of the presence of the high cooling rates in the LSFF process. This phase will go through a martensitic transformation as the deposited track cools down to ambient temperature. Depending on the

process parameters, the top portion of each deposited track remelts and goes under another solidification process. This can result in martensite tempering or in austenitization for temperature higher than Ac_1. The transformation that occurs during the second cooling process is highly dependent on preheating circumstances. If there is not any austenite formed throughout the reheating process, consequently, there is not any major phase transformation during the cooling process. However, if the microstructure is transformed into austenite, austenite will partially or entirely transform into martensite during the second cooling process.

In the remainder of this section, the multi-physics modelling results, presented in Sections 3.9.2 and 4.2, are further extended to study the microstructure of the fabricated component using the LSFF process as well as correlation between the temperature distributions and the formed microstructures. It should be noted that the results are highly dependent on the process parameters and solidification conditions of this specific work.

Using the proposed numerical model, it is possible to obtain the time-dependent temperature and stress profiles of each point within the process domain throughout the build-up process. Figure 4.10 shows the temperature profiles of four points along the deposition track on the plane $y = 0$. Therefore, it is possible to calculate the cooling rate for any desired point across the process domain using the corresponding time-dependent temperature profiles, as shown in Figure 4.11 for three points before deposition of the third layer.

The experimental analysis was performed based on the procedure explained in Section 3.9.1. Using a diamond wheel, three transverse cross-sections were cut from the same samples at a distance of 7 mm, 12.5 mm and 18 mm from the starting edge, along the x axis based on the coordinate system shown in Figure 3.19. The samples were cleaned and polished to metallographical quality. The samples were electrolytically etched with 10% oxalic acid at 12 V DC for about 25 s to reveal the microstructure. The samples were then examined using optical and scanning electron microscopes.

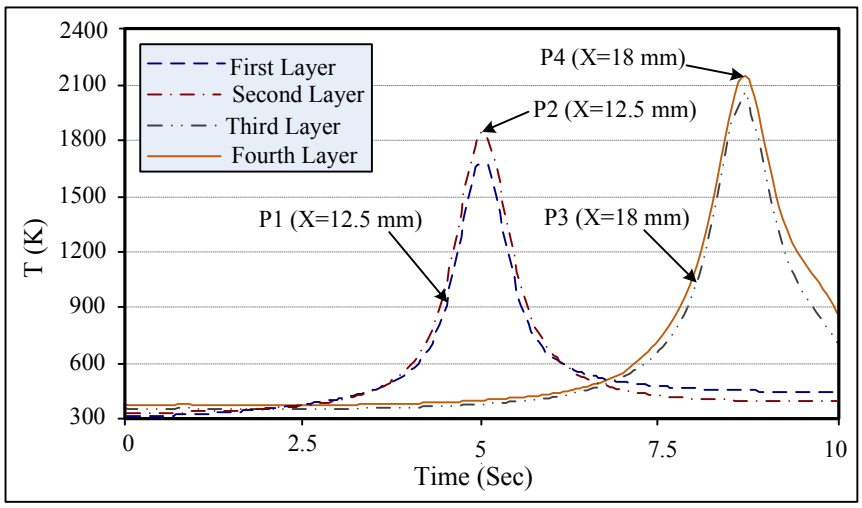

Figure 4.10 Temperature Profiles of the four points along the deposition tracks of the first to fourth layer depositions on the plane *y=0*

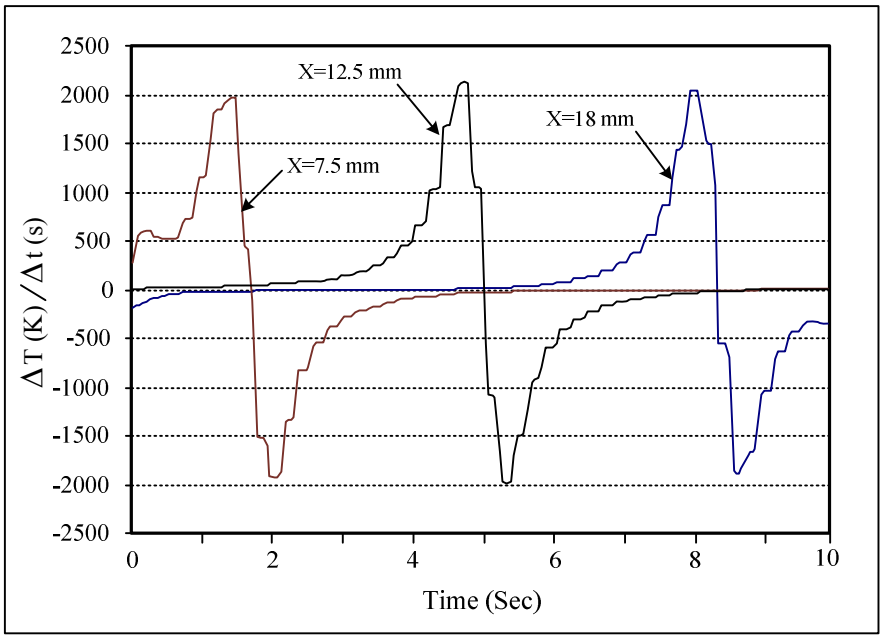

Figure 4.11 Cooling rates of the third layer for points on the center of the melt pool at x= 7.5, 12.5, and 18 mm

During a "single layer fabrication" using the LSFF process, the ratio of temperature gradient at the solid/liquid interface to solidification rate decreases from the bottom to the top in the melt pool. This results in different modes of solidification as per constitutional under-cooling criterion, and the resultant microstructure starts with a plane front solid/liquid interface, evolves rapidly to a dendritic without secondary arms (also called cellular [74]) and then to a dendritic with secondary arm interface. Vilar [75] showed that the final microstructure of a deposited track consists of narrow plane-front and dendritic without secondary arm solidification structures at the bottom of the melt pool, followed by a dendritic structure with arm spacing that occupies most of the track. In the fabrication of the four-layer thin wall as described in Chapter 3, a similar trend of microstructures was also observed during deposition of each single layer. However, in multilayer deposition, the observed microstructure in the top surface of the final deposited layer was predominantly equiaxed with fine dendrites, regardless of the number of previously deposited layers. This type of microstructure is shown in Figure 4.12a (this figure shows the top surface of the fourth layer). This type of microstructure is formed as a result of the higher "local cooling rate" in all directions (1.3e3 K/s obtained from the numerical model). It is interesting to note that this dendritic microstructure was changed to another as per constitutional undercooling criteria and epitaxy during the deposition of the subsequent layers in a multilayer deposition process.

During the "multilayer deposition" of the thin wall, the fine dendrites with secondary arms are observed at the first layer where the average cooling rate is relatively higher compared to that for the upper layers. This type of microstructure is then changed to a mixed dendritic microstructure with and without secondary arms and finally to dendrites without secondary arms as the cooling rate is further decreased. This is because dendrites without secondary arms can also be formed when the columnar growth in-solidification is approximately equal to the constitutional undercooling velocity. As the growth rate further increases, dendrites with secondary arms are formed. At still higher velocities, the front becomes dendritic without secondary arms again, and later banding may occur [76]. The fine dendritic microstructure with columnar orientation is detected at all locations near the substrate in the first layer. The coarsening of grains is also observed at the interface between

two successive layers. The grain coarsening is attributed to the heating effect of the subsequent layer deposition (the heat conducted from the solidified pool to the already deposited layer). It was also observed that micro cracks were initiated at the substrate and the first layer interface.

Figure 4.12b shows the dendritic microstructure without arm spacing at the third layer of the thin wall. This microstructure is present at all locations in the third and fourth layers and predominantly at the second layer. This is due to a relatively lower cooling rate at these locations (0.73e3 K/s) compared to the first layer. No micro-cracks and other bulk defects, except few at isolated locations, were detected in these layers. This is primarily the result of the lower thermal stresses and more ductile nature of the material in the dendritic microstructure without secondary arms.

The mixed microstructure of dendrite with and without secondary arms is shown in Figure 4.12c. This kind of microstructure is observed mainly at the bottom of the second layer, where the cooling rates are in the relatively intermediate regimes (0.86e3 K/s). This is the layer where the material properties are in the transition from brittle to ductile nature and with relatively lower cooling rate as compared to that near the substrate. Since the ductility of the material is increasing and thermal stresses are lower in-magnitude for this layer, most micro cracks disappeared in this region. The advantage of the components, made up with mixed microstructure (with and without secondary arms) is their high yield strength with higher percentage elongation at the fracture point.

It is shown that the rate of solidification is a function of the scan velocity [77], and the microstructure at various locations changes due to the preheating effect caused by the previous layer deposition (the temperature of the substrate increases along with the deposition process).

That should also be noted that the aforementioned results were obtained throughout the process parameters listed in Table 3.1. As mentioned, the rate of solidification is a function of the traverse speed and it was shown that with different deposition speed, the formed microstructures might be different. However, the main goal was to show the relationships between the thermal history and the formed microstructures in LSFF.

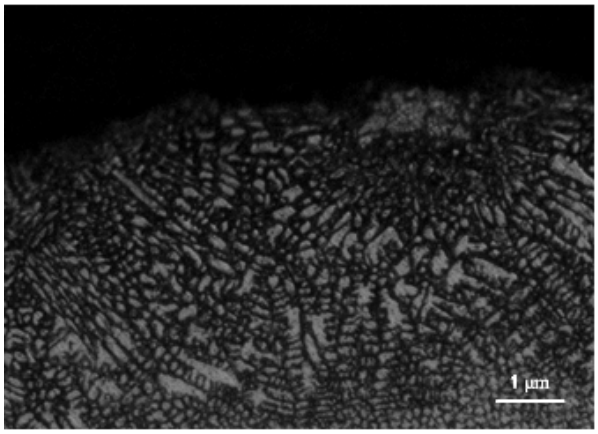

(a)

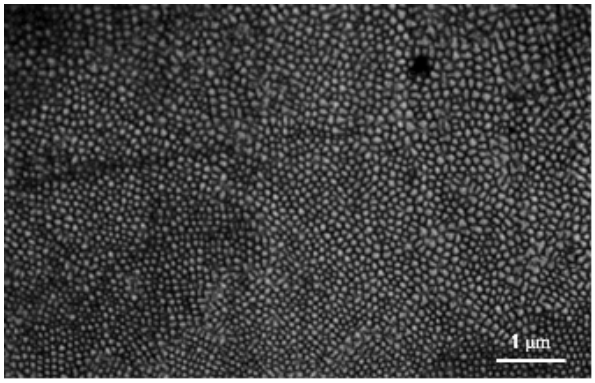

(b)

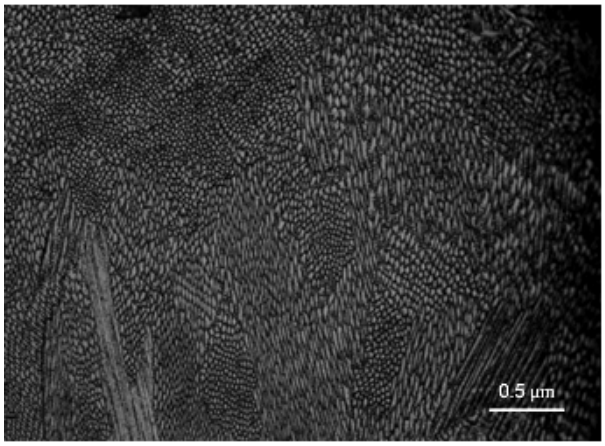

(c)

Figure 4.12 Various Microstructures formed in the thin wall fabricated using LSFF: a) Equiaxed dendrites, b) Dendritic without secondary arms, and c) Mix of both

4.4 Effects of Path Patterns on Thermal Stresses and Geometry of Parts Fabricated Using the LSFF Process

A proper path pattern for the material deposition in the LSFF process has a determining role in the geometrical accuracy of the fabricated part using layered manufacturing techniques. Particularly in LSFF, a proper path pattern also has a determining role on the thermal stress fields and consequently on potential delamination and crack formation across a fabricated part. Some of the most important issues associated with the path pattern will be addressed in this section.

LSFF as a layered manufacturing technique is fundamentally based on a different fabrication concept compared to conventional methods. Using the LSFF process, an object can be built by adding material to the design domain instead of removing material. Therefore, as briefly pointed out in the first chapter, one of the major advantages of the layered manufacturing technique, specifically the LSFF process, is that the geometrical complexity of the object does not have a significant effect on the manufacturing process due to the decomposition into 2D layers [6]. Furthermore, there are also various differences and similarities among the layered manufacturing methods based on their characteristics. For example in shape deposition manufacturing (SDM), using a support structure is a key feature [78].

One of the major differences between LSFF and other layered manufacturing techniques is that the width of each deposition (i.e., clad) depends on the size of the laser beam. Therefore, based on the part geometry, the laser beam and powder stream must trace a defined path to cover the whole surface of the 2D cross-section of the object to be created. However, LSFF has the capability of deposition along multiple axes which makes it possible to orient the part during the fabrication process [79]. Therefore, path planning in LSFF is a process in which sequential paths should be generated for the material deposition system in order to make a 2D surface with finite-width lines of the clad beads overlapping or at top of each other. Two common path topologies used in different engineering applications, which require covering a surface with finite-width scan lines, are the direction-parallel path and contour-parallel path, also known as the spiral path. The direction-parallel path can be

classified into two groups: the one-way path and the zigzag path [80, 81, 82]. Different path patterns are shown in Figure 4.13. Direction-parallel path patterns (one way and zigzag) can also be employed for fabrication 2D vertical objects like a thin wall.

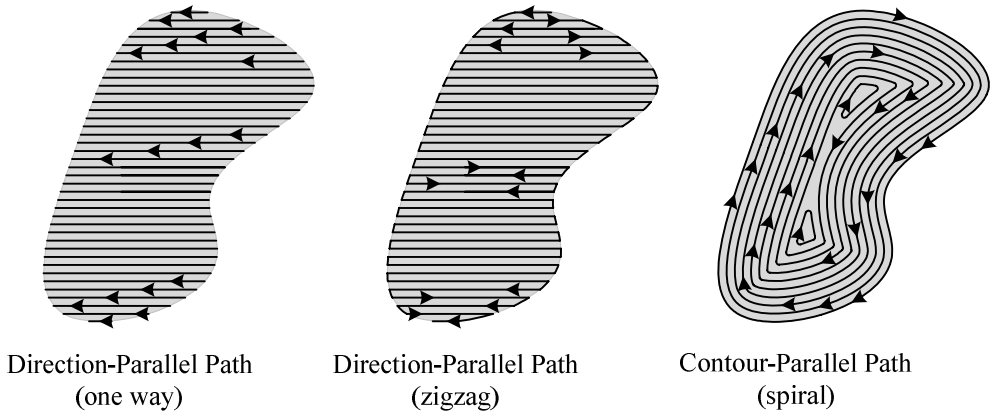

Figure 4.13 Types of deposition path patterns in LSFF

The one way path has usually the longest deposition time compared to other patterns. However, the determining factors in selecting a path pattern for the material deposition in the LSFF process are those that have the most influence on the geometrical aspect and the mechanical properties of a formed part (i.e. temperature distribution, and consequently thermal stresses), namely [79, 81, 83]:

- The path pattern should be planned in such a way that all points on the 2D surface will be covered by the material deposition system only once, ensuring there will not be any non-deposited or over-deposited regions on the surface.

- The path pattern has an important effect on the thermal distribution, and consequent thermal stress throughout the process domain. Depending on the geometry of the part to be manufactured, a symmetrical deposition path pattern results in an even heat distribution, and accordingly a reduction of the thermal stresses across the fabricated structure.

- Based on the geometry of the part, if there are many separate deposition segments in the path pattern, the laser system might be turned on and off repetitively. A delay in

the stability of the laser power may lead to mechanical or geometrical deficiencies in the part.

Although the above factors are of most importance to the final physical quality of a fabricated object, they are highly dependent on the material and geometrical specifications of the object. Therefore, all important factors regarding material and physical specifications of a part should be taken into account prior to the fabrication process within the path planning stage.

4.4.1 Effect of path pattern - case studies

The effects of rastering pattern (path pattern) on the potential delamination within the deposition of WC-Co on the substrate with the same material were studied through an experimental-numerical investigation [84]. The same modelling approach presented in Chapter 3 was used to conduct the numerical study. The proposed modelling approach has the capability of defining different path patterns such as circular, zigzag or one way. Path patterns can be defined through the boundary conditions, Equations (3.8) and (3.9). Experimental analyses showed that a few rastering patterns led to delamination of the deposit WC-Co, while some did not. The depositions were performed on a substrate with the dimension of 12×12×10 mm in x, y, and z directions, respectively. The experimental procedure was the same as described in Section 3.9.1 but with a traverse speed of 3 mm/s, and powder feed rate of 6 g/min. The radii of the laser beam and the powder stream on the substrate were 0.6 mm and 0.7 mm, respectively.

Experimental results for two deposition path patterns are depicted in Figure 4.14a and Figure 4.14b. Figure 4.14a shows the result for a one way deposition pattern and Figure 4.14b shows the result of the deposition of WC-Co using a flip-flop or offset overlap pattern. In the flip-flop deposition path pattern, the first tracks are deposited with a definite offset without overlapping each other. The gaps between the first deposited tracks are then filled to cover the whole 2D surface. The results showed that the deposited WC-Co delaminated for the process using a one way path pattern as seen in Figure 4.14a. The delamination was observed after the deposition of two tracks. The deposited material was then warped as the numbers of tracks were increased. In contrast, no delamination was observed in the result

obtained from the sample prepared using the flip-flop path pattern. The result for this case is shown in Figure 4.14b.

(a)

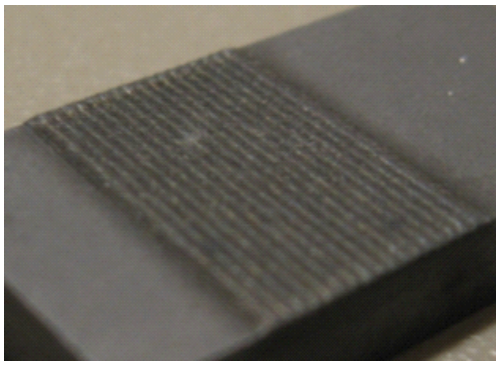

(b)

Figure 4.14 Deposition of WC-Co: a) With continuous one way path pattern, b) With flip-flop path pattern (Fabricated at the Automated Laser Fabrication (ALFa) Laboratory by Dr. C.P. Paul)

In order to study and justify the experimental results regarding the effects of the rastering patterns on the delamination of the deposited material, two FE models with different deposition patterns were developed using the same process parameters. For the first model, the laser beam was considered to scan two straight lines with 60 per cent overlap (one way pattern). The same time as was required for each track deposition was inserted between successive deposited tracks in order to bring the laser beam back to its starting point, as was done in the experimental routine. The path pattern for the second

model was designed for depositing of two successive tracks without overlapping (5 mm distance between two tracks, flip-flop pattern).

The numerical results showed that the maximum stress for the second track of the flip-flop pattern at this region is 4.78 per cent less than for the one way pattern. It should be noted that the difference between the maximum stresses for these two cases increases at the starting points. For instance, after 0.75 mm from the starting points, the maximum stress in the second pattern is 6.41 per cent less than the first pattern for the same region. The numerical results of the models developed for the depositions based on these two different path patterns demonstrate the same results obtained from the experimental analyses. The possibility of having delamination or crack formation for the one way pattern is more than for the flip-flop pattern. Therefore, it is better to consider a rastering pattern which covers a surface from different starting points and switch between these regions to cover the whole surface instead of covering the surface from one side to the other side continuously.

Another study conducted by Nickel et al. [55] investigated the effects of different path patterns on the deflections of a beam and a plate. Their experimental and numerical results showed that depositions on a beam using a one way pattern along a shorter axis produces less deflection than the deposition along the longer axis. For the plate, amongst one way, spiral deposition from inside to outside and spiral deposition from outside to inside, the spiral deposition from outside to inside produces the most uniform clad and the least deflection compared to the other two patterns. The results also revealed that a symmetric spiral deposition pattern produces better results than a non-symmetric one way pattern. The specification of their numerical model was given in Section 3.1.

4.4.2 Geometrical issues in LSFF

As shown and discussed in Section 4.2, the thermal nature of the LSFF process creates some geometrical problems in the fabrication of parts using this technique. There are some more reported geometrical concerns resulting from either the layered manufacturing aspect or temperature distribution induced in the fabrication process. As cited, due to limitation on the width of each track, multiple clad beads must be deposited side by side to cover a large area, and in order to have a smooth surface with minimum roughness, the clad beads have

to be overlapped as schematically shown in Figure 4.15. Li et al. [85] have proposed a realistic but simple analysis of the overlapping process. In this study, the following assumptions were considered to simplify the analysis: the cross section profile of a single clad bead was assumed as a symmetric parabolic arc, dilution during the process was not taken into account, and the cross section profile of previous deposited clad tracks remain unchanged during overlapping.

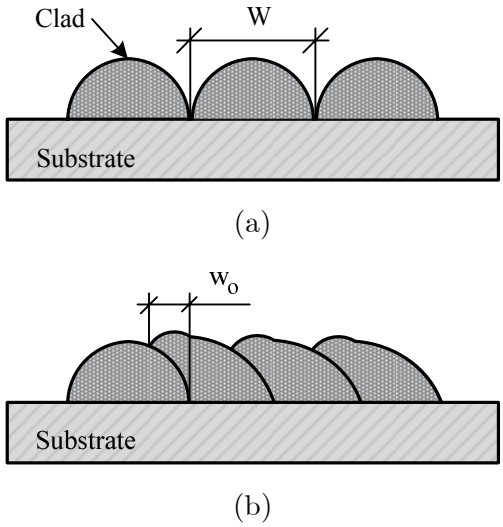

Figure 4.15 Schematic cross sections of the clad tracks: a) Without overlapping (w is the clad width), b) With overlapping (w_o is the overlapped width)

Another geometrical problem which arises from the nature of the LSFF process occurs at the turning points on a deposition path. Compared to the regions with normal material deposition, the interior corner at the turning region on the path is over deposited whereas the exterior corner is under deposited, as schematically shown in Figure 4.16. This problem is amplified and clearly visible when more layers are added. Singh et al. [86] have experimentally addressed this issue. They recommended decreasing the effects on the final product by staggered start/stop deposition points.

This issue only occurs in the zigzag and spiral path patterns, since there is no change of direction in one way direction-parallel path. Hence, this situation can be avoided using a one way path pattern for the material deposition. Furthermore, in one way and spiral patterns,

there are many deposition segments with separate start/stop points. Instabilities on start/stop points affect the geometrical accuracy of the clad at those regions.

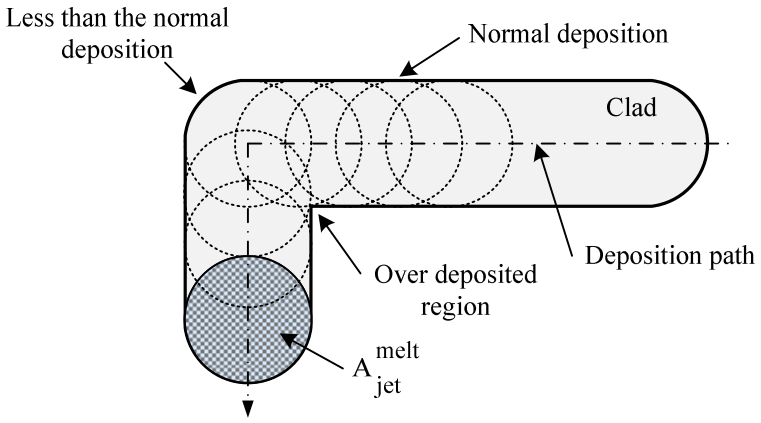

Figure 4.16 Material deposition at the corner of a clad bead

In addition to the path pattern of each layer that influences the geometrical accuracy of a manufactured part using the LSFF process, there are some other factors associated with the formation of multiple layers (i.e., slicing methods). One of the main problems in this category is stair-step error. This error is a result of the nature of the layered manufacturing that the surface of the fabricated object is formed by stepped shape boundaries of the consecutive layers as shown in Figure 4.17. Majhi et al. [87] and Kulkarni et al. [88] have proposed optimum slicing algorithms to minimize the stair-step errors. Depending on the geometry of the part, the stair-step error can be constant or varied for different layers. For example, the errors in Figure 4.17a are different for each layer while in Figure 4.17b they are constant.

The vertical deposition in layered manufacturing including LSFF also creates a surface with steps similar to the overlapping effect as shown in Figure 4.18. Although these types of geometrical problems can usually be reduced by the reductions of the layer thicknesses, this might compromise the consistency of the mechanical properties of the part. However, the selection of an optimum set of process parameters can help to improve the surface quality while keeping the mechanical and metallurgical qualities of the part within desired tolerances.

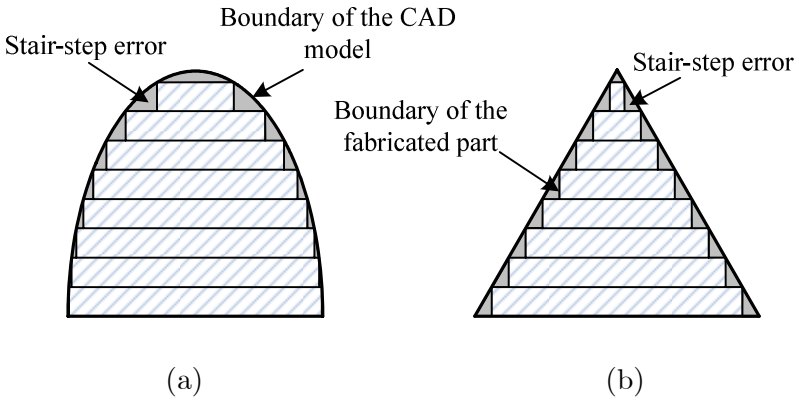

Figure 4.17 Stair-step errors in LSFF

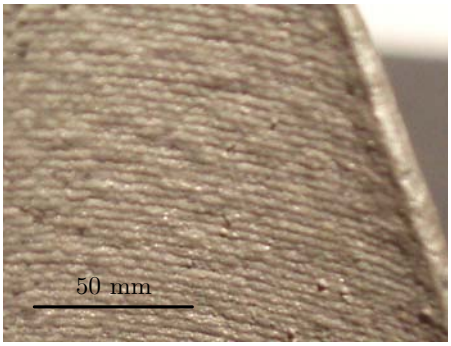

Figure 4.18 Surface quality of a part fabricated using the LSFF process

4.5 Thermal Stress Management

Thermal stress is a tension or compression within the body of an object caused by temperature gradient without the existence of an external force or displacement. As described in Equation (2.8) and previous sections, the temperature gradient caused by a moving concentrated heat source (laser beam) throughout the process domain in a cyclical fashion results in thermal strains. Therefore, in LSFF, the deposited layers are normally subject to the large thermal stresses leading to delamination and crack formation. This phenomenon predominates when the hardness of deposited layers is high [70]. In the previous section, the critical effect that the path pattern used for the material deposition has on the form of the thermal distribution and subsequently the thermal stresses throughout a

fabricated part was described. In addition, in Section 4.2, based on the numerical results, it was pointed out that it is possible to manage the thermal stresses by controlling the thermal distribution within the fabrication process. This will be discussed in more detail in the next section.

4.6 Effect of Preheating on the Delamination and Crack Formation of a Thin Wall Fabricated Using the LSFF Process

In this section, the numerical and experimental investigations for fabrication of a thin wall presented in Chapter 3 and preceding sections of this chapter are further extended to investigate the correlation between the numerical results and the locations of possible delamination/crack formations across the fabricated parts. For this purpose, it is necessary to study the time-dependent temperature distributions and thermal stress patterns along with their evolution throughout the fabrication process. Using the modelling approach presented in Chapter 3, 3D temperature and thermal stress distributions for the four-layer thin wall can be obtained at any elapsed time during the fabrication process. For instance, for the second layer deposition, the temperature and thermal stress patterns on the surface normal to the y axis at $y = 0$ and $t = 5$, and $t = 8.65$ s are shown in Figure 4.19 and Figure 4.20, respectively. These two figures demonstrate the transformations of the thermal stress and temperature distribution patterns along the fabrication path. When the laser beam is in the middle segment of the wall (as shown in Figure 4.19), the stress concentration occurs only around the melt pool region. As the laser beam approaches the end segment of the wall, the stress concentration field grows and two concentrated areas around the melt pool and the corner of the wall are formed. The thermal stress pattern for this case can be seen in Figure 4.20. The same phenomenon takes place at the other corner of the wall as well as in the subsequent layers. However, in order to comprehensively study the effects of the temperature and thermal stress fields on the qualities of the fabricated parts (i.e., delamination and cracks), in addition to the temperature and thermal stress distributions, their variations throughout the whole process provide another perspective regarding the trends of the temperature and thermal stress transformations throughout the fabrication process.

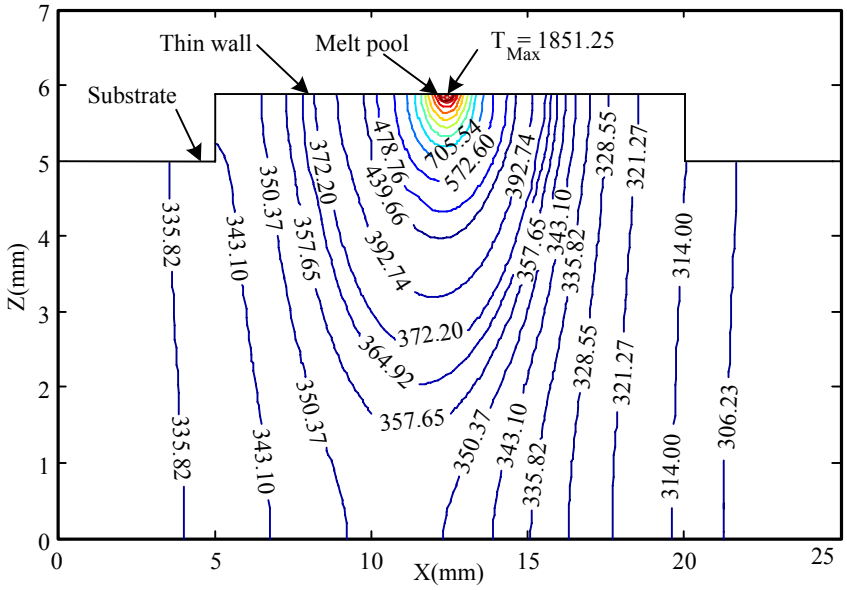

(a)

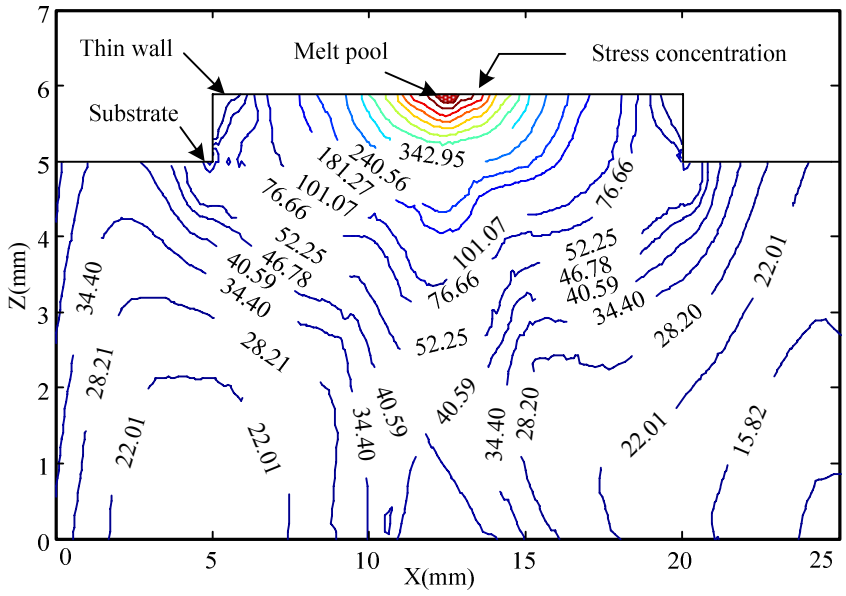

(b)

Figure 4.19 a) Thermal field (Isothermal contours (K)), b) Stress field (Von Mises (MPa)) for the second layer deposition at $t = 5$ s on the surface normal to $y = 0$

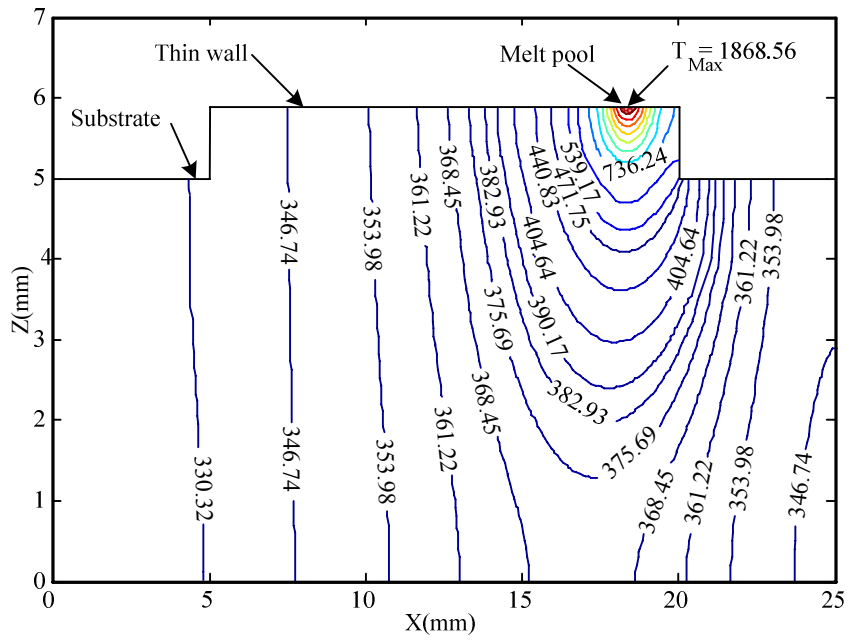

(a)

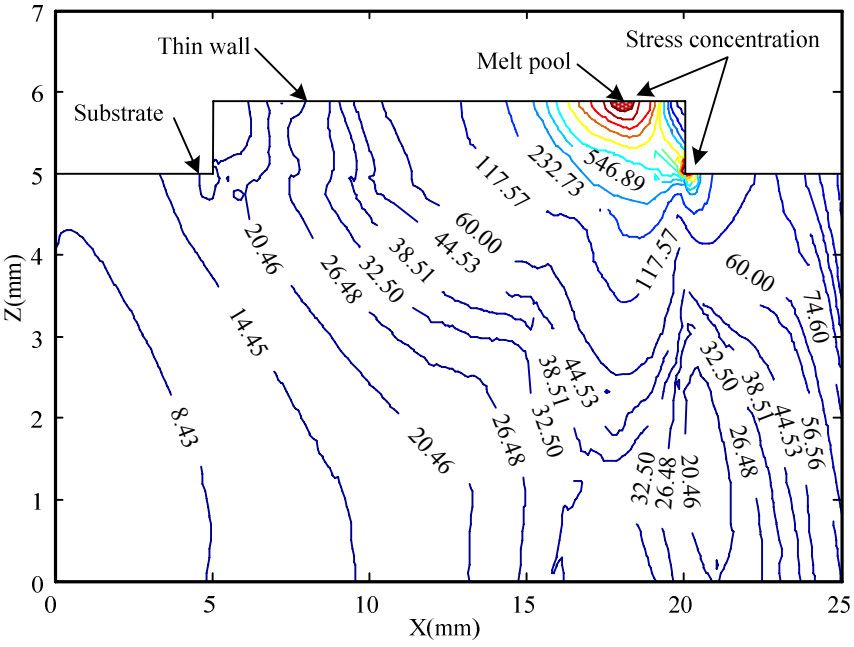

(b)

Figure 4.20 a) Thermal field (Isothermal contours (K)), b) Stress field (Von Mises (MPa)) for the second layer deposition at $t = 8.65$ s on the surface normal to $y = 0$

The numerical results of the maximum temperatures of all layers along the deposition track were shown in Figure 4.3. This figure also shows the position of the laser beam on the substrate considering its corresponding fabrication time. For instance, at the simulation time $t = 6.66$ s, the laser beam is located at $x = 15$ mm on the substrate or $x = 10$ mm on the deposition track. At this position, the corresponding maximum temperatures for the first to the fourth layer can be found on the intersection of the dotted line shown in Figure 4.3 with the maximum temperature profiles.

Due to geometrical changes, and consequently the nature of heat loss, the maximum temperatures for the first to the fourth layer increase throughout the build-up process as discussed in Chapter 4 and as shown in Figure 4.3. It was shown that due to the nature of heat loss throughout the build-up process, the maximum temperature increases with increasing numbers of deposited layers. The same effect was also observed between the middle and the end segments of the wall. The thermal behavior and the relationship between the temperature distribution and the geometry of the deposited material in the multilayer LSFF are studied in detail by Alimardani et al. [15], and were also described in Section 4.2.

Although the temperature increases throughout the LSFF process, the thermal stresses exhibit a different interesting behavior. Due to the geometrical changes and the decrease in thermal gradients throughout the process (which is a result of an increase in the substrate temperature within the build-up process), the average maximum thermal strains and consequently thermal stresses decrease (as discussed in detail in the previous chapter). On the other hand, because of the sudden geometrical changes, although the average thermal stresses decrease during the LSFF process, the maximum stresses still occur at the end segments of layers 2 to 4. This was illustrated in Figure 4.6 in which the maximum stresses of several points on the first layer imposed by the depositions of the second to fourth layers were shown. The numerical results indicate that the thermal stress patterns, which determine the regions with more propensity to delamination and crack formation, are a function of the temperature distribution and the geometry of the deposition zone. To verify the numerical results, as well as investigate the correlation between the thermal stress fields and the locations of the possible delamination and crack formations, the microscopic views of

different cross-sections of the thin wall, which was experimentally built up and also explained in Chapter 3 and Chapter 4, were studied for the first to the fourth layer.

The micro-cracks formed in the experimentally fabricated wall exhibit the same trend predicted by the numerical results. To show this, Figure 4.21 depicts three cross-sections normal to the x axis, after deposition of the second layer. The positions of the cross-sections are at $x = 7$, 12.5, and 18 mm, relative to the coordinate system shown schematically in Figure 3.10. To study the micro-cracks across the experimentally fabricated wall, the samples were cleaned and polished to metallographical quality, and then examined using optical and scanning electron microscopes. As seen in Figure 4.21, there are many micro-cracks formed close to the substrate along the first layer deposition due to the larger thermal stresses in the first layer (the average maximum thermal stresses of the first layer is 24 per cent larger than its counterpart for the second layer throughout the deposition track). In addition, compared to the beginning and end segments, the number of micro-cracks per unit width is almost half at the middle segment as the result of the lower thermal stresses in this region. This trend was predicted by the simulation results. As shown in Figure 4.3**,** Figure 4.6, Figure 4.19, and Figure 4.20, high stresses at the two end segments of the wall for layers 2 to 4 as well as the stress concentration at the corners of the wall connected to the substrate (which was due to the heat transfer mechanism and geometrical changes) result in more cracks at these locations. This fact is also demonstrated explicitly in Figure 4.7.

The numerical results as well as the relationship between the thermal strain/stress and temperature gradient (defined based on the thermoelastic constitutive equations [62]), indicate that by controlling the thermal gradient/temperature distribution and the geometrical changes throughout the fabrication process, it is possible to control the contraction caused by the thermal strains, and consequently thermal stresses. Therefore, to reduce delamination and cracking, the temperature gradient formed during the LSFF process should be kept as small as possible. Since for the first layer deposition, the process starts at the initial temperature of the substrate (normally the ambient temperature), the temperature gradient is larger than its counterparts for subsequent layers. This accordingly results in larger thermal stresses for the first layer. This effect can be controlled by preheating the substrate.

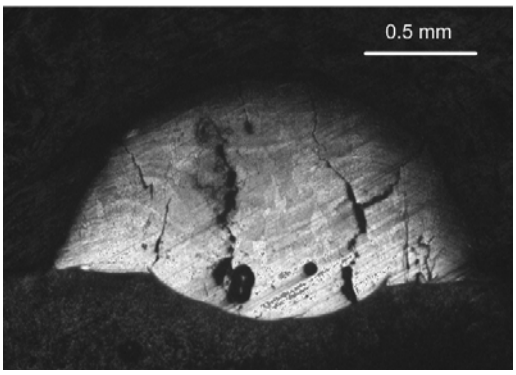

(a)

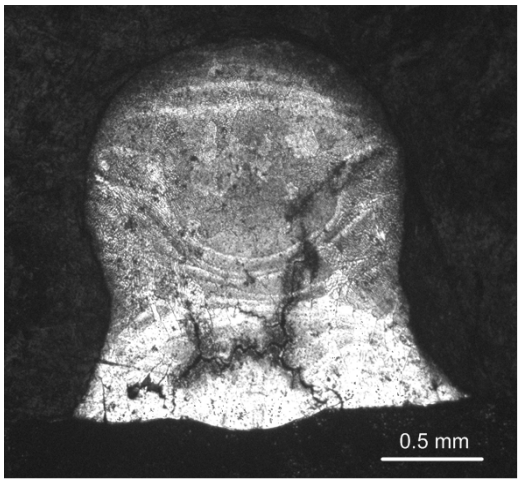

(b)

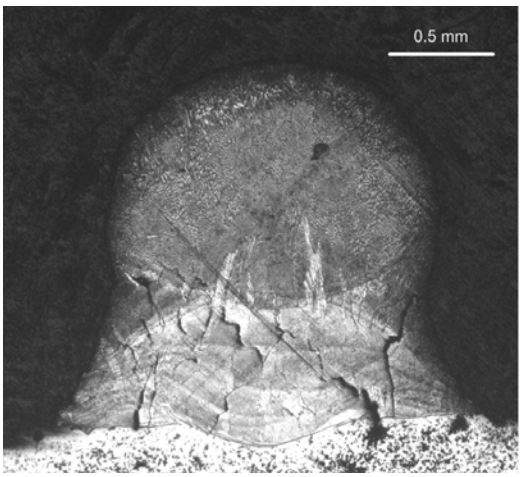

(c)

Figure 4.21 Transverse section of two-layer deposition at: a) 7 mm, b) 12.5 mm, and c) 18 mm from the start edge

To further examine the effect of preheating, preheating the substrate prior to the fabrication process and its effect on the temperature distributions, and consequently thermal stress fields induced throughout the LSFF process are next numerically and experimentally investigated.

Figure 4.22 shows the simulation results for the maximum temperatures of the process along the deposition track for the substrate preheated to 400, 600, and 800 K prior to the first layer deposition. One of the interesting features demonstrated in this figure is that the transient time for developing a properly formed melt pool is shorter in the preheated models, considering the melting temperature of the powder and the substrate. For instance, the melt pool forms after 0.05 seconds from the starting time for the model preheated to 600 K, while this takes 1.7 seconds for the non-preheated model (i.e., point M) , as shown in Figure 4.22 [Note: that the noisy data resulting from the mesh density in the melt pool boundary were smoothed using a moving average technique. Finally, the curves of the maximum stresses for each preheated model were fitted to the numerical data using a quadratic polynomial]. This can cause a better bonding between the first layer and the substrate, and consequently it can prevent delamination and crack formation in the first layer during the deposition of subsequent layers.

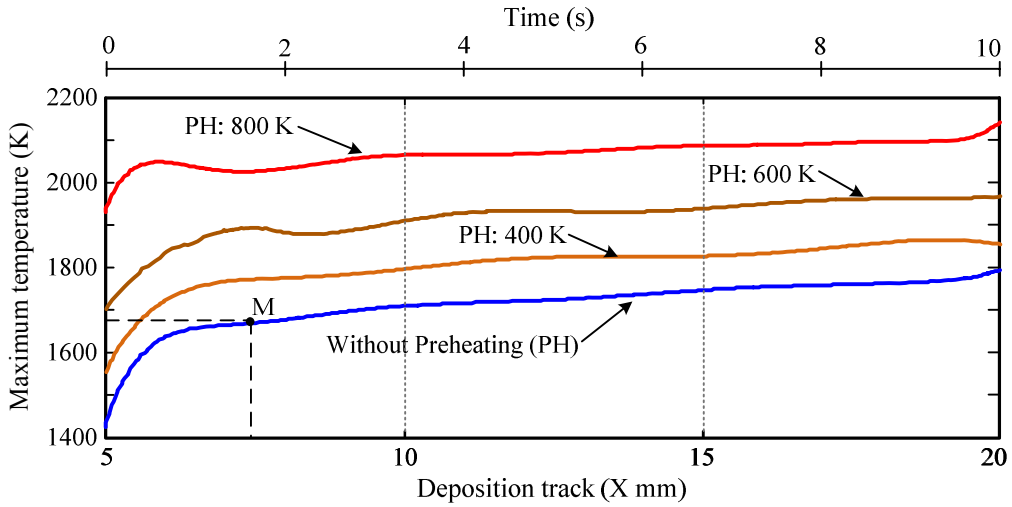

Figure 4.22 Maximum temperatures (K) along with the deposition track for the first layer with preheating the substrate prior to the LSFF process

Figure 4.23 shows time-dependent thermal stresses at 0.5 mm (on the zx plane at $y = 0$) from the melt pool boundaries (i.e., solid-liquid interface) for the models in which the substrate was preheated prior to the fabrication process from 400 to 800 K for every 100 K interval. The data used to create this figure were processed with the same method as explained for Figure 4.22. The figure shows that the thermal stresses are reduced by the preheating of the substrate.

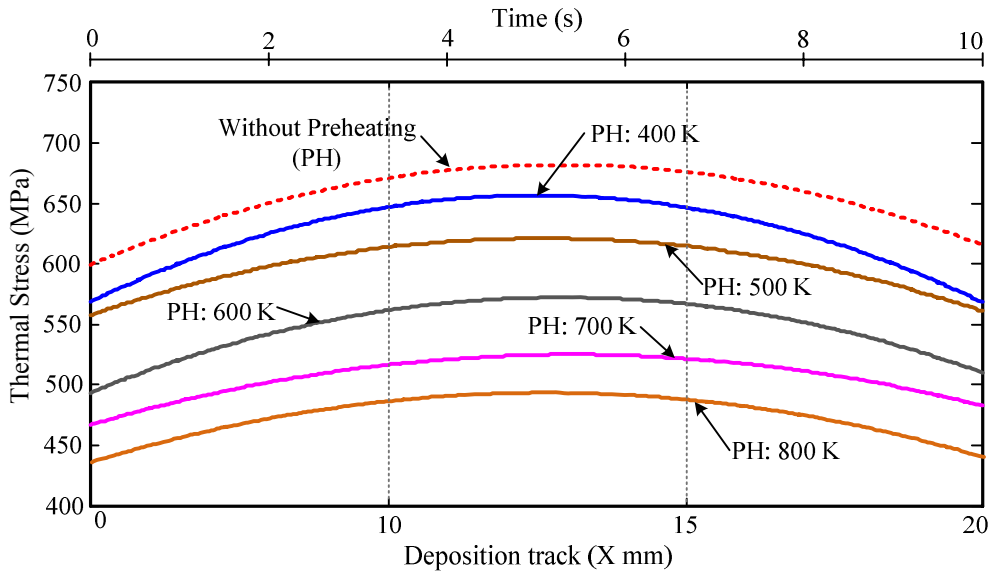

Figure 4.23 Von Mises thermal stresses (MPa) for the first layer with preheating the substrate prior to the LSFF process at 0.5 mm far from the melt pool boundaries

As seen in Figure 4.22, the maximum temperatures increase with a positive ratio in the course of preheating the substrate from 400 to 800 K. This characteristic provides an advantage for reducing the laser power while still having a proper melt pool. To explore this feature and its feasibility, the LSFF process was also simulated for each preheated substrate with laser powers of 250 and 200 W. For the substrate preheated to 800K, Figure 4.24 illustrates the maximum temperatures along with the deposition track for the processes with the different laser powers. As seen, by reducing the laser power to 250 W, a proper melt pool is still formed in addition to a shorter transient time for reaching its fully-developed condition. The slopes of the maximum temperatures also show that the processes with

preheating have a more consistent melt pool compared to the process without preheating the substrate.

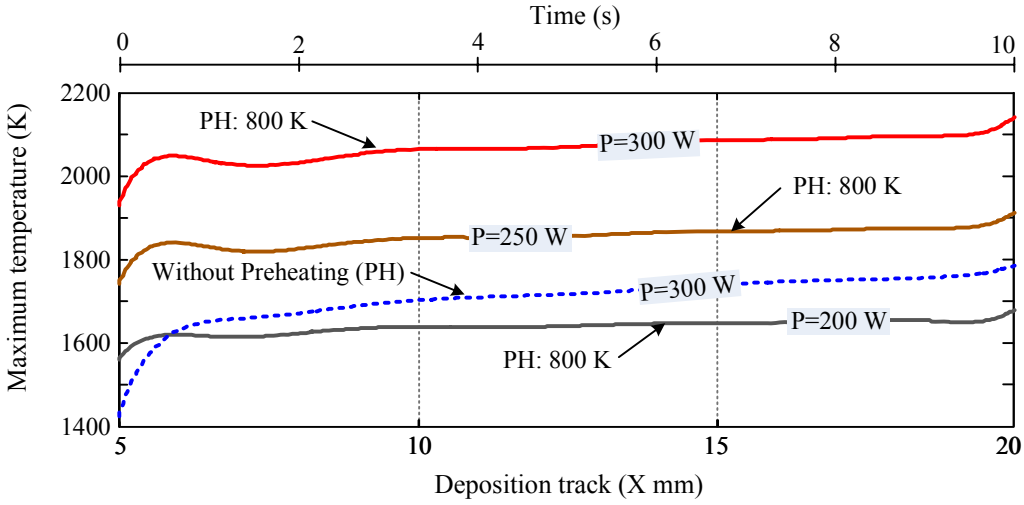

Figure 4.24 Maximum temperatures (K) along with the deposition track for the first layer with 800 K preheating the substrate and different laser powers

To study the preheating effect on the temperature distribution and thermal stress field more comprehensively, Figure 4.25 shows the average maximum temperatures for non-preheated and preheated models with different laser powers (300, 250, and 200 W). Considering the melting temperature of the substrate and powder particles, the figure indicates the region in which the proper melt pools are formed. Corresponding to these cases, Figure 4.26 shows the thermal stresses at 0.5 mm (on the zx plane at $y = 0$) from the melt pool boundaries throughout the deposition track. For instance, the thermal stresses at the melt pool boundaries for the model preheated to 800 K with the laser power of 300 W show 28 per cent reduction compared to the non-preheated model. On the other hand, the thermal stresses for the same model, but with the laser power of 250 W, show a 34 per cent reduction.

It should be noted that the thermal stresses shown in Figure 4.23 and Figure 4.26 do not fully represent the trend by which the stress distributions throughout the process domains of different cases can be compared to each other. This results from the fact that the melt pool boundary for each case occurs at different locations due to the different melt pool sizes (i.e.

maximum temperature for each case is different). To compare the stress distribution induced in the process domains for the different cases, Figure 4.27 illustrates the maximum thermal stresses under the melt pool path at z = 0.0045 mm on the xz plane.

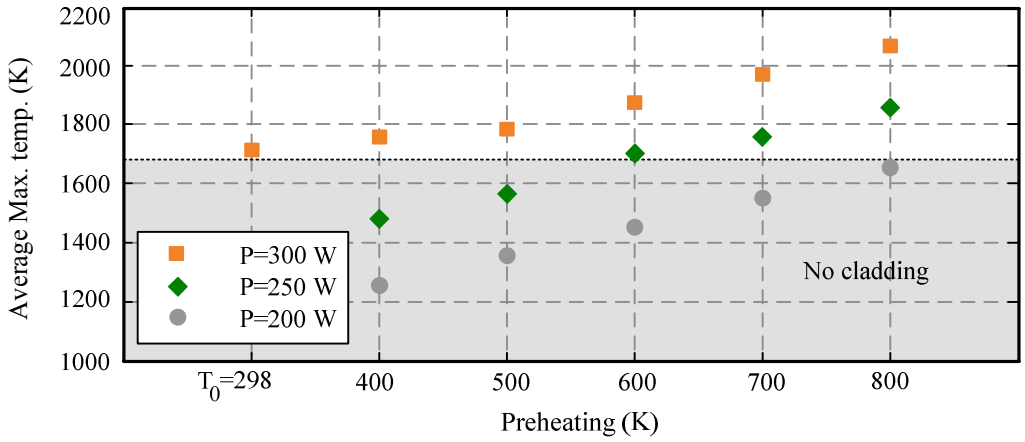

Figure 4.25 Average maximum temperatures for different preheating and laser powers of 200, 250, and 300 W

Figure 4.27 shows that the thermal stresses do not show a significant decrease after preheating the substrate to 500 K (with the same laser power). But, as seen, the maximum thermal stresses show a significant reduction by decreasing the laser power without compromising the melt pool condition since the maximum temperatures show increases with a positive ratio in the course of preheating the substrate from 400 to 800 K as shown in Figure 4.22 and Figure 4.25. For instance, for the substrate preheated to 700 K, the average maximum stresses are reduced by 16.7 per cent by decreasing the laser power from 300 to 250 W, while the value for this case with the same laser power of the non-preheated model shows only a 3.6 per cent reduction. For this case, the melt pool temperature also shows a 3 per cent increase with respect to the non-preheated model. These results demonstrate that the maximum temporal thermal stresses are significantly reduced by optimizing the laser power along with preheating the substrate.

To verify the numerical results and study the effect of the preheating on the micro-cracks formed in the thin wall, related experiments with the same procedure explained in the

preceding section were conducted. In these experiments, two substrates were preheated to 600 and 800 K, and the same thin walls were fabricated for these two cases with the laser power of 250 W, while other process parameters were kept the same as listed in Table 3.1. Figure 4.28 shows three cross-sections of the build-up for the sample preheated to 800 K at x=7, 12.5, and 18 mm, relative to the coordinate system schematically shown in Figure 3.10. Inspection of these cross-sections confirms the crack-free surfaces for this sample. Inspection of the cross-sections of the sample preheated to 600 K shows a few isolated micro-cracks at the bottom of the middle cross-section, as illustrated in Figure 4.29. The experimental results also confirmed good bonding between the deposited layers as well as with the substrate.

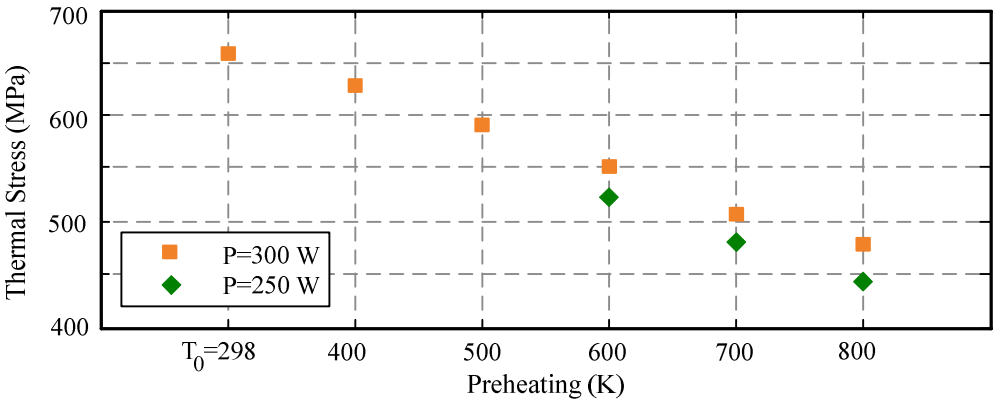

Figure 4.26 Average Von Mises thermal stresses at 0.5 mm far from the melt pool boundaries for different preheating and laser powers of 250 and 300 W

Based on the numerical results summarized in Figure 4.25 and Figure 4.27, it is possible to define critical values for the maximum temperature and thermal stresses, and consequently for the process parameters throughout the LSFF process. These critical values, which determine the quality of the fabricated parts, are a function of process parameters, material properties, and geometries of the deposition zones. For instance, based on the specific defined process parameters, material properties of SS304L, and the geometry of the part used in this work, for a substrate preheated to 600 K, the maximum temperatures throughout the fabrication process were the same compared to the non-preheated substrate while its maximum stresses were reduced by up to 21.6 per cent. However, determining a

comprehensive optimum set of process parameters requires more experimental and numerical analyses based on the role of each operating parameter on the whole process.

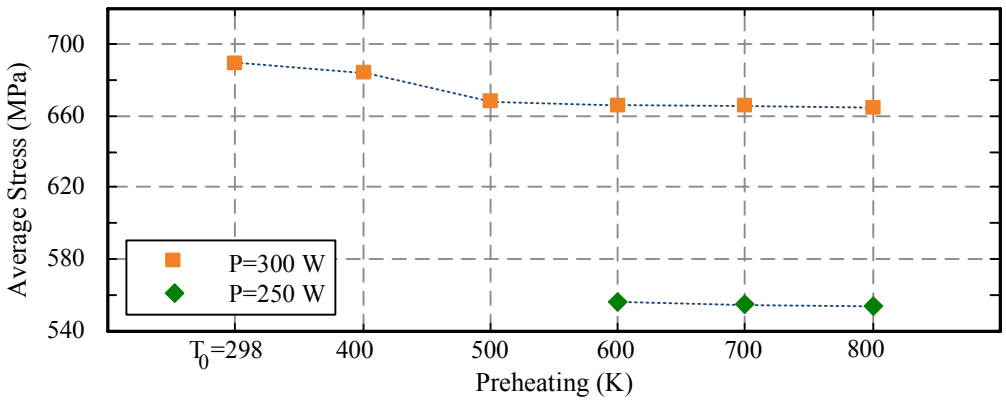

Figure 4.27 Average maximum Von Mises thermal stresses of the track, under the melt pool at z = 0.0045 mm on the *xz* plane, for different preheating and laser powers of 250 and 300 W

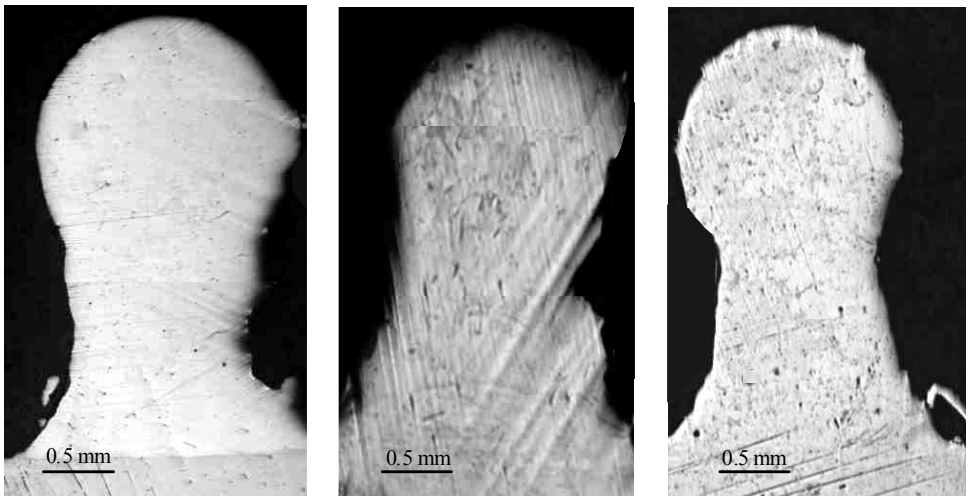

Figure 4.28 Cross-section of the thin wall with substrate preheated to 800 K at: a) x=7 mm, b) x=12.5 mm, and c) x=18 mm

Figure 4.29 Isolated micro-cracks in cross-section of the thin wall at $x = 12.5$ mm with substrate preheated to 600 K

4.7 Summary

Since the LSFF results strongly rely on the temperature distribution and its transformation throughout the fabrication process, studying this aspect of the process is of crucial importance. The LSFF model developed in the last chapter was used to investigate the time-dependent thermal characteristics of the process during the fabrication of a four-layer thin wall of AISI 304L steel using a pulsed Nd:YAG laser. The temperature distributions and its evolution along with the thermal stresses induced throughout the process were studied. The effect of the melt pool temperature on the geometry of the wall was also investigated. The results showed that the temperature distributions under a predefined set of the process parameters vary with the geometrical formation of a part throughout the fabrication process. Due to geometrical changes, and consequently the nature of heat losses, the maximum temperatures for the first to the fourth layer increase throughout the build-up process. This behavior results in higher temperature and a larger melt pool, which consequently results in a higher powder catchment. The same effect was also observed between the middle and the end segments of the wall. With the same process parameters throughout the build-up process, the results in terms of the thermal stresses showed that the changes in the thermal stresses are a function of the time-dependent geometry of the process domain, and the temperature gradients. This is also implied by the governing equations presented in Chapter 2. Moreover, the results revealed that contrary to the maximum temperatures over the

build-up process, the average maximum of thermal stresses decrease from the first to the fourth layer depositions.

Along with a review of the research program investigating the microstructures formed in the LSFF process, the experimental and numerical results of the simulated thin wall were also further extended to study the variations of the microstructure through a multilayer deposition and its correlation with temperature distributions. Based on the temperature gradient at the solid/liquid interface and cooling rate, various microstructures such as dendritic with and without secondary arms (and their mix) are formed throughout the fabricated wall. These microstructures can be predicted using the temperature history of each point developed using the FE model. In general, the results showed that the presented numerical results have good potential to predict this complex process and give a perspective of the microstructure of the fabricated part based on the temperature history and the developed stress field during the LSFF process.

Investigation of thermal characteristics of the LSFF process revealed that by controlling the thermal distribution and sudden geometrical changes, it is possible to manage the thermal stresses as the main source for cracks and delamination. The effects of path patterns on the temperature distributions and stress fields were studied. In addition, the numerical and experimental results of a fabricated thin wall showed that by preheating the substrate prior to the fabrication process, it is possible to substantially reduce the micro-cracks formed across the part. For instance, by preheating the substrate to 800 K, the thermal stresses formed during the fabrication process showed 22 per cent reduction.

Chapter 5

Effects of Process Parameters and Material Properties in LSFF

In LSFF, process parameters define the final quality of the fabricated parts. To control the process, having a profound knowledge of these parameters and their effects on each other as well as on the final build-up is of great importance. An optimum set of process parameters can tremendously improve the quality of the fabricated parts and also alleviate the complexity of the LSFF process control plan. In addition, among different process parameters, those related to the material properties are very important for fabrication of multi-material components (heterogeneous structures). In multi-material fabrication, besides the effects of material properties, the influence of their variations on the LSFF process has also to be taken into special consideration during the fabrication process planning. In continuation of a basic definition and discussion of the process parameters in the first two chapters, this chapter reviews the roles of these parameters more specifically on the fabrication process. However, the main concern of this chapter is the fabrication of heterogeneous objects and the effect of the material properties and their variations on the temperature distribution and thermal stress fields. This is achieved by a preliminary investigation using the numerical approach introduced in Chapter 3 by applying appropriate modifications for a multi-material deposition process.

5.1 Effects of the Process Parameters in LSFF

Section 2.3 defined the main process parameters in the LSFF process. It was explained that the LSFF process is governed by a large number of process parameters related to the process domain such as material properties and to the equipment including the motion device and laser. Table 2.1 lists the main process parameters in LSFF. A large number of parameters have been defined or adopted to represent the operating parameters quantitatively or qualitatively. There are several system and optical parameters that define the laser beam properties such as laser power, focal spot diameter, and laser beam intensity distribution. There are many books and technical articles devoted to the laser beam characteristics specifically for laser material processing applications [16, 23, 89].

In terms of the clad quality and geometry, aspect ratio is defined as a dimensionless number to show the ratio of width to the height of a clad. Steen at al. [16] classified all track cross sections into three main groups. These typical cross sections with their geometrical specifications are shown in Figure 5.1. Figure 5.1a, b, and c show an ideal deposition with minimal dilution, a cross section of a track with high dilution and a clad without dilution which creates inter-run porosity, respectively. For the deposition without inter-run porosity, the angle β (shown in Figure 5.1), should be acute which can be defined by aspect ratio. For the deposition of Stellite 6 without inter-run porosity, it was shown that the aspect ratio should not be less than five.

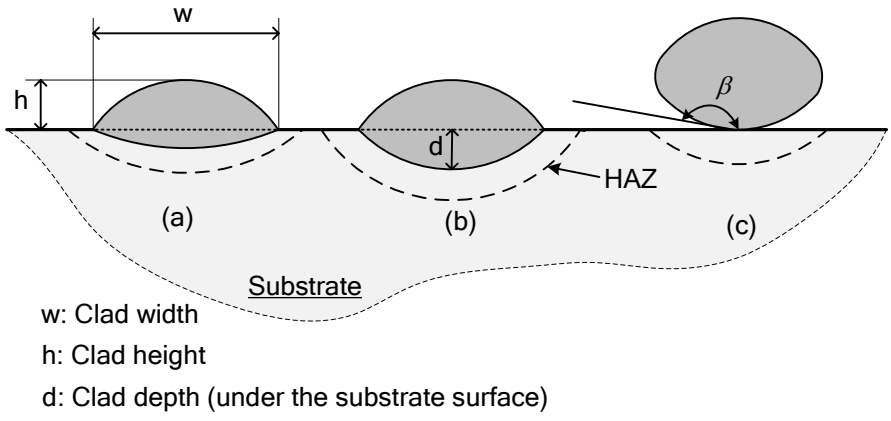

Figure 5.1 Basic cross sections of a single track with: a) minimal dilution, b) high dilution, c) no dilution

There are many reported results in the literature of investigations regarding the effects of process parameters on clad geometrical and metallurgical features. For instance, Kreutz el al. [90] studied the variation of clad height with respect to the powder feed rate over the traverse speed for two different laser power intensities. Their results showed that the clad height increased with laser power intensity and powder feed rate over the traverse speed. The qualities of deposited tracks within the above-mentioned operating conditions were not acceptable at the high and low powder feed rates due to lack of fusion and high dilution, respectively (Dilution can be defined base on the clad geometrical or metallurgical characteristics. Using the geometrical characteristics presented in Figure 5.1, it can be simply defined as the ratio of clad depth, d, to the clad depth and height, $d+h$ [91]). This method of investigation in which the effects of several parameters were studied for quality of the deposited material has been reported by other research groups as well. Using this method (parameters variation), it is possible to define an optimum operating window indicating the ideal operating region based on the variations of different sets of process parameters. These grouped parameters can also be used in control plans for the fabrication process. Another advantage of this method is to report the experimental results more efficiently.

Steen [16] also experimentally defined a process window for deposition of Stellite 6 considering the effect of various process parameters on the process, including laser powder intensity, powder feed rate, and process scanning speed. The process window for Stellite 6 was defined based on the laser power intensity versus feed rate. The optimum region was determined by liming the process window using the following sets of process parameters, $P_1 = \text{aspect ratio}, P_2 = P/\dot{m}D$, and $P_3 = P/UD$ in which P (W) is the laser power absorbed by the substrate, $\dot{m}$ (g/s) is the powder feed rate, U (mm/s) is the scanning speed, and D (mm) us the laser beam spot size on the substrate. For this specific material and using the above sets of parameters, the process window classified several regions with ideal formed clad, no formed clad, high dilution, and porosity. A second set of parameters, P_2, defined a limit for dilution; when this reaches its maximum value, dilution occurs. For this case P_2 was reported as 2,500 J/g.mm. The third set of parameters, P_3, indicates the minimum energy required for forming a clad, and was 22 J/mm^2 for this case.

Based on the reported studies, the effects of changing the laser power, the laser spot size and the powder feed rate, on the dilution, clad height and maximum thickness, melt pool depth, and cracking were investigated using the parametric variation method [20]. For instance, by increasing the laser power, the melt pool depth, dilution, and maximum clad thickness increase while the clad height and cracking decrease. In contrast, by increasing the powder feed rate, the clad height and cracking increase while the meld pool depth, dilution and maximum clad thickness show a decrease. More discussions on parametric studies of the LSFF process are addressed in the literature [16, 20].

With advances in the process modelling, more questions regarding the effects of the process parameters on the final mechanical and metallurgical qualities of the process outcomes have been answered. These include questions which cannot easily be answered through experimental analyses alone, such as the microstructure formation or melt pool behavior and its effect on the clad during the fabrication process. Several investigations on the effects of the process parameters on the physical and metallurgical specifications of the fabricated parts using the modelling approach are addressed in the preceding chapters namely in Sections 2.3, 2.4 and 3.1.

Since the modelling approach presented in Chapter 3 is based on the main process parameters, the developed model can be employed to investigate the effects of the process parameters during the fabrication process as well. For instance, Figure 5.2 shows the effect of the process scanning speed (interaction time) on the temperature history of a point in the process domain, located at (12.5, 0, 5) mm relative to the coordinate system schematically shown in Figure 5.2, within the process domain during the deposition of the first layer. The corresponding cooling rates of each temperature profile are shown in Figure 5.3 for scanning speeds of 0.5 mm/s to 3 mm/s. As seen, by decreasing the scanning speed the interaction time increases. As a result, the maximum temperature when the laser beam is at the designated point, increases. In addition, by increasing the interaction time, the cooling rates substantially decrease, as shown in Figure 5.3. Similar modelling approach and results, presented in Figure 5.2 and Figure 5.3, were used to investigate the effects of the scanning speed on the phase transformations during the deposition of Ti-45Nb on the mild steel substrate [92].

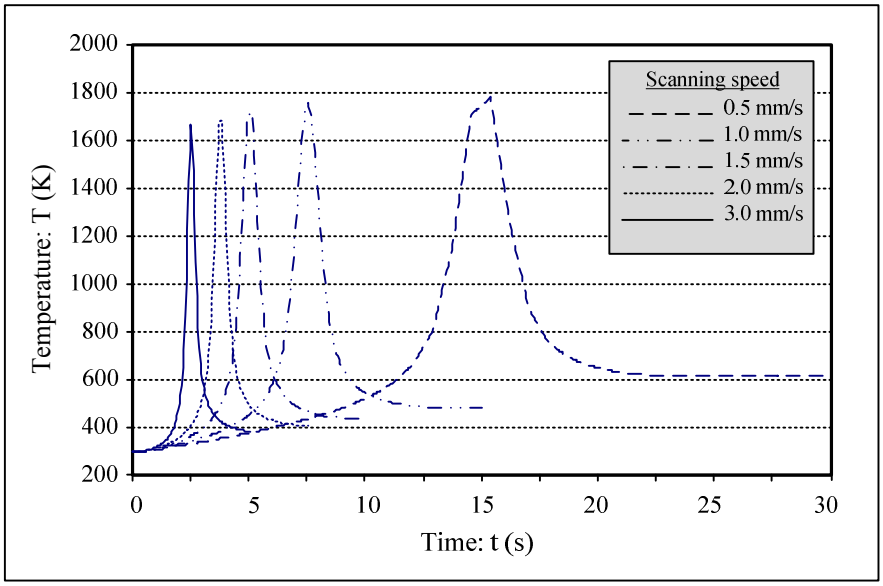

Figure 5.2 Temporal temperature profiles at point (12.5, 0, 5) mm of the first layer deposition for different process scanning speed

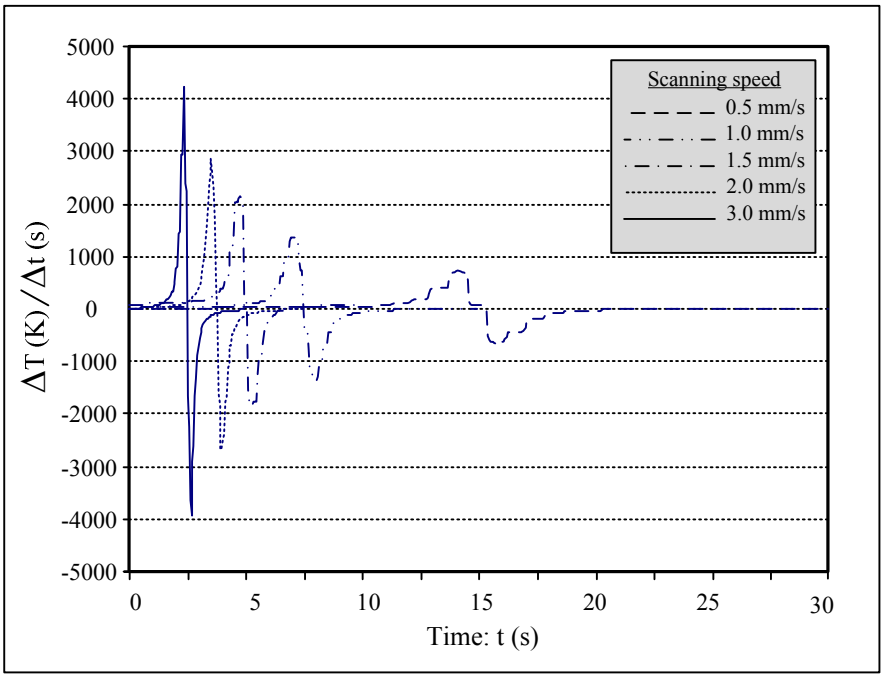

Figure 5.3 Cooling rates at point (12.5, 0, 5) mm of the first layer deposition for different process scanning speed

It was shown that for a very short interaction time ($t \leq 0.027$s) where the cooling rate is less than -31185 K/s, no inter-metallic phases were formed. For longer interaction times ($0.03 \leq t \leq 0.048$ s), a mixture of FeNb and Ti-Nb solid solution were observed. In addition, for longer interaction times where the cooling rate increased to -14235 K/S, only Fe_2Ti and Fe_2Nb compounds were formed without any solid solutions.

The experimental results also showed that even for a short interaction time, a uniform distribution of phases was formed throughout the deposed track. This result confirms that the convection effect in the melt pool is enough for an even distribution of Nb across the formed clad. The trends of cooling rates obtained from the model were verified by the results obtained from an analytical equation proposed for computing the cooling rates in laser cladding [16]. The numerical and experimental results showed that the time-dependent temperature distribution and consequently the cooling rate in the LSFF process have primary roles in microstructure and phase evolution during the deposition process. This was discussed in Section 4.3 as well.

In the next section, the effects of material properties in the multi-material deposition on the temperature distribution and stress field throughout the build-up process using LSFF will be discussed.

5.2 Fabrication of Multi-material Structures Using LSFF process

Most manufacturing protocols are developed for fabrication of homogeneous structures. They are based on the geometrical specifications and do not consider the effect of material variation across the body of a part [93, 94]. As briefly pointed out in Section 2.2, due to the flexibility and additive nature of the LSFF process, this method has shown great capability for fabrication of heterogeneous structures. The LSFF technique allows the creation of parts in which the deposited materials can change gradually from one region to another. To take advantage of the potential of this technique for fabrication of heterogeneous structures, the underlying physics of the process during the multi-material deposition should carefully be studied. This is important for the development of a process plan by which it is possible to counter the drawbacks associated with the LSFF process more efficiently. The drawbacks of

the LSFF process that are mainly prevalent in layered manufacturing techniques, such as delamination and crack formation, were comprehensively reviewed in the preceding chapters.

Since temperature distributions and thermal stress fields throughout the LSFF process primarily determine the final quality of the fabricated parts, especially for fabrication of multi-material structures with diverse material properties, dynamic prediction of the temperature distributions and thermal stresses and their evolutions throughout the process is crucial to understanding and consequently controlling the process. Therefore, in this section, the temporal temperature and thermal stress fields during the fabrication of a heterogeneous structure using the LSFF process are investigated. For this purpose, the coupled 3D numerical modelling approach developed in Chapter 3 with appropriate modifications is used to simulate multi-material deposition. The developed numerical model can predict the 3D geometry of each layer, the temperature distributions and thermal stress fields at any time during the build-up process.

In order to study the temperature distribution and thermal stress pattern in a layer-by-layer fashion and also to have a basis for comparing the results with their counterparts for single material structures, a four-layer thin wall of two Stellite 6 layers and two Ti layers are numerically and experimentally fabricated on a 25×20×5 mm substrate of sandblasted SS304L plate.

The experiments were carried out with the same procedure mentioned in Section 3.9.1 only with a different CNC table and laser. For the experiments performed for this section, a five-axis CNC table (Fadal), and a fiber laser with a maximum power of 1000 W (IPG) were used. Ti 99.6% powder of particle size 75-180 μm, and Stellite 6 powder of particle size 44-149 μm were used as the additive materials for the deposition process. After depositing the first two-layer, the process was stopped to change the additive material from Stellite 6 to Ti for the next two-layer deposition.

In the numerical analyses, the solution of the last time step of each simulation pass was considered as the initial condition for the simulation of the next pass (i.e., subsequent layer). After the second layer deposition, for transition from Stellite 6 to Ti, like in the experimental analysis, the simulation was started considering the ambient temperature for

the initial condition. The main process parameters and their values used for the modelling as well as experiments are listed in Table 5.1.

Table 5.1 Process parameters

Process parameter	Value	Unit
$\dot{m}$ - Powder feed rate	2	g/min
P - Laser Power	100-300	W
r_{jet} - Radius of the powder jet on the substrate	7.5e-4	m
r_l - Radius of the laser beam on the substrate	7.0e-4	m
T_0 - Ambient Temp.	298	K
T_m - SS304L Melting Temp.	1695	K
T_m - Stellite 6 Melting Temp.	1630	K
T_m - Ti Melting Temp.	1923	K
U- Process speed	1.5	mm/s

5.3 Temperature Distribution and Stress Field in the Multi-Material Deposition Process

The coupled temperature distributions, thermal stresses, and geometrical prediction of the additive material for the build-up process of a four-layer thin wall with the single-material (SS304L) were discussed in Chapter 3 and Chapter 4. It was shown that the maximum temperatures throughout the build-up process, from the first to the fourth layer, increase while the average maximum thermal stresses decrease. The maximum temperatures for the four-layer thin wall fabricated with the single-material were shown in Figure 4.3. The figure showed the increase in the maximum temperatures at the two end segments of the second to the fourth layer as well. Similar patterns were observed for the multi-material deposition,

Figure 5.4 showing the maximum temperatures throughout the four-layer depositions of two Stellite 6 layers and two Ti layers on SS304L, respectively. The laser power for this simulation was 300 W for the entire build-up process. Other process parameters are the same as those listed in Table 5.1.

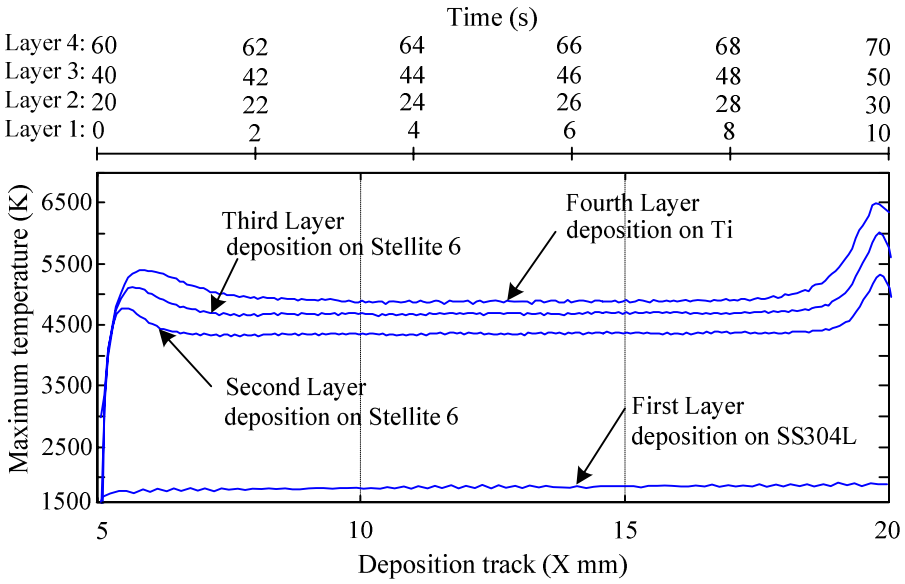

Figure 5.4 Maximum temperatures throughout the multi-materials deposition process

As seen in Figure 5.4, the maximum temperatures noticeably increase from the second layer. As discussed, the increases in the maximum temperatures for the upper layers are due to the nature of heat losses through the wall. For the first layer, the substrate acts as a heat sink and absorbs the energy distributed by the laser beam. As more layers are deposited, the heat losses through convection/radiation increase. Since the energy losses through convection/radiation are lower than those through conduction, the temperature rises as more layers are deposited. The same phenomena occur for the end segments compared to the middle sections. In addition, for the multi-material deposition, the thermo-physical properties of the substrate and additive materials play an important role in the maximum temperatures throughout the LSFF process. For the materials used in this study, the thermal conductivities for Ti and Stellite 6 are 62 and 67 per cent smaller than that for the substrate, respectively. Smaller heat conductivity results in a reduction in the heat loss

through conduction, and based on the same reasoning discussed above, the increase in the maximum temperatures from the first to the second layer are more noticeable. Since the thermal conductivities of Ti and Stellite 6 are almost the same, compared to SS304L, the increase in the maximum temperatures can only be the consequences of the geometrical changes within the build-up process. Therefore, an important point conveyed by the results illustrated in Figure 4.3 and Figure 5.4 is the effect of the material properties on the maximum temperatures generated throughout the process (for the material used in this investigation) compared to the geometrical changes. Hence, for the fabrication of heterogeneous structures, finding an optimal set of process parameters is crucial to arriving at a result with consistent physical and metallurgical properties. For instance, for the fabrication process with the parameters for which the maximum temperatures are as shown in Figure 5.4, in some parts of the wall poor bonding was observed as shown in Figure 5.5a. Figure 5.5b also shows an intersection of the same sample with better bonding. This inconsistency is the result of the melt pool condition for the first layer deposition which is not well-developed (considering the melting temperatures of the substrate and additive material compared to the maximum temperatures shown in Figure 5.4). For this purpose, the deposition of each layer was simulated with different laser powers, as the results are shown in Figure 5.6.

Figure 5.6 shows the average maximum temperatures for each layer resulting from different laser powers. The results show that the depositions with laser powers of 150 W are proper for the second to the fourth layer while a laser power of 300 W results in a well-developed melt pool for the deposition of the first layer. On the other hand, the depositions of the second to fourth layers using a laser power of 150 W have another important advantage, which is the effect on the thermal stress fields. The maximum thermal stresses formed throughout the process domain for the depositions of the second to the fourth layer reduce by 51.3, 50.0, and 50.7 per cent, respectively. But, for the first layer increasing the laser power from 300 to 350 W increases the maximum thermal stresses by 15.6 per cent. For the first layer, it was shown that the thermal stresses can effectively be reduced by preheating the substrate prior to the fabrication process [22, 57].

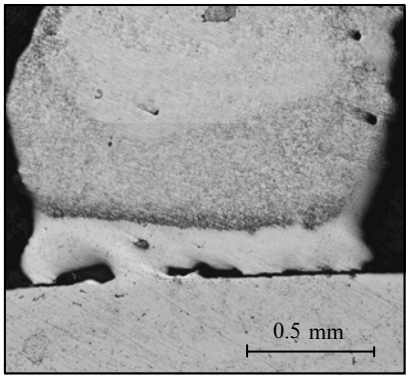

(a)

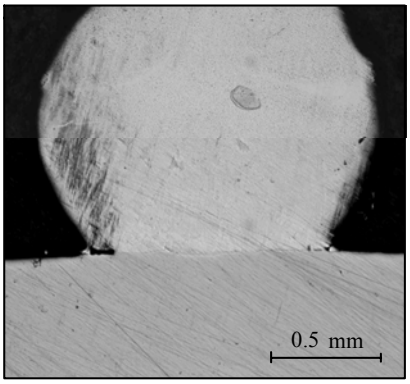

(b)

Figure 5.5 Cross sections of the four-layer thin wall fabricated using Stellite 6 and Ti

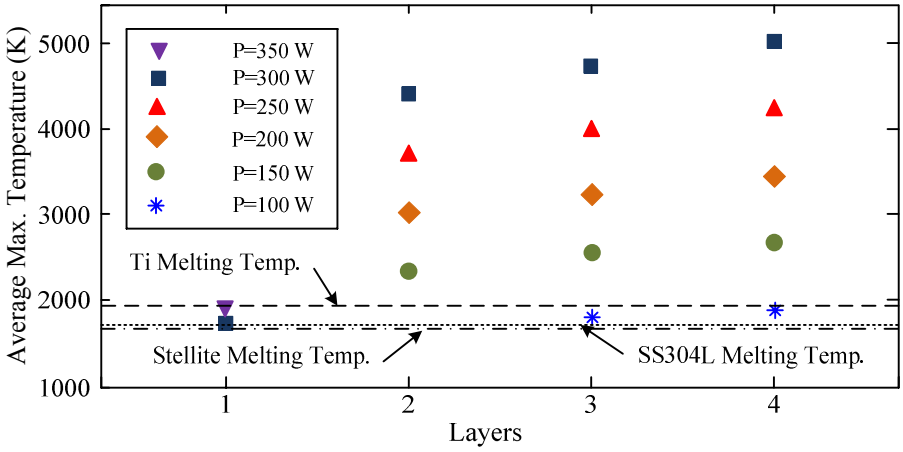

Figure 5.6 Average maximum temperatures for each layer with different laser power

For the single-material deposition, the thermal stress concentrations are formed around the melt pool. When the laser beam scans the two-end segments, another thermal stress concentration occurs at the two ends of the wall (where the wall connects to the substrate). Figure 5.7 shows the maximum thermal stresses imposed by the deposition of the fourth layer on the interfaces of the first layer and the substrate, the first and second layers, and the second and third layers. For this case the laser power was 150 W.

As seen, during the deposition of the fourth layer, the maximum thermal stresses on the interface of the first layer and the substrate increase at the two ends of the wall due to the sudden geometrical changes. The interesting point is that the maximum thermal stresses on the interface of the third layer, which is closer to the melt pool area, are 35 per cent less than the second layer which is farther from the melt pool zone. This is due to the material properties of the additive materials. The modulus of elasticity of Stellite 6 (116e3 MPa) is two times larger than Ti (237e3 MPa). Moreover, Stellite 6 has a larger linear coefficient of thermal expansion than Ti. Considering the governing equations, Equation (3.22), the values of these material properties can dominate the reduction in temperature gradient, which is 28 per cent from the third to the second layer.

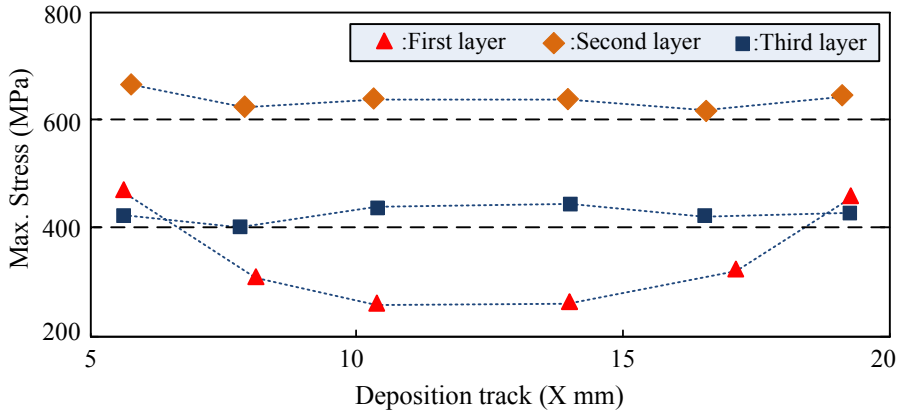

Figure 5.7 Maximum thermal stresses (Von Mises) imposed by the deposition of the fourth layer on the first, second, and third layers

Finally, the four-layer thin wall was experimentally fabricated with the optimum laser power obtained from the numerical simulation shown in Figure 5.6. For the sample fabricated with a laser power 300 W for the deposition of the first layer and 150 W for the second, third and fourth layers, no micro-cracking was observed. Figure 5.8 shows the interface regions between successive layers. Poor bonding and delamination were substantially reduced compared to the samples fabricated with the higher laser powers (few isolated poor bonding between the first layer and the substrate were observed, mainly at the beginning of the deposited clad).

For the sample fabricated with laser power of 300 W for the whole process, in addition to the poor bonding, delamination between the second and third layers was also observed. This was expected since the maximum thermal stresses for the third and fourth layers occur at the interface between the second and third layer as shown in Figure 5.7. The bonding between the second and the third layer can also improve by subsequent deposition of Ti and Stellite.

5.4 Summary

In LSFF, the final physical quality of a fabricated part is a function of sensitive and interrelated process parameters. Therefore, understanding the relationships between these parameters and their effects on the process is crucial. Many research groups experimentally defined a process window by which it is possible to determine an optimum set of process parameters for deposition of a specific additive material. Many parameters based on the process parameters have also been defined to measure the quality of the fabricated parts. With advances in process modelling, the effects of some of the main process parameters were individually studied using numerical analyses as well as experimental investigations.

In this research, the effects of material properties in multi-material deposition were specifically studied. Numerical simulations along with the experimental investigations were conducted to study the effects of multi-material properties on the temperature distribution and stress field throughout the build-up process. The multi-material deposition in LSFF is the basis for the fabrication of heterogeneous structures which have potential of functioning in multidisciplinary environments. For this purpose, the developed numerical model was

used to simulate the fabrication of a thin wall composed of two Stellite 6 layers and two Ti layers on a stainless steel substrate. The temperature distribution and thermal stress fields and their evolutions throughout the fabrication process were studied in a layer-by-layer fashion. The results showed that for multi-material deposition, the thermo-physical properties of the substrate and additive materials play an important role in the maximum temperatures and thermal stresses formed throughout the LSFF process. Contrary to the single material deposition in which the thermal stress concentrations were formed around the melt pool, during the deposition of the fourth layer, the maximum thermal stresses on the interface of the third layer, which is closer to the melt pool area, are 35 per cent less than the second layer which is farther from the melt pool zone. The numerical results were also used to define an optimum laser power for each layer deposition to reduce the temperature gradients and consequently the thermal stresses induced throughout the deposition process.

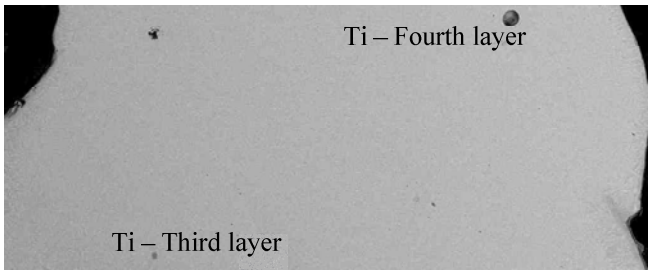

(a)

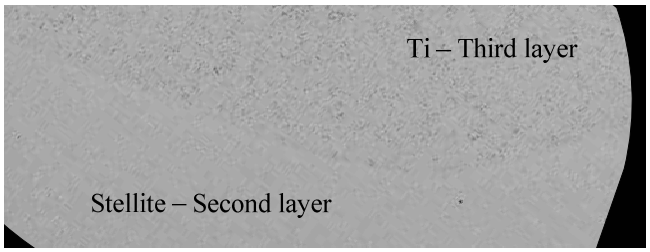

(b)

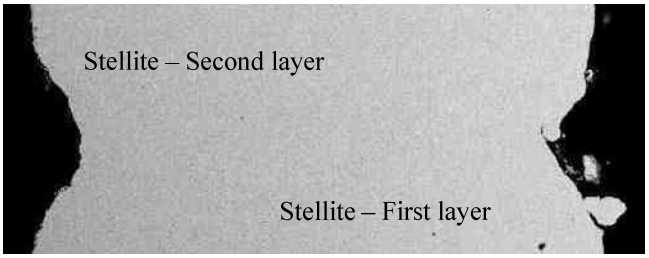

(c)

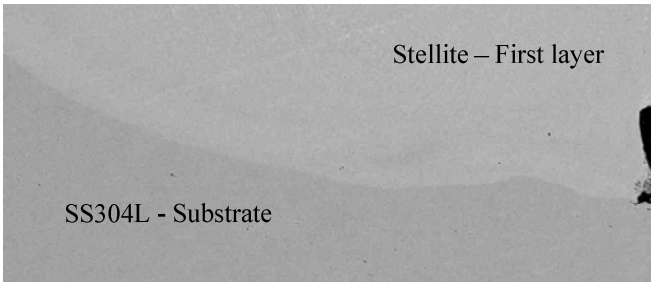

(d)

Figure 5.8 Cross sections of the four-layer thin wall fabricated using Stellite 6 and Ti: a) Fourth and third layers, b) Third and second layers, c) Second and first layers, d) First layer and substrate

Chapter 6

Conclusions and Future Work

The objective of the research presented in this thesis was to study the underlying physics of multilayer material deposition in LSFF, as well as to investigate certain drawbacks which limit the full capability of this emerging manufacturing technique. A 3D coupled time-dependent modelling approach was developed to assist the investigation in parallel to the experimental analyses. This chapter concludes the thesis by highlighting the main results achieved through numerical and experimental analyses presented in the preceding chapters. A separate section is also devoted to some topics and recommendations stemming from this study that can be considered as the basis for potential future studies in the field of laser material processing.

6.1 Conclusions

Modelling complex systems and processes can help improve our understating of fundamental characteristics of these systems and processes, which are often not possible to obtain or deduce directly through experimental analyses. In addition, the models developed can be of great assistance in comparing potential alternative solutions to address limitations of the system or process. This was the motivation for modelling multilayer LSFF deposition as a complex multidisciplinary and a fairly fast physical process. Since this manufacturing technique has the potential to solve many limitations in conventional fabrication of

heterogeneous structures, in addition to LSFF multilayer fabrication, the model developed was also employed to investigate the effect of the multi-material deposition on the process outcomes. The following are the main results and contributions achieved in this research:

1. **Multi-physics modelling of the LSFF process:** A coupled transient 3D multi-physics model of the LSFF process was developed to predict the geometry of the deposited material as well as temperature and thermal stress fields across the process domain in a dynamic fashion. For this purpose, the process was first mathematically modeled through the 3D heat conduction and the thermoelastic constitutive equations along with their associated boundary conditions. The effects of the main process parameters such as powder catchment and the moving leaser beam were then considered in the boundary conditions.

   Contrary to the reported modelling approaches, the modelling approach proposed in this research was coupled with an algorithm developed for the geometry prediction of the additive material. The final mathematical model of the process was then solved by using numerical methods. In the proposed algorithm for the geometrical prediction, the thermal domain is numerically obtained assuming a decoupled interaction between the laser beam and powder stream. Using this method, it is possible to predict the geometry of the additive material in a layer-by-layer fashion while considering the effects of the deposition on non-planar surfaces on the main operating parameters.

   In addition, most numerical models are developed for the single layer deposition process, and are also limited to thermal analyses. Few models, developed for multilayer deposition, solve the thermal and stress fields in a decoupled fashion. In addition, the geometry of the additive material considered for solving the temperature and stress distributions is not realistic. In the modelling approach presented in this thesis, in addition to the geometrical prediction of the additive material, the temperature distributions and the temporal thermal stress fields are dynamically determined using a coupled solution strategy. The model can predict the temperature and thermal stress distributions and their variations throughout the whole process. The temperature and thermal stress distributions and their history for each specific point within the LSFF

medium provide exclusive information and data to comprehensively study the effects of the physical phenomena involved in the LSFF process on the final qualities of the fabricated parts.

To demonstrate the capability of the proposed algorithm, a buildup process of a four-layer thin wall of SS304L was simulated. The performance and accuracy of the algorithm were experimentally verified. In conclusion, the main results from this section of the research are as follows:

- The numerical results of the geometry prediction showed that more material is deposited in the upper layers as well as at the two end segments of the wall for the second to the fourth layer. This is due to the increase in powder catchment efficiency for higher layers. It was shown that the powder catchment efficiency increases for higher layers while the effective absorption factor decreases.
- Due to geometrical changes and consequently the nature of heat losses, the maximum temperatures for the upper layers rise throughout the build-up process. The same patterns are also observed between the middle and the end segments of the wall for the upper layers.
- Based on the results obtained in this study, it is possible to define critical values for the maximum temperature and thermal stresses throughout the LSFF process. These critical values can determine a process window in which a part can be fabricated free from potential delamination and cracking. The numerical and experimental results confirm that this critical value for the ratio of the maximum thermal stresses to the maximum temperatures for the particular geometry and material used in this work is between 7e5 and 10.5e5 Pa/K.

2. **Correlation between temporal temperature distribution and microstructure:** While the thermal stresses are the main cause of any possible delamination and crack formation across the deposited layers, the temperature distributions and subsequent rapid cooling rates, determine the microstructure and final physical properties of the parts fabricated using LSFF. Therefore, investigation of the correlation between the formed

microstructure and thermal history of each point within the process domain can provide information for finding an optimum set of process parameters to achieve a desired and consistent microstructure across the fabricated part.

It was shown that the formed microstructures within the four-layer wall such as dendritic with and without secondary arms and their mixes, are a function of the temperature history (the temperature gradient at the solid/liquid interface and the cooling rate). Therefore, regarding the numerical and experimental results, a model of the process can provide a perspective of the microstructure and its variation throughout a fabricated part, prior to the build-up process.

3. **Effect of preheating the substrate on the temperature and thermal stress fields:** Since the thermal stress patterns and intensity contribute significantly to potential delamination and crack formation, the numerical results obtained from the model were used to study the correlation between the temperature distributions and stress fields, and the delamination and crack formation during the LSFF process.

The effect of preheating the substrate prior to the fabrication process on the delamination and crack formation were investigated. The investigation was conducted through the numerical and experimental fabrication of a four-layer thin wall of AISI 304L steel. To study the effects of the preheating, simulations were done for the substrates preheated from 400 to 800 K in 100 K intervals. All through the study, appropriate experiments were conducted for the preheated and non-preheated substrates to verify the numerical analyses and their related interpretations. The main results of this study are summarized as follows:

- The relationships between the temperature distribution, geometry of the deposition zone, and consequently the temporal thermal stress patterns throughout the process domain indicate the locations which are more prone to delamination and micro-crack formations across fabricated parts.
- The numerical analyses along with the experimental investigations showed that preheating the substrate prior to the LSFF process reduces the thermal stresses

during the fabrication process. For instance, for the substrate preheated to 700 K, the average maximum stresses reduce by about 4 per cent compared to those of the non-preheated model.

- A significant increase in the melt pool temperature that results from preheating the substrate (which was revealed by the numerical results) is an advantage for reducing the required laser power while keeping the melt pool in its proper condition. This method significantly decreases the temporal thermal stresses during the process compared to the cases in which only the substrate was preheated with the same applied laser power. For instance, within the specific operating parameters and material properties of this work, a crack-free result was obtained for the substrate preheated to 800 K using an optimum laser power. For this case, a 22 per cent reduction in thermal stresses is obtained throughout the process domain while the melt pool characteristics throughout the fabrication process remained the same compared to the non-preheated substrate.
- Another advantageous feature of preheating is that the transient time for developing a properly formed melt pool is shorter in the preheated models relative to the non-preheated ones. For the model developed in this research, the transient time for the full-developed melt pool of a model in which the substrate preheated to 600 K is 96.5 per cent shorter than its counterpart for the non-preheated model.

4. **Effect of path pattern on the temperature and thermal stress fields:** In LSFF, path pattern plays a determining role on the temperature distribution and consequently on the thermal stress field within a build-up domain during the fabrication process. The proposed modelling approach was employed to study two different path patterns and their effects on the deposition of WC-Co on a WC-Co substrate. With the same operating parameters, two different deposition paths demonstrated two different outcomes. Numerical results for these specific material and geometries showed that deposition with offset overlap can generate a better result (i.e., lower thermal stresses) than a continuous overlapped path pattern.

5. **Fabrication of Multi-material component:** To study multi-material fabrication using LSFF and its associated physical phenomena, a four-layer thin wall of two Stellite 6 layers and two Ti layers was simulated on a SS304L substrate using the numerical model. The temperature distributions, the thermal stresses, and their evolutions throughout the fabrication process were studied. Compared to the single-material deposition, the numerical results revealed the effects of the thermo-physical material properties on the temperature distributions and the thermal stress fields. The main results concluded from this study are as follows:

   - For the material used in this study, it was identified that for the first layer deposition of Stellite 6 on the substrate of SS304L, a laser power of 350 W is required, while for the deposition of the second to the fourth layers (deposition of Stellite 6 and Ti), the laser power can be reduced to 150 W. These optimum laser powers play crucial role in reducing the temperature gradients and consequently the thermal stresses induced throughout the deposition process.

   - The numerical results showed the qualitative effects of the material properties on the thermal stress fields, relative to other process parameters investigated in the single material deposition. For instance, the maximum thermal stresses on the interface of the third layer, which is closer to the melt pool area, are 35 per cent less than the second layer which is farther from the melt pool zone during the deposition of the fourth layer, due to the differences between thermo-physical properties of Ti and Stellite 6.

6.2 Future Work

As pointed out throughout the thesis, LSFF is a fairly new trend in manufacturing with many innovative features. The topics discussed in this thesis have mainly focused on the fundamental underlying physics of the LSFF process which are required to be explored for achieving higher quality results as well as developing successful industrial applications.

There are many different aspects of the LSFF process which still warrant more extensive investigation and development, these include aspects related to the control and automation

of the process, and exploration of more commercial materials and alloys with novel properties that can be adopted for the process. Specifically, considering the outcomes and findings of this research, the following themes can be recommended for potential future studies in this field.

1. **Improvement of the LSFF model:** Some of the features of the modelling approach presented in this research have potential for improvement. The algorithm developed for the geometrical prediction of the additive material can directly be integrated in the FE model by future advances in the engineering computational packages (the introductory work in this regard has been reported as cited in Chapter 3). The melt pool region can separately be defined and then coupled with the remaining process domain. This can provide the advantage of considering the effects of the different strains formed in the melt pool. However, these improvements should carefully be taken into account since they might compromise the accuracy of the results in other aspects considered in the model.

2. **Development of real-time controller:** As discussed, the LSFF process is governed by a large number of sensitive operating parameters. The mechanical and metallurgical qualities of a part, which are determined by these parameters, may vary significantly even under the same operating conditions. Therefore, designing a control system to achieve reproducible results with constant properties specifically for the fabrication of complex geometries is unavoidable. The knowledge obtained from this thesis can be used to design a more comprehensive and efficient control plan. The first step is the development of non-contact process detectors to monitor the stability of the melt pool as a key factor during the fabrication process. The second step is the development of a real-time controller. Proper control systems can be designed through the examination of different control plans such as classical, neural networks, fuzzy logic, and neuro-fuzzy methods. A neuro-fuzzy model of the process that was already developed by Alimardani et al. [95] can be enhanced and used as a part of a controller, but for other methods, new models should be developed.

3. **Automated optimum layer decomposition and path planning paradigm:** In layered manufacturing, most of the slicing and path planning protocols are developed based on the geometry of a part. As discussed, in the LSFF process, the underlying physics of the process and consequently the final quality of a fabricated part tightly depend on the path pattern designed for the deposition process. Therefore, the results and findings of this research can be used as a basis for developing a more versatile and sophisticated slicing and path planning paradigm specifically for the LSFF technique. The model developed also can be used for a more comprehensive study of different path patterns to investigate the effects of the process parameters, and their advantages and disadvantages based on the geometrical specifications of an object.

4. **Heterogeneous structures with commercial applications:** There are several fundamental challenges involved in the fabrication of heterogeneous structures using LSFF. Most of the processes planning protocols and available engineering computational packages are developed for homogeneous structures. They are only based on the geometry and do not consider the effect of material variation in a part. The preliminary work performed in this research was focused only for a specific structure (deposition of two specific materials). This work can be continued to incorporate the effect of the material composition into the process a more precisely, specifically in the transition regions. This can be done by developing more accurate analytical model for the specific problems involved with these types of structures and then applying the results into the main model by making additional assumptions and adjustments.

5. **Experimental setup for fabrication of heterogeneous structures:** The experimental setup should be enhanced for the fabrications of heterogeneous structures. Since the material composition in heterogeneous parts should be controlled directly by the powder feeder through fusing multiple powder mixtures into the melt pool, depending on a material composition, several powder feeders with different nozzles as well as with a mixer and a nozzle are necessary. Using several powder feeders with a mixer facilitates a consistent composition of different materials in structures composed of various materials that their compositions change throughout the structures.

6. **Mechanical and metallurgical databases for new materials:** To fabricate the heterogeneous structures for real applications, a metallurgical investigation of the proper materials and alloys should be conducted in parallel to the other aforementioned tasks. As discussed in the thesis, different operating parameters result in very different outcomes. Therefore, the proper operating parameters for each set of materials with any specific application should accompany the other related results.

7. **New applications:** The advantageous LSFF features encourage engineers to employ this technique for fabrication of unconventional structures, which cannot be produced by traditional techniques. The model developed can facilitate the investigation of these new applications. For instance, since LSFF as a direct metal deposition method has inherent potential to control the topology and microstructure of the fabricated parts locally, it has shown inherent potential for fabrication of porous structures which are increasingly important for osseointegration and scaffold design in tissue engineering. The complexity involved in experimental fabrication of this type of structures can be overcome or at least alleviated by understanding the underlying physics of the process in this type of structure. This also can facilitate defining an optimum operating window prior to the experimental analyses.

Bibliography

1. L. Dubourg, D. Ursescu, F. Hlawka, A. Cornel, "Laser cladding of MMC coatings on aluminum substrate: influence of composition and microstructure on mechanical properties," Wear, vol. 258, no. 11-12, 2005, pp. 1745–1754.

2. M. Zhong, W. Liu, G. Ning, L. Yang, Y. Chen, "Laser direct manufacturing of tungsten nickel collimation component," Journal of Materials Processing Technology, vol. 147, 2004, no. 2, pp. 167–173.

3. J. D. Kim, K.H. Kang, J. N. Kim, "Nd:YAG laser cladding of marine propeller with hastelloy C-22," Applied physics A, Material Science & Processing, vol. 79, no. 4-6, 2004, pp. 1583–1585.

4. X. Yan, P. Gu, "A review of rapid prototyping technologies and systems," Journal of Computer-Aided Design, vol. 28, no. 4, 1996, pp. 307–318.

5. D.T. Pham, R.S. Gault, "A comparison of rapid prototyping technologies," International Journal of Machine Tools and Manufacturing, vol. 38, 1998, pp. 1257–1287.

6. P. Kulkarni, A. Marsan, D. Dutta., "A review of process planning techniques in layered manufacturing," Rapid Prototyping Journal, vol. 6, no. 1, 2000, pp. 18–35.

7. E.S. Santos, M. Shiomi, K Osakada, T. Laoui, " Rapid manufacturing of metal components by laser forming," International Journal of Machine Tools and Manufacturing, vol. 46, 2006, pp, 1459-1468.

8. C.P. Paul, A. Jain, P. Ganesh, J. Negi, A.K. Nath, "Laser Rapid Manufacturing of Colmonoy-6 Components," Journal of Optics & Laser in Engineering, vol. 44, 2006, pp. 1096-1109.

9. W. Lee, J.M. Myoung, Y.H. Yoo, H. Shin, "Effect of thermal misfit stress on crack deflection at planar interfaces in layered systems," Journal of Composites Science and Technology, vol. 66, 2006, pp. 435–443.

10. N.W. Klingbeil, J.L. Beuth, R.K. Chin, C.H. Amon, "Residual stress-induced warping in direct metal solid freeform fabrication," International Journal of Mechanical Sciences, vol. 44, no. 2, 2002, pp. 57–77.

11. D. Hu, R. Kovacevic, "Sensing, modelling and control for laser-based additive manufacturing," International Journal of Machine Tool and Manufacture, vol. 43, no. 1, 2003, pp. 51–60.

12. H. Y. Chen, S. J. Huang, "Adaptive fuzzy sliding-mode control for the Ti6A14V laser alloying process," Int. Journal of Manuf. Technology, vol. 24, 2004, pp. 667–674.

13. D. Hu, H. Mei, R. Kovacevic, "Improving solid freeform fabrication by laser based additive manufacturing," Proceedings of the institution of mechanical engineers- Part B-Engineering Manufacture, vol. 216, no. 9, 2002, pp. 1253–1264.

14. K. Samanta, B. Koc., "Feature-based design and material blending for free-form heterogeneous object modelling," Journal of Computer-Aided Design, vol. 37, no. 3, 2005, pp. 287-305.

15. M. Alimardani, E. Toyserkani, J.P. Huissoon, "Three-dimensional numerical approach for geometrical prediction of multilayer laser solid freeform fabrication process," Journal of laser applications, vol. 19, no. 1, 2007, pp. 14–25.

16. W.M. Steen, Laser Material Processing. Third edition, Springer, 2003.

17. Y. Fu, A. Loredo, B. Martin, A. B. Vannes., "A theoretical model for laser and powder particles interaction during laser cladding," Journal of Material Technology, vol. 128, no. 1-3, 2002, pp. 106–112.

18. G. Palumbo, S. Pinto, L. Tricarico, "Numerical finite element investigation on laser cladding treatment of ring geometries," Journal of Material Processing Technology, vol. 155-156, no. 1-3, 2004, pp. 1443–1450.

19. M.Y. Wang, X. Wang., "A level-set based variational method for design and optimization of heterogeneous objects," Computer-Aided Design, vol. 37, no. 3, 2005, pp. 321–337.

20. M. Schneider, "Laser cladding with powder: effect of some machining parameters on clad properties", Ph.D. Thesis University of Twente, Enschede, The Netherlands, 1998.

21. D. Hu, R. Kovacevic, "Modeling and measuring the thermal behavior of the molten pool in closed-loop controlled laser-based additive manufacturing," Journal of Engineering Manufacture, vol. 212 Part B, 2003, pp. 441–452.

22. M. Alimardani, E. Toyserkani, J.P. Huissoon, "A 3D dynamic numerical approach for temperature and thermal stress distributions in multilayer laser solid freeform fabrication process," Journal of Optics and Lasers in Engineering, vol. 45, no. 12, 2007, pp. 1115–1130.

23. J.F. Ready, LIA handbook of laser material processing, Laser Institute of America. Mangolia Publishing Inc., 2001 p. 541–5.

24. J. Liu, L. Li, "In-time motion adjustment in laser cladding manufacturing process for improving dimensional accuracy and surface finish of the formed part," Journal of Optics and Laser Technology, vol. 43, 2004, pp. 477–483.

25. L. Han, F.W. Liou, K.M. Phatak, "Modelling of laser cladding with powder injection," Metallurgical and Materials Transaction, vol. 35B, 2004, pp. 1139–1150.

26. Y. L. Huang, G. Y. Liang, J. Y. Su, J. G. Li, "Interaction between laser beam and powder stream in the process of laser cladding with powder feeding," Journal of Modeling and Simulation in Material Science and Engineering, vol. 13, no. 1. 2005, pp. 47–56.

27. E. Toyserkani, A. Khajepour, S. F. Corbin, "3-D finite element modeling of laser cladding by powder deposition: Effects of laser pulse shaping on the process," Journal of Optics and Lasers in Engineering, vol. 4, no. 6, 2004, pp. 849–867.

28. E. Toyserkani, A. Khajepour, S. F. Corbin, "3-D finite element modeling of laser cladding by powder deposition: Effects of powder feedrate and travel speed on the process," Journal Laser Applications, vol. 15, no. 3, 2003, pp. 153–161.

29. B. Adak, P. Nash, D. Chen, "Microstructural characterization of laser cladding of Cu-30Ni," Journal of Material Science, vol. 40, no. 8, 2005, pp. 2051–2054.

30. S. Niederhauser, B. Karlsson, "Mechanical properties of laser cladded steel," Journal of Material Science and Technology, vol. 19, no. 11, 2003, pp. 1611–1616.

31. A. J. Pinkerton, L. Li, "Modeling the geometry of a moving laser melt pool and deposition track via energy and mass balances," Journal of Physics D: Applied Physics, vol. 37, 2004, pp. 1885–1895.

32. Y.L. Huang, J. Liu, N.H. Ma, J.G. Li, "Three-dimensional analytical model on laser-powder interaction during laser cladding," Journal of Laser Applications, vol. 18, no. 1, 2006, pp. 42–46.

33. F. M. White, Heat Transfer, Addison-Wesley Publishing Company, 1984, 588pp.

34. X. He, J. Mazumder, "Transport phenomena during direct metal deposition," Journal of Applied Physics, vol. 101, 2007, pp. 053113: 1-9.

35. J. Choi, L. Han, Y. Hua, "Modelling and experiments of laser cladding with droplet injection," Transactions of the ASME: Journal Heat transfer, vol. 127, 2005, pp. 978–986.

36. G.T. Mase, G.E. Mase., Continuum Mechanics for Engineers, CRC Press, Second edition, 1999.

37. S. Ghosh, J. Choi, "Three-dimensional transient finite element analysis for residual stresses in the laser aided direct metal/material deposition process," Journal of Laser Applications, vol. 17, no. 3, 2005, pp. 144–158.

38. P. Ferro, H. Porzner, A. Tiziani, F. Bonollo, "The influence of phase transformations on residual stresses induced by the welding process-3D and 2D numerical models," Journal of Modelling and Simulation in Material Science and Engineering, vol. 14, 2006, pp. 117–136.

39. A.P. Mackwood, R.C. Crafer, "Thermal modelling of laser welding and related processes: a literature review," Journal of Optics and Laser Technology, vol. 37, 2005, pp. 99-115.

40. M. Picasso, C.F. Marsden, J. D. Wagniere, A. Frend, M. Rappaz, "A simple but realistic model for laser cladding," Metallurgical and Material Transactions B, vol. 25B, no. 2, 1994, pp. 281–291.

41. C. Cho, G. Zhao, S. Kwak, C.B. Kim, "Computational mechanics of laser cladding process," Journal of Materials Processing Technology, vol. 153-154, 2004, pp. 494–500.

42. H. Qi, J Mazumder, H Ki, "Numerical simulation of heat transfer and fluid flow in coaxial laser cladding process for direct metal deposition," Journal of Applied Physics, vol. 100, 2006, pp 024903: 1-11.

43. P. Peyre, P. Aubry, R. Fabbro, R. Neveu, A. Longuet, "Analytical and numerical modelling of the direct metal deposition laser process", Journal of Physics D: Applied Physics, vol. 41, no. 2, 2008, pp. 025403: 1–10.

44. R. C. Luo, C. L. Chang, Z. H. Huang, J. H. Tzou, " Rapid tooling for automated desktop manufacturing," International Conference on Robotics and Automation, New Orleans, LA, Proceeding of the 2005 IEEE, pp. 584–589.

45. R. C. Luo, C. C. Chen, J. H. Tzoug, "The development of a direct metallic rapid prototyping system," The 30th Annual Conference of the IEEE industrial Electronics Society, 2004, pp. 33–38.

46. A. J. Pinkerton, L. Li, " The effect of laser pulse width on multiple-layer 316L steel clad microstructure and surface finish," Journal of Applied Surface Science, vol. 208-209, no. 1, 2003, pp. 411–416.

47. A. J. Pinkerton, L. Li, " An investigation of the effect of pulse frequency in laser multiple-layer cladding of stainless steel," Journal of Applied Surface Science, vol. 208-209, 2003, pp. 405–410.

48. A. J. Pinkerton, L. Li, "Multiple-layer cladding of stainless steel using a high-powered diode laser: an experimental investigation of the process characteristics and material properties," Thin Solid Films, vol. 453-454, 2004, pp. 471–476.

49. J. Liu, L. Li, "Effect of powder concentration distribution on fabrication of thin-wall parts in coaxial laser cladding," Journal of Optics & Laser Technology, vol. 37, no. 4, 2005, pp. 287–292.

50. A. Vasinonta, J. L. Beuth, M. L. Grifith, "A process map for consistent build condition in the solid freeform fabrication of thin-walled structures," Journal of Manufacturing Science and Engineering, vol. 123, no. 4, 2001, pp. 615–622.

51. L. Han, K.M. Phatak, F.W. Liou, "Modeling of laser deposition and repair process," Journal of Laser application, vol. 17, no. 2, 2005, pp. 89–99.

52. L. Costa, R. Vilar, T. Reti, A.M. Deus, "Rapid tooling by laser powder deposition: Process simulation using finite element analysis," Acta Materialia, vol. 53, 2005, pp. 3987–3999.

53. A.S. C.M. D'Oliveira, C.P. Da Silva, R. MC. Vilar, "Microstructural features of consecutive layers of satellite 6 deposited by laser cladding," Journal of Surface and Coating Technology, vol. 153, 2002, pp. 203–209.

54. M.P. Mughal, H. Fawad, R.A. Mufti, M. Siddique, "Deformation modeling in layered manufacturing of metallic parts using gas metal arc welding: effect of process parameters," Journal of Modeling and Simulation in Material science and Engineering, vol. 13, 2005, pp. 1187–1204.

55. A.H. Nickel, D.M. Barnett, F.B. Prinz, "Thermal stresses and deposition patterns in layered manufacturing", Journal of Material Science and Engineering A, vol. 317, 2001, pp. 59–64.

56. R. Jendrzejewski, G. Sliwinski, M. Krawczuk, W. Ostachowicz, "Temperature and stress fields induced during laser cladding," Journal of Computers and Structures, vol. 82, no. 2, 2004, pp. 653–658.

57. R. Jendrzejewski, G. Sliwinski, "Investigation of temperature and stress fields in laser cladding coating," Journal of Applied Surface science, vol. 254, no. 4, 2007, pp. 921–925.

58. A.P. Mackwood, R.C. Crafer, "Thermal modelling of laser welding and related processes," Optics and laser technology, vol. 37, 2005, pp. 99–115.

59. C. Lampa, A.F.H. Kaplan, J. Powell, C. Magnusson, "Analytical thermodynamic model of laser welding," Journal of Physics D: Applied Physics, vol. 30, no. 9, 1997, pp. 1293–1299.

60. S. Kumar, S. Roy, C.P.Paul, A.K. Nath, "Three-dimensional conduction heat transfer model for laser cladding process ," Journal of Numerical Heat Transfer, Part B: Fundamental, vol. 53, 2008, pp. 271–287.

61. S. Brown, H. Song, "Finite element simulation of welding of large structures," Trans. ASME, J. Eng. for Industry, vol. 114, no. 4, 1992, pp. 441–451.

62. N. Noda, R. Hetnarski, Y Tanigawa., Thermal Stresses, Taylor & Francis, Second edition, 2003.

63. A.W. Fitzgibbon, M. Pilu, R.B. Fischer, "Direct least squares fitting of ellipses," The 13th International Conference on Pattern Recognition, Vienna, 1996, pp 253–257.

64. M. Kalyon, B.S. Yilbas, "Exact solution for time exponentially varying pulsed laser heating: convective boundary condition case," Proceedings of the Institution of Mechanical Engineers, Part C: Journal of Mechanical Engineering Science, vol. 215, no 5, 2001, pp 591-602.

65. A.J. Pinkerton, L. Li, "The development of temperature fields and powder flow during laser direct metal deposition wall growth," Proceedings of the Institution of Mechanical Engineers, Part C: Journal of Mechanical Engineering Science, vol. 218, no C5, 2004, pp. 531–541.

66. Z. Jandric, R. Kevacevic, "Heat management in solid free-from fabrication based on deposition by welding," Journal of Engineering Manufacturing Part B, vol. 218, 2004, pp. 1525–1540.

67. J. Sears, "Additive manufacturing and repair," 26th International Congress on the Applications of Lasers and Electro-Optics (ICALEO), Orlando, FL, USA, Ref. code 1902, 2007, pp. 1058-1063.

68. R. Grylls, T. Marchione, D. Keicher, "Advances in laser-deposition equipment and capabilities," 26th International Congress on the Applications of Lasers and Electro-Optics (ICALEO), Orlando, FL, USA, Ref. code 1902, 2007, pp. 1074-1080.

69. C.P. Paul, M. Iravani, A. Khajepour, S. Corbin, "Automated laser fabrication of high performance saw blades," 26th International Congress on the Applications of Lasers and Electro-Optics (ICALEO), Orlando, FL, USA, Ref. code 2003, 2007, pp. 1003-1006.

70. S. Li, Q. Hu, X. Zeng, S. Ji, "Effect of carbon content of the microstructure and the cracking susceptibility of Fe-based laser-clad layer," Journal of Applied Surface Science, vol. 240, 2005, pp. 63–70.

71. E. Toyserkani, A. Khajepour, S. Corbin., Laser Cladding, CRC Press, 2005.

72. W. Kurz, "solidification microstructure processing maps: theory and application," Journal of Advanced Engineering Materials, vol. 3, no. 7, 2001, pp 443-452.

73. R. Jendrzejewski, I. Kreja, G. Sliwinski, "Temperature distribution in laser-clad multi-layers," Journal of Materials Science and Engineering A, vol. 379, 2004, pp 313-320.

74. S.C. Gill, M. Zimmermannn, W. Kurz, "Laser resolidifcation of the Al-Al2Cu Eutectic: the coupled zone," Acta Metallurgia Materialia, vol. 40, no. 11, 1992, pp. 2895-2906.

75. R. Vilar, "Laser Cladding," Journal of Laser Applications, vol. 11, 1999, pp. 64-79.

76. M. Carrard, M. Gremaud, M. Zimmermann, W. Kurz, "About the banded structure in rapidly solidified dendritic and eutectic alloys," Acta Metallurgia Materialia, Vol. 40, no. 5, 1992, pp. 983-996.

77. D.A. Porter, K.E. Easterling, *Phase transformations in metals and alloys*, Van Nostrand Reinhold Co. Ltd., 1981.

78. A.H. Nickel, "Analysis of thermal stresses in shape deposition manufacturing," Ph.D. Thesis, Stanford University, USA, 1999.

79. R. Dwivedi, R. Kovacevic, "Process planning for multi-directional laser-based direct metal deposition," Journal of mechanical engineering science, vol. 219 Part C, 2005, pp. 695–707.

80. B.O. Kim, B.K. Choi, "Machining efficiency comparison direction-parallel tool path with contour-parallel tool path", Computer-Aided design, vol. 34, no. 2, 2002, pp. 89–95.

81. K.A. Tarabanis, "Path planning in the proteus rapid prototyping system", Rapid Prototyping Journal, vol. 7, no. 5, 2001, pp. 241–252.

82. V.T. Rajan, V. Srinivasan, K.A. Tarabanis, "The optimal zigzag direction for filling a two-dimensional region", Rapid Prototyping Journal, vol. 7, no. 5, 2001, pp. 231–240.

83. Krishnan Ramaswami, "Process planning for shape deposition manufacturing", Ph.D. Thesis, Stanford University, USA, 1997.

84. C.P. Paul, M. Alimardani, A. Khajepour, "Effect of rastering pattern on delamination behaviour during Automated Laser Fabrication", Proceedings of the Fourth International WLT-Conference on Lasers in Manufacturing (LIM), Munich, Germany, pp. 203-206, June 18-21, 2007.

85. Y. Li, J. Ma, "Study on overlapping in the laser cladding process", Surface and Coating Technology, vol. 90, 1996, pp. 1–5.

86. P. Singh, P. Kulkarni, H. Qi, V. Kumar, M. Azer, "Investigation on toolpath geometries for surface quality improvement in laser net shape manufacturing", Laser Material Processing Conference, ICALLEO, 2005, pp. 326–330.

87. J. Majhi, R.Janardan, M. Smid, P. Gupta, "On some geometric optimization problems in layered manufacturing," Computational Geometry: Theory and Application, vol. 12, no. 3-4, 1999, pp.219–239.

88. P. Kulkarni, D. Dutta, "An accurate slicing procedure for layered manufacturing," Journal of Computer-Aided Design, vol.28, no.9, 1996, pp. 683–697.

89. W.W. Duley, Laser processing and analysis of materials. Plenum, 1983.

90. E.W. Kreitz, G. Backes, A. Gasser, K. Wissenbach, "Rapid prototyping with Co_2 laser radiation," Journal of Applied Surface Sciencd, vol. 86, 1995, pp. 310–316.

91. G.J. Bruck, "Fundamentals and industrial applications of high power laser beam cladding," Laser Beam Surface Treating and Coating, SPIE, vol. 957, pp. 14-28, Dearborn, Michigan, 29-30 June 1988.

92. V. Fallah V., A. Khajepour, M. Alimardani, "A Numerical-Experimental Investigation on the Deposition of Ti-45Nb on Mild Steel using Automated Laser Fabrication Process", 27th International Congress on the Applications of Lasers and Electro-Optics (ICALEO), Temecula, California, USA, October 20-23, 2008, Ref. code 505.

93. K.H. Shin, D. Dutta, "Process-planning for layered manufacturing of heterogeneous object using direct metal deposition," Journal of Computing and Information Science in Engineering, vol. 2, 2002, pp. 330–344.

94. K.H. Shin, H. Natu, D. Dutta, J. Mazumder, "A method for the design and fabrication of heterogeneous objects," Journal of Material and Design, vol. 24, 2003, pp. 339–353.

95. M. Alimardani, E. Toyserkani, "Prediction of Laser Solid Freeform Fabrication Using Neuro-fuzzy Method", Journal of Applied Soft Computing, vol. 8, no. 1, 2008, pp 316-323.